

This work was written as part of one of the author's official duties as an Employee of the United States Government and is therefore a work of the United States Government. In accordance with 17 U.S.C. 105, no copyright protection is available for such works under U.S. Law.

Public Domain Mark 1.0

<https://creativecommons.org/publicdomain/mark/1.0/>

Access to this work was provided by the University of Maryland, Baltimore County (UMBC) ScholarWorks@UMBC digital repository on the Maryland Shared Open Access (MD-SOAR) platform.

Please provide feedback

Please support the ScholarWorks@UMBC repository by emailing scholarworks-group@umbc.edu and telling us what having access to this work means to you and why it's important to you. Thank you.

Application of spheroid models to account for aerosol particle nonsphericity in remote sensing of desert dust

Oleg Dubovik,^{1,2} Alexander Sinyuk,^{1,3} Tatyana Lapyonok,^{1,3} Brent N. Holben,¹ Michael Mishchenko,⁴ Ping Yang,⁵ Tom F. Eck,^{1,6} Hester Volten,⁷ Olga Muñoz,⁸ Ben Veihelmann,⁹ Wim J. van der Zande,¹⁰ Jean-Francois Leon,¹¹ Michael Sorokin,^{1,3} and Ilya Slutsker^{1,3}

Received 24 August 2005; revised 21 November 2005; accepted 15 February 2006; published 15 June 2006.

[1] The possibility of using shape mixtures of randomly oriented spheroids for modeling desert dust aerosol light scattering is discussed. For reducing calculation time, look-up tables were simulated for quadrature coefficients employed in the numerical integration of spheroid optical properties over size and shape. The calculations were done for 25 bins of the spheroid axis ratio ranging from ~ 0.3 (flattened spheroids) to ~ 3.0 (elongated spheroids) and for 41 narrow size bins covering the size parameter range from ~ 0.012 to ~ 625 . The look-up tables were arranged into a software package, which allows fast, accurate, and flexible modeling of scattering by randomly oriented spheroids with different size and shape distributions. In order to evaluate spheroid model and explore the possibility of aerosol shape identification, the software tool has been integrated into inversion algorithms for retrieving detailed aerosol properties from laboratory or remote sensing polarimetric measurements of light scattering. The application of this retrieval technique to laboratory measurements by Volten et al. (2001) has shown that spheroids can closely reproduce mineral dust light scattering matrices. The spheroid model was utilized for retrievals of aerosol properties from atmospheric radiation measured by AERONET ground-based Sun/sky-radiometers. It is shown that mixtures of spheroids allow rather accurate fitting of measured spectral and angular dependencies of observed intensity and polarization. Moreover, it is shown that for aerosol mixtures with a significant fraction of coarse-mode particles (radii $\geq \sim 1 \mu\text{m}$), the nonsphericity of aerosol particles can be detected as part of AERONET retrievals. The retrieval results indicate that nonspherical particles with aspect ratios ~ 1.5 and higher dominate in desert dust plumes, while in the case of background maritime aerosol spherical particles are dominant. Finally, the potential of using AERONET derived spheroid mixtures for modeling the effects of aerosol particle nonsphericity in other remote sensing techniques is discussed. For example, the variability of lidar measurements (extinction to backscattering ratio and signal depolarization ratio) is illustrated and analyzed. Also, some potentially important differences in the sensitivity of angular light scattering to parameters of nonspherical versus spherical aerosols are revealed and discussed.

Citation: Dubovik, O., et al. (2006), Application of spheroid models to account for aerosol particle nonsphericity in remote sensing of desert dust, *J. Geophys. Res.*, *111*, D11208, doi:10.1029/2005JD006619.

1. Introduction

[2] Adequate modeling of light scattering by nonspherical particles is widely recognized as one of the major difficulties in remote sensing of tropospheric aerosols in

¹Laboratory for Terrestrial Physics, NASA Goddard Spaceflight Center, Greenbelt, Maryland, USA.

²Now at Laboratoire d'Optique Atmosphérique, Université de Lille 1/CNRS, Villeneuve d'Ascq, France.

³Also at Science Systems and Applications, Inc., Lanham, Maryland, USA.

⁴NASA Goddard Institute for Space Studies, New York, New York, USA.

⁵Department of Atmospheric Sciences, Texas A&M University, College Station, Texas, USA.

⁶Also at Goddard Earth Sciences and Technology Center, University of Maryland Baltimore County, Baltimore, Maryland, USA.

⁷Astronomical Institute "Anton Pannekoek," University of Amsterdam, Amsterdam, Netherlands.

⁸Instituto de Astrofísica de Andalucía, Granada, Spain.

⁹Royal Netherlands Meteorological Institute, De Bilt, Netherlands.

¹⁰Molecular and Biophysics, Institute for Molecules and Materials, Radboud University, Nijmegen, Netherlands.

¹¹Laboratoire d'Optique Atmosphérique, Université de Lille 1/CNRS, Villeneuve d'Ascq, France.

general and desert dust in particular. There are various in situ and laboratory measurements [e.g., Heintzenberg, 1998; Nakajima et al., 1989; West et al., 1997; Volten et al., 2001] as well as remote sensing results [Koepke and Hess, 1988; Kaufman, 1993; Sasano and Browell, 1989; Liu et al., 1999; Dubovik et al., 2002a; Deuzé et al., 2000; Sinyuk et al., 2003; Müller et al., 2003; Wang et al., 2003; Herman et al., 2005; Kalashnikova et al., 2005] that reveal significant deviations of light scattering of desert dust aerosols from scattering properties of homogeneous spheres [Mishchenko et al., 2000]. As a result, there have been numerous efforts to account for particle nonsphericity in aerosol retrieval algorithms [e.g., Kahn et al., 1997; Krotkov et al., 1999; Liu et al., 1999; Dubovik et al., 2002b; Mishchenko et al., 2003; Herman et al., 2005; Kalashnikova et al., 2005]. Nevertheless, at present, there is no single widely accepted light scattering model for applications to the retrieval of desert dust properties. The development of such a model appears to be difficult both methodologically and technically. For example, Kalashnikova and Sokolik [2002, 2004] proposed the strategy of modeling light scattering by an ensemble of nonspherical particles using some geometrical particle parameters derived from in situ measurements of ambient desert dust. However, both the measurement of the aerosol microphysical properties as well as the modeling of light scattering by a single particle with varying size, shape and composition have significant limitations. The in situ and laboratory measurements have issues with sampling of unperturbed aerosol, isolation of aerosol particles, and evaluation of their physical and optical parameters [e.g., Bond et al., 1999; Haywood et al., 2003; Reid et al., 2003a, 2003b; Tanré et al., 2003]. The modeling of optical properties of single particles with diverse geometrical shapes and morphologies has been addressed by many fruitful studies for a number of years [e.g., van de Hulst, 1957; Bohren and Huffman, 1983; Mishchenko et al., 2000, 2002]. However, because of the complex nature of the light scattering formalism, the models available for applications are rather limited. Specifically, the exact solutions describing the interaction of the electromagnetic field with a single particle exist only for a few selected geometrical shapes [Mishchenko et al., 2000, 2002]. Existing numerical methods, such as the discrete dipole approximation [e.g., Draine and Flatau, 1994] and the finite difference time domain technique [e.g., Yang et al., 2000] theoretically have no obvious limitations, but, in practice, require excessive computer resources. Therefore the ability to simulate the interaction of electromagnetic radiation with individual particles of various shape, size and morphology is probably the most critical factor in driving the advances in modeling of the optical properties of nonspherical aerosols.

[3] Thus the majority of approaches employed in aerosol retrievals to account for particle nonsphericity are based on modeling simulations limited in terms of particle size range, geometrical shapes, and compositions. As a result, comparisons of retrieval algorithms utilizing different assumptions for modeling optical properties of nonspherical aerosols are difficult and, quite often, inconclusive. For example, the benefits and limitations of using even the simplest nonspherical shapes, such as spheroids (ellipsoids of revolution), for modeling light scattering by nonspherical aerosol are not completely clear. Specifically, Mishchenko et al.

[1997] showed that a mixture of randomly oriented spheroids with different sizes and axis ratios can reproduce the flattening of the phase function at side scattering angles for desert dust – perhaps the main scattering feature associated with nonsphericity of aerosol particles. Therefore light scattering by spheroids has been used extensively in remote sensing applications [e.g., see Mishchenko et al., 2004b]. At the same time, there is no physical reason to expect all dust particles to be perfect spheroids, and, indeed, microphotographs of natural aerosols show a great variety of shapes, often different from spheroids. Therefore there are studies aimed at modeling desert dust scattering for more complex and, arguably, more realistic geometrical shapes [e.g., Yang et al., 2000; Kalashnikova and Sokolik, 2002, 2004]. However, such simulations require very long computation times and are not possible for the entire size range of desert dust aerosol. For example, the studies of Kalashnikova and Sokolik [2002, 2004] limit the calculations to particles with volume-equivalent radii smaller than 1 and $\sim 2 \mu\text{m}$ correspondingly, while both in situ and remote sensing observations suggest high concentrations of particles with radii up to $5 \mu\text{m}$ and greater in desert dust aerosol [e.g., see Arimoto et al., 1997; Li-Jones and Prospero, 1998; Dubovik et al., 2002a; Reid et al., 2003a, 2003b; Haywood et al., 2003]. This is why the spheroid approximation remains appealing from an operational perspective. Moreover, the following considerations can be listed as further motivations for the utilization and exploration of spheroid models:

[4] 1. A spheroid is the simplest nonspherical shape that can generalize the spherical shape (a sphere is a spheroid with an axis ratio $\epsilon = 1$). Accordingly, conventional spherical models of atmospheric aerosol can be easily generalized in terms of a model of randomly oriented spheroids with only one extra characteristic – the distribution of axis ratios (assuming, as the first-order approximation, that shape is independent of size).

[5] 2. The scattering of electromagnetic radiation by spheroids can be accurately simulated. For example, the *T*-matrix method provides an exact solution for light scattering by randomly oriented spheroids with different sizes, axis ratios, and complex refractive indices [Mishchenko and Travis, 1994]. The corresponding computer routine has calculation speed and range of applicability far superior to other available numerically exact routines.

[6] 3. The observations of scattering by real desert dust show a considerable degree of averaging of contributions from individual particles with different orientations, shapes, and compositions. Hence one can expect [Wiscombe and Mugnai, 1986; Bohren and Singham, 1991; Mishchenko et al., 1997] that specific shape details of a single particle may be insignificant after such an averaging and that scattering by an ensemble of particles can be approximated by that of a mixture of simplified particles (such as spheroids). For example, Min et al. [2005] used a hollow-sphere model to reproduce some scattering properties of desert dust and indicated that the exact shape used for modeling is unimportant to a certain degree as long as the particle model employed deviates from the perfect symmetry of a homogeneous sphere. Kahnert [2004] arrived at a similar conclusion based on his mimicking the scattering matrices of prisms by using simple geometrical shapes (spheres and spheroids).

[7] The limits of applicability of the spheroid model have been examined in several studies. For example, *Nousiainen and Vermeulen* [2003] and *Veihelmann et al.* [2004] analyzed the possibility of reproducing scattering matrices of mineral dust measured in the laboratory [*Volten et al.*, 2001] by theoretical simulations using spheroids. *Kahnert* [2004] examined the feasibility of employing a spheroid model for reproducing the scattering matrices of desert dust represented by 110 different types of particles with low symmetry (4- and 5-hedral prisms with different aspect ratios). These studies have demonstrated that spheroids are far superior to spheres in reproducing the laboratory measurements. However, at the same time, these studies have highlighted the difficulties in accounting for the contribution of spheroids with larger sizes and higher degrees of nonsphericity. Specifically, *Nousiainen and Vermeulen* [2003] and *Nousiainen et al.* [2006] did not consider particles with radii larger than 2.5 μm , *Kahnert* [2004] used 2.8 μm as the largest particle size, and *Veihelmann et al.* [2004] used a variable particle size cutoff as a function of aspect ratio (i.e., the greater the aspect ratio the smaller the cutoff size). The studies based on the measured scattering matrices [*Nousiainen and Vermeulen*, 2003; *Kahnert*, 2004] used only one (and the same) aerosol sample.

[8] Therefore more analyses are called for in order to understand better the limitations of the spheroid model. One of the major factors slowing such analyses is the necessity of committing to a substantial computation effort. For example, even the most advanced *T*-matrix code [*Mishchenko et al.*, 2002] slows down and becomes numerically unstable for highly elongated and flattened spheroids (i.e., aspect ratios exceeding 2–2.4) with size parameters $x (=2\pi r/\lambda)$ exceeding 40–60. As a consequence, the simulation of light scattering by spheroids that requires integrating spheroid extinction and scattering cross sections over both a wide range of sizes and aspect ratios is computationally much more demanding than simulations of light scattering by spherical particles. The same factor limits efforts aimed at the incorporation of spheroid models into remote sensing aerosol retrievals.

[9] In a recent paper, *Dubovik et al.* [2002b] proposed the use of kernel look-up tables for implementing quick and accurate simulations of spheroid phase functions. The present study describes further developments aimed primarily at modeling the entire scattering matrix of spheroids. Also, we discuss the use of the developed look-up tables in the validation of the spheroid model versus laboratory measurements of scattering matrices [*Volten et al.*, 2001]. Most importantly, we establish an approach that rigorously incorporates the shape distribution of aerosol particles into aerosol remote sensing applications. Therefore this paper demonstrates that the developed kernel look-up tables allow the use of a spheroid mixture as a generalized aerosol model (representing spherical, nonspherical, and mixed aerosols) in remote sensing retrievals of atmospheric aerosols. Specifically, the possibility of retrieving a complete set of aerosol parameters, including the complex refractive index and the size and shape distributions, from spectral and angular photopolarimetric observations using Sun/sky radiometers of the AERosol RObotic NETwork (AERONET) is discussed. The final section discusses the

possibility of using spheroid models in order to account for aerosol particle nonsphericity in lidar and satellite passive remote sensing measurements.

2. Scattering Matrix Modeling

[10] Photometric and polarization parameters of atmospheric radiation can be modeled by solving the vector radiative transfer equation for a plane-parallel multilayered atmosphere [*Hovenier et al.*, 2004; *Mishchenko et al.*, 2006]. Each layer is characterized by the extinction optical thickness τ_{ext} (describing combined scattering and absorption of directly transmitted light in the layer), single scattering albedo ω_0 (ratio of the scattering optical thickness τ_{scat} to τ_{ext}), and the scattering matrix $\mathbf{P}(\Theta)$. The latter describes the angular polarizing properties of a single-scattering event in the layer. Specifically, the transformation of the Stokes vector of the incident light into that of the scattering light is described by the following equation:

$$\begin{pmatrix} I_s \\ Q_s \\ U_s \\ V_s \end{pmatrix} \propto \begin{pmatrix} P_{11}(\Theta) & P_{12}(\Theta) & 0 & 0 \\ P_{12}(\Theta) & P_{22}(\Theta) & 0 & 0 \\ 0 & 0 & P_{33}(\Theta) & P_{34}(\Theta) \\ 0 & 0 & -P_{34}(\Theta) & P_{44}(\Theta) \end{pmatrix} \begin{pmatrix} I_i \\ Q_i \\ U_i \\ V_i \end{pmatrix}, \quad (1)$$

where Θ is the scattering angle, I , Q , U and V are the Stokes parameters [*van de Hulst*, 1957], and the subscripts “i” and “s” refer to the incident and scattered beams, respectively. The above scattering matrix of spheroids (as well as of any randomly oriented particles with a plane of symmetry) has a block-diagonal structure with six independent elements $P_{ii}(\Theta)$. This structure of the scattering matrix is also characteristic of any ensemble of randomly oriented particles with equal numbers of particles and their mirror counterparts [*van de Hulst*, 1957; *Mishchenko et al.*, 2002]. For homogeneous or radially inhomogeneous spheres (as particles of higher symmetry), the scattering matrix has only four independent elements (since $P_{11}(\Theta) = P_{22}(\Theta)$ and $P_{33}(\Theta) = P_{44}(\Theta)$). The element $P_{11}(\Theta)$ of the scattering matrix is called the scattering phase function and satisfies the following normalization condition:

$$\frac{1}{2} \int_0^\pi \sin(\Theta) P_{11}(\Theta) d\Theta = 1. \quad (2)$$

[11] The scattering properties of the atmospheric aerosol layer are modeled via the averaging of single-particle properties. For example, for homogeneous spherical aerosol one can write:

$$\tau_{\text{scat}}(\lambda) P_{ii'}(\lambda, \Theta) = \int_{r_{\min}}^{r_{\max}} C_{ii'}(\lambda, \Theta, n, k, r) \frac{dN(r)}{dr} dr, \quad (3)$$

$$\tau_{\text{ext/scat}}(\lambda) = \int_{r_{\min}}^{r_{\max}} C_{\text{ext/scat}}(\lambda, n, k, r) \frac{dN(r)}{dr} dr, \quad (4)$$

where $C_{ext}(\lambda, n, k, r)$, $C_{scat}(\lambda, n, k, r)$, and $C_{ii'}(\Theta, \lambda, n, k, r)$, denote, respectively, the cross sections of extinction, scattering and directional scattering corresponding to matrix elements $P_{ii'}(\Theta)$, λ – wavelength, n and k – real and imaginary parts of the refractive index, r – radius of the particle. $dN(r)/dr$ is the number size distribution of particles which determines particle concentrations as follows:

$$N(r_1; r_2) = \int_{r_1}^{r_2} \frac{dN(r)}{dr} dr, \quad (5)$$

where $N(r_1; r_2)$ is the total number of particles (in the atmospheric layer) with radii between r_1 and r_2 per unit lateral area. Equations (3) and (4) are written for the size distribution of columnar aerosol particle number concentration; however, practical algorithms assuming spherical particles are usually designed to retrieve the distribution of surface area or volume of aerosol particles because light scattering by an ensemble of small particles depend on the particle surface area or volume [cf. *Bohren and Huffman*, 1983] rather than on the number concentration. In addition the cross sections $C_{...}(\dots, r)$ show much smoother variability for equal relative steps $\Delta r/r$ (i.e., for equal logarithmic steps, since $dr/r = d \ln r$) than for equal absolute steps Δr . For example, the SkyRad inversion [*Nakajima et al.*, 1996] and AERONET operational inversion algorithm [*Dubovik and King*, 2000] are set to retrieve the aerosol volume distribution $dV/d \ln r$. The integration over particle sizes can be rewritten (in equations (3) and (4)) in terms of $dV/d \ln r$ as follows:

$$\int_{r_{\min}}^{r_{\max}} C_{...}(\dots, r) \frac{dN(r)}{dr} dr = \int_{\ln r_{\min}}^{\ln r_{\max}} \frac{C_{...}(\dots, r)}{v(r)} \frac{dV(r)}{d \ln r} d \ln r, \quad (6)$$

where $v(r)$ is the volume of particle with radius r and $dV(r)/d \ln r$ denotes volume size distribution of particles. The latter determines particle volume concentrations as follows:

$$V(r_1, r_2) = \int_{r_1}^{r_2} \frac{dV(r)}{dr} dr = \int_{\ln r_1}^{\ln r_2} \frac{dV(r)}{d \ln r} d \ln r, \quad (7)$$

where $V(r_1; r_2)$ is the total volume of particles with radii between r_1 and r_2 in the atmospheric layer per unit lateral area. The size distributions $dV/d \ln r$ and dN/dr are related as follows:

$$\frac{dV(r)}{d \ln r} = v(r) \frac{dN(r)}{d \ln r} = v(r) r \frac{dN(r)}{dr}. \quad (8)$$

The integrations on the left- and right-hand sides of equation (6) are equivalent in general, however the expression on the right-hand side of equation (6) requires fewer nodal points for numerical integration.

[12] The spheroid is a geometrical shape formed by rotating an ellipse about its minor axis (oblate spheroid) or its major axis (prolate spheroid), and is uniquely

described by two parameters instead of one (radius) used for spheres. Specifically, *Mishchenko et al.* [2002] suggest using the axis ratio ε ($\varepsilon = a/b$, a – axis of spheroid rotational symmetry, b – axis perpendicular to the axis of spheroid rotational symmetry) and r – radius of the sphere having the same surface area or volume (we use r – radius of the volume-equivalent sphere for consistency with the *Dubovik and King* [2000] algorithms that retrieve the particle volume distribution). In principle, the size distribution of spheroids should be a function of two variables ε and r ; that is, one can write:

$$V(r_1, r_2; \varepsilon_1, \varepsilon_2) = \int_{\varepsilon_1}^{\varepsilon_2} \int_{r_1}^{r_2} v(r) \frac{d^2 N(\varepsilon, r)}{d\varepsilon dr} dr d\varepsilon, \quad (9)$$

where $v(r)$ is the volume of the sphere with radius r ; $V(r_1, r_2; \varepsilon_1, \varepsilon_2)$ is the total volume of spheroids with axis ratios between ε_1 and ε_2 and with volumes between $v(r_1)$ and $v(r_2)$ in the atmospheric layer per unit lateral area; $d^2 N(\varepsilon, r)/d\varepsilon dr$ is the differential number size and axis ratio distribution of spheroids.

[13] *Mishchenko et al.* [1997] showed that the simplest model with the same axis ratio distribution for spheroids of all sizes can adequately reproduce the phase functions measured for desert dust. This assumption is in agreement with the results of in situ studies of Saharan dust which showed that shape factors and aspect ratios do not have pronounced size dependence [*Reid et al.*, 2003b]. (Aspect ratio ε' is the ratio of the largest to the smallest particle dimensions, therefore the relation to axis ratio ε is $\varepsilon' = \varepsilon$ (for prolate spheroids) and $\varepsilon' = 1/\varepsilon$ (for oblate spheroids).) The spheroid distribution in an atmospheric layer can be described using two independent distributions and, instead of equation (9), one can write:

$$\begin{aligned} \int_{\varepsilon_1}^{\varepsilon_2} \int_{r_1}^{r_2} v(r) \frac{d^2 N(\varepsilon, r)}{d\varepsilon dr} dr d\varepsilon &\approx \int_{\varepsilon_1}^{\varepsilon_2} \int_{r_1}^{r_2} v(r) \frac{dN(r)}{dr} \frac{dn(\varepsilon)}{d\varepsilon} dr d\varepsilon \\ &= \int_{\ln \varepsilon_1}^{\ln \varepsilon_2} \int_{\ln r_1}^{\ln r_2} \frac{dV(r)}{d \ln r} \frac{dn(\varepsilon)}{d \ln \varepsilon} d \ln r d \ln \varepsilon, \end{aligned} \quad (10)$$

where $dN(r)/dr$, $dV(r)/dr$ and $dV(r)/d \ln r$ are the number and volume distributions of the spheroids as a function of r (radius of the sphere with equivalent volume) written in absolute and logarithmic scale of r ; $dn(\varepsilon)/d\varepsilon$ and $dn(\varepsilon)/d \ln \varepsilon$ ($=\varepsilon dn(\varepsilon)/d\varepsilon$) are the distributions of the spheroid axis ratios (assumed the same for all r) written in absolute and logarithmic scale of ε . In the following analysis, we use $dn(\varepsilon)/d \ln \varepsilon$ because the logarithmic scale allows numerical integration over $\ln \varepsilon$ with constant step $\Delta \ln \varepsilon$, whereas using the absolute scale makes the integration more complicated since ranges of variability of ε are very different for oblate ($0 < \varepsilon < 1$) and prolate ($1 < \varepsilon$) spheroids. Hence, for τ_{scat} , τ_{ext} , and elements $\tau_{scat} P_{ii'}(\Theta)$, one can write instead of equations (2) and (3):

$$\begin{aligned} \tau_{scat} P_{ii'}(\Theta; \lambda) &= \int_{\ln \varepsilon_{\min}}^{\ln \varepsilon_{\max}} \int_{\ln r_{\min}}^{\ln r_{\max}} \frac{C_{ii'}(\dots, \varepsilon, r)}{v(r)} \\ &\cdot \frac{dn(\varepsilon)}{d \ln \varepsilon} \frac{dV(r)}{d \ln r} d \ln r d \ln \varepsilon, \end{aligned} \quad (11)$$

and

$$\tau_{scat/ext} = \int_{\ln \varepsilon_{\min}}^{\ln \varepsilon_{\max}} \int_{\ln r_{\min}}^{\ln r_{\max}} \frac{C_{ext/scat}(\dots, \varepsilon, r)}{v(r)} \cdot \frac{dn(\varepsilon)}{d \ln \varepsilon} \frac{dV(r)}{d \ln r} d \ln r d \ln \varepsilon, \quad (12)$$

where $\tau_{scat} P_{iir} = \tau_{scat} P_{iir}(\Theta, \lambda)$ and $\tau \dots$ denotes τ_{scat} or τ_{ext} ; $C_{ext}(\lambda, n, k, \varepsilon, r)$, $C_{scat}(\lambda, n, k, \varepsilon, r)$, and $C_{iir}(\Theta, \lambda, n, k, \varepsilon, r)$ denote the spheroid cross sections of extinction, scattering and directional scattering, respectively. For convenience of interpretation we use the following normalization of the distributions $dV(r)/d \ln r$ and $dn(\varepsilon)/d \ln \varepsilon$:

$$V_{total} = \int_{\ln r_{\min}}^{\ln r_{\max}} \frac{dV(r)}{d \ln r} d \ln r, \quad \text{and} \quad 1 = \int_{\ln \varepsilon_{\min}}^{\ln \varepsilon_{\max}} \frac{dn(\varepsilon)}{d \ln \varepsilon} d \ln \varepsilon. \quad (13)$$

Accordingly, $dV(r)/d \ln r$ describes the size distribution of the total aerosol volume in the atmospheric layer and $dn(\varepsilon)/d \ln \varepsilon$ describes the relative representation (weight) of the spheroids with different axis ratios.

[14] In order to reduce computation time, remote-sensing algorithms based on equations (10) and (11) often use precomputed look-up tables of aerosol scattering properties. Utilizing look-up tables of scattering kernels is another efficient and more flexible way for approximating aerosol single-scattering properties [e.g., see *Twomey*, 1977; *King et al.*, 1978; *Dubovik and King*, 2000]. For example, following *Dubovik et al.* [2002b] the single-scattering properties of randomly oriented spheroids can be approximated as follows:

$$\begin{aligned} & \int_{\ln \varepsilon_{\min}}^{\ln \varepsilon_{\max}} \int_{\ln r_{\min}}^{\ln r_{\max}} \frac{C_{\dots}(\dots, \varepsilon, r)}{v(r)} \frac{dn(\varepsilon)}{d \ln \varepsilon} \frac{dV(r)}{d \ln r} d \ln r d \ln \varepsilon \\ &= \sum_{p,k} \frac{dn(\varepsilon_p)}{d \ln \varepsilon} \frac{dV(r_k)}{d \ln r} K_{\dots}(\dots, \varepsilon_p, r_k), \end{aligned} \quad (14)$$

where $dn(\varepsilon_p)/d \ln \varepsilon$ and $dV(r_k)/d \ln r$ are the values of the size distributions $dV(r)/d \ln r$ and $dn(\varepsilon)/d \ln \varepsilon$ given at discrete logarithmically equidistant points:

$$\varepsilon_p (p = 1, \dots, N_\varepsilon) \text{ and } r_k (k = 1, \dots, N_r),$$

$$\Delta \ln \varepsilon = \ln \varepsilon_{p+1} - \ln \varepsilon_p = \text{const}, \quad (15)$$

$$\Delta \ln r = \ln r_{k+1} - \ln r_k = \text{const},$$

the kernels $K_{ext}(\lambda, n, k, \varepsilon_p, r_k)$, $K_{scat}(\lambda, n, k, \varepsilon_p, r_k)$, $K_{iir}(\Theta, \lambda, n, k, \varepsilon_p, r_k)$ are simulated as follows:

$$\begin{aligned} K_{\dots}(\dots, \varepsilon_p, r_k) &= \int_{\Delta \ln r_k} \int_{\Delta \ln \varepsilon_p} \frac{C_{\dots}(\dots, \varepsilon, r)}{v(r)} d \ln \varepsilon d \ln r \\ &\approx \int_{\Delta \ln r_k} \frac{C_{\dots}(\dots, \varepsilon_p, r)}{v(r)} d \ln r, \end{aligned} \quad (16)$$

where $\Delta \ln \varepsilon_p$ and $\Delta \ln r_k$ denote integration intervals $[\ln \varepsilon_p - (\Delta \ln \varepsilon)/2, \ln \varepsilon_p + (\Delta \ln \varepsilon)/2]$ and $[\ln r_k - (\Delta \ln r)/2, \ln r_k + (\Delta \ln r)/2]$, respectively. Equation (15) exploits the assumption of constant size distributions $dV(r)/d \ln r$ and $dn(\varepsilon)/d \ln \varepsilon$ over the integration intervals around nodal points r_k and ε_p :

$$\begin{aligned} \frac{dV(r)}{d \ln r} &= \frac{dV(r_k)}{d \ln r} \quad - \quad \text{for } r \text{ in } (\ln r_k - \Delta \ln r/2) \leq \ln r < (\ln r_k + \Delta \ln r/2), \\ \frac{dn(\varepsilon)}{d \ln \varepsilon} &= \frac{dn(\varepsilon_p)}{d \ln \varepsilon} \quad - \quad \text{for } \varepsilon \text{ in } (\ln \varepsilon_p - \Delta \ln \varepsilon/2) \leq \ln \varepsilon < (\ln \varepsilon_p + \Delta \ln \varepsilon/2). \end{aligned} \quad (17)$$

The above assumption is illustrated in Figure 1. Equation (17) and Figure 1 show the simplest way of approximating the function $dV(r)/d \ln r$ by using a limited number of discrete points of $dV(r_k)/d \ln r$. We generally use more accurate trapezoidal approximations that assume a linear dependence of the function $dV(r)/d \ln r$ between discrete points:

$$\frac{dV(r)}{d \ln r} = A \ln r + B \quad (r_k \leq r \leq r_{k+1}), \quad (18)$$

where the coefficients A and B should coincide with values of $dV(r_{k+1})/d \ln r$ and $dV(r_k)/d \ln r$. *Twomey* [1977] describes in detailed the use of the trapezoidal approximation in kernel calculations. Applying the same approach (also see *Dubovik and King* [2000]) for computing spheroid kernels, equation (16) can be written as follows:

$$\begin{aligned} K_{\dots}(\dots, \varepsilon_p, r_k) &\approx \int_{\ln r_k}^{\ln r_{k+1}} \frac{\ln r_k - \ln r}{\Delta \ln r} \frac{C_{\dots}(\dots, \varepsilon_p, r)}{v(r)} d \ln r \\ &+ \int_{\ln r_{k-1}}^{\ln r_k} \frac{\ln r - \ln r_{k-1}}{\Delta \ln r} \frac{C_{\dots}(\dots, \varepsilon_p, r)}{v(r)} d \ln r. \end{aligned} \quad (19)$$

In addition, both equations (16) and (19) are based on the following assumption:

$$\begin{aligned} C_{\dots}(\dots, \varepsilon, r) &\approx C_{\dots}(\dots, \varepsilon_p, r) \quad - \quad \text{for } \varepsilon \text{ in } (\ln \varepsilon_p - \Delta \ln \varepsilon/2) \leq \ln \varepsilon < (\ln \varepsilon_p + \Delta \ln \varepsilon/2). \end{aligned} \quad (20)$$

This approximation is needed for decreasing the number of kernel computations. In addition, *Mishchenko et al.* [1997] demonstrated that the optical cross sections of randomly oriented spheroids are rather smooth functions of size and that the aspect ratio integrations with moderate step size ($\Delta \varepsilon = 0.2$) are virtually indistinguishable from those with a much smaller integration step size ($\Delta \varepsilon = 0.05$). Thus, in our study, equations (15)–(19) were used as the basic assumptions and the single-scattering properties of randomly oriented spheroids were approximated as follows:

$$\tau_{scat} P_{iir}(\Theta, \lambda) \approx \sum_{p,k} \frac{dn(\varepsilon_p)}{d \ln \varepsilon} \frac{dV(r_k)}{d \ln r} K_{iir}(\Theta, \lambda, n, k, \varepsilon_p, r_k), \quad (21)$$

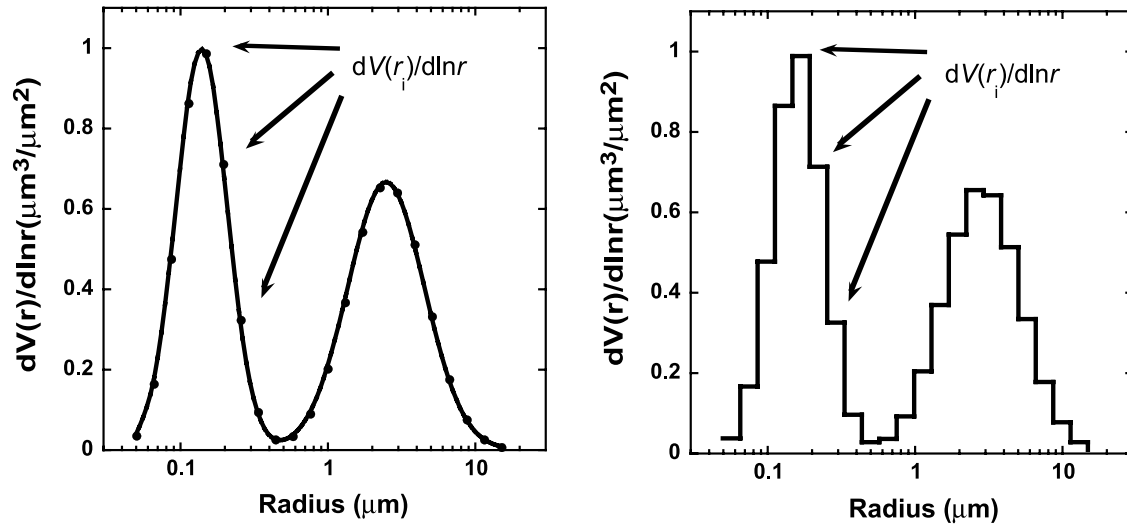


Figure 1. Illustration of the approximation used for the size distribution $dV(r)/d\ln r$ in equation (16). (left) Original size distribution and (right) approximated size distribution.

and

$$\tau_{ext/scat} \approx \sum_{p,k} \frac{dn(\varepsilon_p)}{d\ln \varepsilon} \frac{dV(r_k)}{d\ln r} K_{ext/scat}(\lambda, n, k, \varepsilon_p, r_k). \quad (22)$$

[15] Equations (21) and (22) are efficient in multiple simulations of scattering by polydisperse aerosols with variable size distributions because the integration over a particle size range is replaced by using the matrices $K_{ext}(\dots)$ and $K_{scat}(\dots)$ which are precomputed once with high accuracy. This approximation is helpful in improving the time performance of spherical-particle retrievals, even though Lorenz-Mie computations are very fast. For the retrievals of nonspherical particles, the use of the above approximations is critical because direct simulations of nonspherical scattering in the inversion code would be unacceptably time consuming.

[16] The dependence of the kernel matrices $K_{ext}(\lambda, n, k, \varepsilon_p, r_k)$, $K_{scat}(\lambda, n, k, \varepsilon_p, r_k)$, $K_{ii}(\Theta, \lambda, n, k, \varepsilon_p, r_k)$ on the real, n , and imaginary, k , parts of the refractive index can be parameterized by a look-up table covering the range of values characteristic for atmospheric aerosol. In the algorithm by Dubovik and King [2000], the kernels $K_{ext}(\lambda, n, k, r_k)$, $K_{scat}(\lambda, n, k, r_k)$ and the kernel of the phase function $K_{11}(\Theta, \lambda, n, k, r_k)$ were computed for spheres at $(N_n \times N_k \times N_r)$ grid points. The $N_n = 15$ equidistant points for n , the $N_k = 15$ logarithmically equidistant points for k , and the $N_r = 22$ logarithmically equidistant bins for r sampled the following ranges of the complex refractive index and particle size: $1.33 \leq n \leq 1.6$, $0.0005 \leq k \leq 0.5$ and $0.05 \leq r \leq 15$ (μm). For values of n and k between the sampling points, the kernels $K_{ext}(\dots, n, k, r_k)$ were linearly interpolated on the logarithmic scale. Dubovik and King [2000] calculated the kernels for four AERONET sky-channel wavelengths $N_\lambda = 4$ ($\lambda_i = 0.44, 0.67, 0.87$, and 1.02 μm). The scattering matrix kernel was calculated for 35 scattering angles $N_\Theta = 35$, optimized for AERONET measurements geometry. This set of angles includes all scattering angles corresponding to the AERONET almucantar observations

for the solar zenith angle 60° . This approach allowed fast modeling of atmospheric radiances with an accuracy of $\sim 1 - 2\%$ at the AERONET sky-channel wavelengths. The studies by Dubovik et al. [2002b] complemented the Lorenz-Mie kernels of Dubovik and King [2000] with the kernels of randomly oriented spheroids. The kernel look-up tables of Dubovik et al. [2002b] included spheres as well as both elongated (aspect ratios $\varepsilon_p = 0.4; 0.48; 0.58; 0.7; 0.83$) and flattened ($\varepsilon_p = 1.2; 1.45; 1.7; 2.1; 2.5$) spheroids; that is, the matrices $K_{ext}(\lambda, n, k, \varepsilon_p, r_k)$, $K_{scat}(\lambda, n, k, \varepsilon_p, r_k)$, $K_{11}(\Theta, \lambda, n, k, \varepsilon_p, r_k)$ were calculated for $N_\varepsilon = 11$ logarithmically equidistant points ($\Delta \ln \varepsilon = 0.2$) for axis ratios in the range: $0.4 \leq \varepsilon \leq 2.5$.

[17] In the present study, the spheroid kernels $K_{ii}(\Theta, \lambda, n, k, \varepsilon_p, r_k)$ were generated for all elements of the scattering matrix shown in equation (1) at 25 logarithmically equidistant points covering the axis-ratio range from 0.3 to 3.0. In addition, for improving the accuracy of the approximation (21), the matrices $K_{ii}(\Theta, \lambda, n, k, \varepsilon_p, r_k)$ were computed with an angular resolution of 1° ($N_\Theta = 180$), instead of $N_\Theta = 35$ fixed angles used in the previous studies. Also, the size range covered by the kernels was significantly expanded; specifically, all kernels were computed at $N_x = 41$ logarithmically equidistant points for size parameter x ($=2\pi r/\lambda$) in the following range: $0.012 \leq x$ ($=2\pi r/\lambda$) ≤ 625 . The computation of spheroid scattering in such a wide range of size parameters was performed using two different methods, as suggested in a previous study [Dubovik et al., 2002b]. Specifically, for the majority of computations we used the advanced T -matrix code [Mishchenko et al., 2002], which provides an exact solution for electromagnetic scattering by randomly oriented spheroids. The specific size limit for stable performance of the T -matrix code depends on ε . The limit decreases as ε departs from 1 toward both larger and smaller values (Veihelmann et al. [2004] provide a table illustrating this tendency). Also, the size limit can be different for the same ε but different n and k . Thus, in this study, we performed calculations by the T -matrix code up to the convergence point. From that point onward we continued simulations using the approximate geometric-optics-

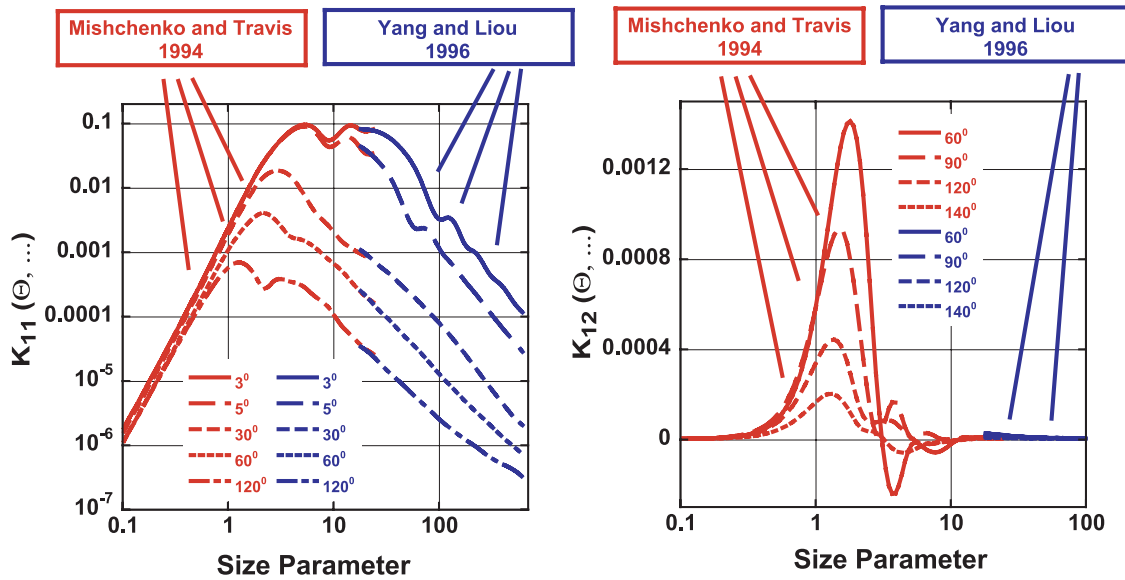


Figure 2. Elements of the kernel matrices $K_{11}(\Theta, \lambda, n, k, \varepsilon_p, r_k)$ and $K_{12}(\Theta, \lambda, n, k, \varepsilon_p, r_k)$ at different scattering angles for prolate randomly oriented spheroids ($\varepsilon = \sim 2.7$, $n = 1.53$, $k = 0.003$). The red and blue curves show the results obtained with the T -matrix code [Mishchenko and Travis, 1994] and the Yang and Liou [1996] method, respectively.

integral-equation method of Yang and Liou [1996]. This method uses the ray-tracing procedure to find the field on the particle surface. The latter is then transformed to the far field using an equivalence theorem. This geometric-optics-integral-equation approach is applicable to smaller particles than the conventional geometric optics method and is expected to provide accurate τ_{ext} , τ_{scat} and $P_{ii}(\Theta)$ values for spheroids with x larger than ~ 30 – 40 . Thus, by supplementing the T -matrix method with the geometric-optics-integral-equation technique we generated the kernel matrices for spheroids in a wide range of x .

[18] Figure 2 illustrates the elements of $K_{11}(\Theta, \lambda, n, k, \varepsilon_p, r_k)$ and $K_{12}(\Theta, \lambda, n, k, \varepsilon_p, r_k)$ calculated using these two codes and shows good agreement for the range of size parameters where both codes are applicable ($x \sim 30$ – 50). In general, comparisons of simulations of the kernels using the two codes show good agreement (similar to the one shown in Figure 2) of $K_{11}(\dots, \varepsilon_p, r_k)$ for the whole range of scattering angles and for all complex refractive indices considered. Some deterioration of accuracy was observed for the method of Yang and Liou [1996] in simulations of $K_{11}(\dots, \varepsilon_p, r_k)$ for backscattering angles ($175^\circ < \Theta \leq 180^\circ$). The agreement of $K_{12}(\dots, \varepsilon_p, r_k)$ simulated by the two different codes is good for scattering angles between 30° and 160° where the values of the degree of linear polarization ($-P_{12}(\Theta, \lambda)/P_{11}(\Theta, \lambda)$) are the highest. For the kernels $K_{22}(\dots, \varepsilon_p, r_k)$, $K_{33}(\dots, \varepsilon_p, r_k)$ and $K_{44}(\dots, \varepsilon_p, r_k)$ we observed the same tendencies in the agreement of the two methods as for the phase function kernel $K_{11}(\dots, \varepsilon_p, r_k)$. For the kernel $K_{34}(\dots, \varepsilon_p, r_k)$ the tendencies are similar to those observed for $K_{12}(\dots, \varepsilon_p, r_k)$ (good agreement for $30^\circ < \Theta \leq 160^\circ$ and slightly worse for smaller and larger scattering angles).

[19] The simulation of the kernel matrices at all of the $N_n \times N_k \times N_x \times N_\varepsilon$ sampling points requires a very long computational time. Therefore the number of points for integration in equation (19) was chosen to moderate the computational time. Specifically, simulations for $\varepsilon = 1$

where performed with the fast Lorenz-Mie code using a large number of integration points (~ 1000) for each size bin ($\ln r_i \pm \Delta \ln r/2$). The T -matrix method is based on the analytical averaging over spheroid orientations and, therefore, is fast. However, for x and/or ε close to the numerical instability thresholds, the T -matrix computations slow down considerably. At the same time, the size dependence of the optical cross sections for randomly oriented spheroids with $\varepsilon \geq 1.2$ is rather smooth, and the integration step can be increased without loss of accuracy. Therefore the T -matrix simulations in equation (19) were performed with a smaller number of integration points (~ 100) for each size bin ($\ln r_i \pm \Delta \ln r/2$). The method of Yang and Liou [1996] requires longer computation time since the method integrates numerically the scattering by each single particle over a large number of orientations (20,000 used here). After that integration, the size dependence of the scattering cross section of spheroids is smooth, especially when ε is very different from 1 (e.g., for an ε value at which the T -matrix code becomes unstable we use the approximate code). Therefore, to moderate the computational time, only 20 points were used for each size bin ($\ln r_i \pm \Delta \ln r/2$) in the equation (19) integration over all sizes.

[20] Thus, with more than a year of CPU time expenditure, the spheroids kernels $K_{ext}(\lambda, n, k, \varepsilon_p, r_k)$, $K_{scat}(\lambda, n, k, \varepsilon_p, r_k)$ and $K_{ii}(\Theta, \lambda, n, k, \varepsilon_p, r_k)$ were simulated for the following ranges of aerosol parameters:

$$1.33 \leq n \leq 1.6,$$

$$0.0005 \leq k \leq 0.5,$$

$$0.3 \leq \varepsilon \leq 3.0, \quad (23)$$

$$0.012 \leq x (= 2\pi r/\lambda) \leq 625,$$

$$\Delta 1^\circ - \text{resolution for } K_{ii}(\Theta, \lambda, n, k, \varepsilon_p, r_k).$$

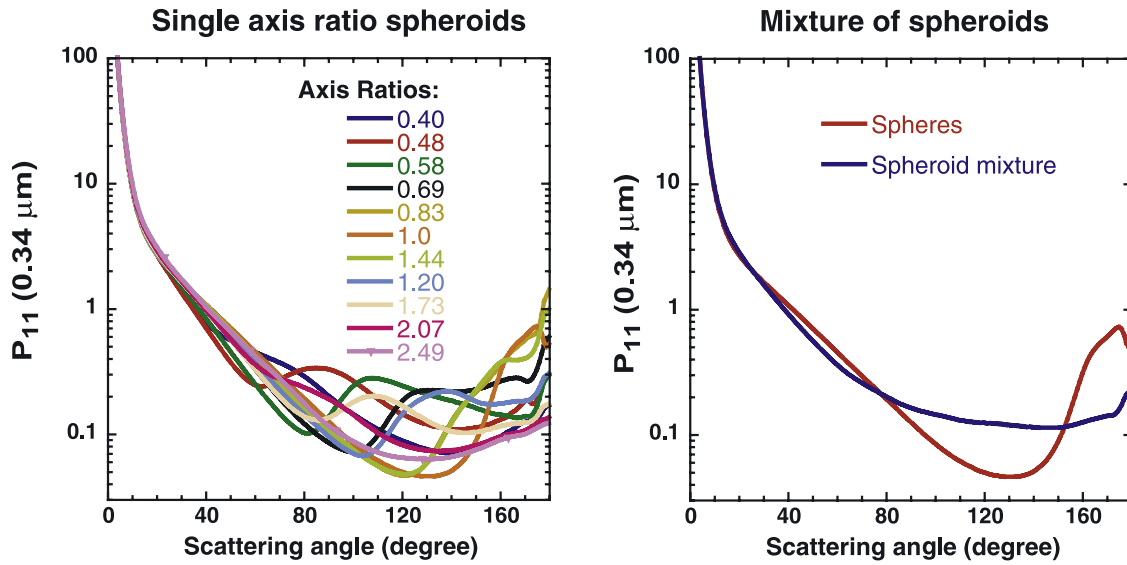


Figure 3. (left) $P_{11}(\Theta, \lambda, \varepsilon_p)$, the phase functions of desert dust simulated for the spheroid model with 11 single axis ratios ε_p . (right) $P_{11}(\Theta, \lambda)$, the phase function of desert dust simulated as a mixture of spheroids with different ε_p (blue line). $P_{11}(\Theta, \lambda)$ is obtained by integrations of $P_{11}(\Theta, \lambda, \varepsilon_p)$ with axis ratio distribution $dn(\varepsilon_p)/d\ln\varepsilon$. Also shown is $P_{11}(\Theta, \lambda)$, the phase function of desert dust simulated under assumption of spherical particles (red line). All phase functions were simulated with the size distribution and complex refractive index of the Saudi Arabia desert dust model [Dubovik *et al.*, 2002a].

For effectiveness and flexibility of applying these kernels, a user-friendly software package has been designed. This software allows quick simulation of τ_{ext} , τ_{scat} and $P_{ii}(\Theta)$ from known n , k , $dV(r_k)/d\ln r$, and $dn(\varepsilon_p)/d\ln\varepsilon$. Figures 3 and 4 illustrate using this spheroid approximation for modeling the phase function and degree of linear polarization of nonspherical dust.

[21] Several tests were conducted in order to estimate the accuracy of τ_{ext} , τ_{scat} and $P_{ii}(\Theta)$ provided by the software. The tests for typical tropospheric aerosols [Dubovik *et al.*, 2002a] have shown that for τ_{ext} and τ_{scat} the error is below 1% and for $P_{ii}(\Theta)$ in the range of $\Theta \leq 175^\circ$ the error is below ~ 1 –3%. For the large scattering angles $\Theta > 175^\circ$ the accuracy of simulated $P_{ii}(\Theta)$ decreases, which is due to accuracy limitations of the Yang and Liou [1996] method. To estimate the possible impact of these limitations, we compared the software output with the following general relationships for $P_{ii}(\Theta)$ in the exact backscattering direction [Mishchenko and Hovenier, 1995; Hovenier and van der Mee, 2000]:

$$\begin{aligned} P_{22}(180^\circ) &= -P_{33}(180^\circ), \\ P_{12}(180^\circ) &= P_{34}(180^\circ) = 0, \\ P_{44}(180^\circ) &= P_{11}(180^\circ) - 2 P_{22}(180^\circ). \end{aligned} \quad (24)$$

The comparisons showed that the first two relationships are satisfied with an accuracy better than 1–3% of $P_{11}(180^\circ)$. The last relation was satisfied with significantly lower accuracy for large spheroids with small and high axis ratios ($\varepsilon < 0.7$ or $\varepsilon > 1.45$). Specifically, for simulations using the size distribution and refractive index observed for Saudi Arabian dust [Dubovik *et al.*, 2002a] this relation was satisfied with an accuracy of only 10–15% at shorter visible

wavelengths ($\sim 0.44 \mu\text{m}$). Also, it should be noted that the limits of the ranges given by equation (23) are subject to future reevaluation and expansion (for complex refractive index in particular).

[22] When designing the kernels, we used the scale invariance rule [Mishchenko *et al.*, 2002, 2006]. According to this rule, τ_{ext} , τ_{scat} and $P_{ii}(\Theta)$ for randomly oriented spheroids are functions of size parameter x ; that is, these characteristics are identical for all couplets (size, wavelength) corresponding to the same size parameter $x = 2\pi r/\lambda$. Accordingly, by using a single look-up table the simulations can be performed for any λ and r_k within the range of x given by equation (23). Several options were included in the package for improving the speed of producing τ_{ext} , τ_{scat} and $P_{ii}(\Theta)$ from the kernels. For example, it is possible to create subset of kernels for user specified sets of angles and r_k . Also, the user can fix the axis ratio distribution $dn(\varepsilon_p)/d\ln\varepsilon$ and use only n , k , $dV(r_k)/d\ln r$. As a result, this kernel based package allows very fast (< 1 s) simulations of τ_{ext} , τ_{scat} and $P_{ii}(\Theta)$ (see sections 3 and 4). The kernels and software package with a detailed description of its functions is publicly available from the lead author upon request.

3. Inverting Measured Scattering Matrices

3.1. General Concept of Scattering Matrix Inversion

[23] Using spheroid kernel look-up tables can be beneficial for a number of applications involving the modeling of light scattering by nonspherical particles. Additionally, significant flexibility can be added to studies aimed at validation of the spheroid approximation against measurements or for comparison to more sophisticated calculations involving more diverse models of particle shape. For example, in contrast to previous studies that compared measured scattering matrices [Nousiainen and Vermeulen,

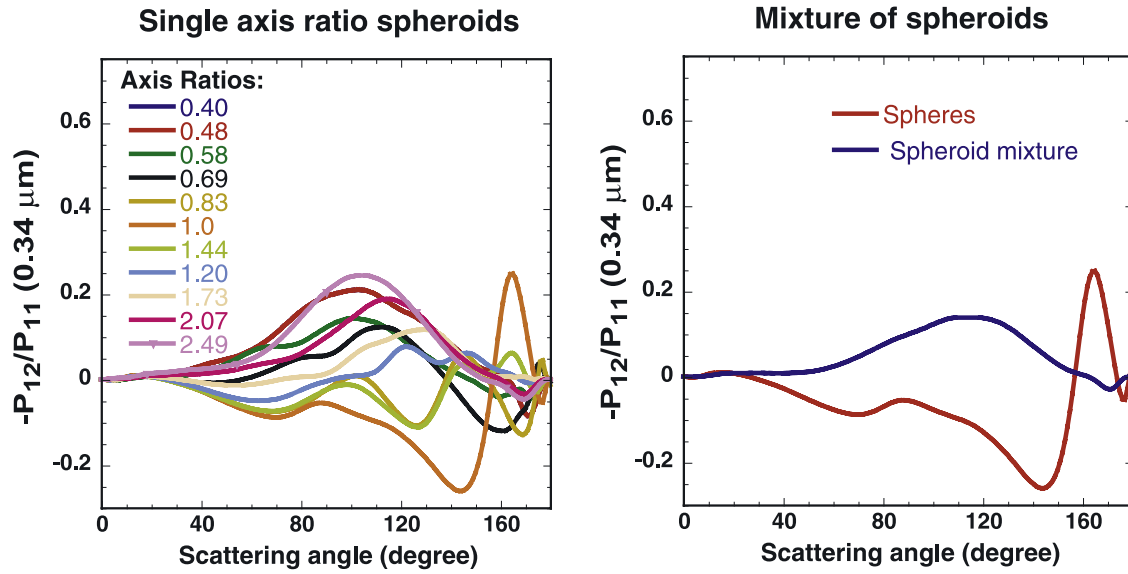


Figure 4. (left) $-P_{12}(\Theta, \lambda, \epsilon_p)$, the degree of linear polarization of desert dust simulated for the spheroid model with 11 single axis ratios ϵ_p . (right) $P_{12}(\Theta, \lambda)$, the degree of linear polarization of desert dust simulated as a mixture of spheroids with different ϵ_p (blue line). $-P_{12}(\Theta, \lambda)$ is obtained by integrations of $P_{11}(\Theta, \lambda, \epsilon_p)$ with the axis ratio distribution $dn(\epsilon_p)/d\ln\epsilon$. Also shown is $P_{11}(\Theta, \lambda)$, the degree of linear polarization of desert dust simulated under the assumption of spherical particles (red line). All $P_{12}(\Theta, \lambda)$ were simulated with the size distribution and complex refractive index of the Saudi Arabia desert dust model [Dubovik *et al.*, 2002a].

2003; Veihelmann *et al.*, 2004] to ones simulated with the *T*-matrix technique, the use of precomputed kernels allows the inclusion of larger particles and multiple repetition of the spheroid calculations (with different aerosol parameters) without significant computational time expense. Therefore fitting the measurement results can be accomplished not only by using forward simulations (as in the studies by Nousiainen and Vermeulen [2003] and Veihelmann *et al.* [2004]), but also efficiently by employing an inversion approach (e.g., an inversion was employed with similar purpose in the studies by Kahnert [2004], Min *et al.* [2005], and Nousiainen *et al.* [2006]).

[24] Indeed, laboratory measurements [Volten *et al.*, 2001, 2005; Muñoz *et al.*, 2001, 2004; Hovenier *et al.*, 2003] provide unique experimental information about polarization properties of several samples of nonspherical aerosol. The design and implementation of these measurements have involved extensive theoretical and experimental efforts. Therefore an elaborate consideration of all sources of uncertainties can be beneficial in the analysis and use of such observations.

[25] Specifically, in order to understand if spheroids can reproduce the measurements within given uncertainty limits, one needs to know and be able to analyze all uncertainties in both the measurements and the assumed aerosol parameters (size distribution, refractive index, and shape distribution). The inversion that accounts for differences in accuracy levels of both the measurements and the a priori assumptions is an adequate tool to address all those uncertainties in the comparisons of measurements with complex modeling (see theoretical considerations by Dubovik [2004]).

[26] Thus we have developed an inversion algorithm that retrieves aerosol properties via fitting the measured scatter-

ing matrices using spheroid kernels. As shown in the diagram of inversion logistics (Figure 5), the algorithm assumes aerosol particles as spheroids and retrieves $dV(r_k)/d\ln r$, n , k and $dn(\epsilon_p)/d\ln\epsilon$. The technical details of the inversion implementation are similar to those used in the aerosol retrieval algorithm by Dubovik and King [2000]. The main concept employed in the algorithm reduces the inversion to using a multiterm Least Squares Method (LSM) for solving the combined system of equations (for details of the inversion methodology see also Dubovik [2004]). Here the inversion of the scattering matrix (Figure 5) solves the following system of equations:

$$\begin{cases} \mathbf{f}^* = \mathbf{f}(\mathbf{a}) + \Delta_{\mathbf{f}} \\ \mathbf{0}^* = \mathbf{G} \mathbf{a} + \Delta_{\mathbf{g}}, \\ \mathbf{a}^* = \mathbf{a} + \Delta_{\mathbf{a}} \end{cases} \quad (25)$$

where the first equation corresponds to the scattering matrix measurements. The second equation represents a priori smoothness constraints on retrieved characteristics that are applied for eliminating of unrealistic strongly oscillating dependencies in the retrieved characteristic. Specifically, assuming zeros ($\mathbf{0}^*$ – zero vector) for derivatives of retrieved aerosol characteristics allows elimination of the strongly oscillating solutions with high derivatives (see detailed discussion by Dubovik and King [2000] and Dubovik [2004]). The matrix \mathbf{G} is composed of coefficients allowing the numerical estimates of derivatives of function $y(x)$ using discrete values $a_i = y(x_i)$. Such constraints are used for smoothing distributions of $dV(r_k)/d\ln r$ and $dn(\epsilon_p)/d\ln\epsilon$, and for smoothing spectral dependencies of the real

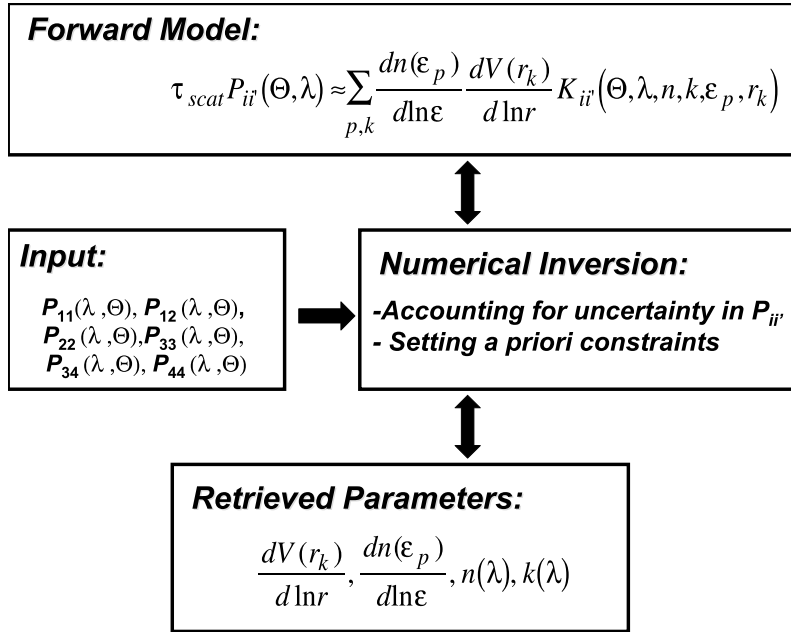


Figure 5. Illustration of inversion logistics in the algorithm developed for scattering matrix inversion.

and imaginary parts $n(\lambda)$ and $k(\lambda)$ of the refractive index (if scattering matrices are measured at several wavelengths). The third line in equation (25) shows the possibility of using a priori constraints on actual values of any retrieved parameter a_i and \mathbf{a}^* is vector of a priori estimates of a_i . The symbols $\Delta \dots$ denote the uncertainty in the measurements \mathbf{f}^* or a priori constraints on $\mathbf{0}^*$ and \mathbf{a}^* . For optimized accounting of those uncertainties, the solution of equation (25) is performed via minimization of the following quadratic form:

$$2\Psi(\mathbf{a}) = (\mathbf{f}(\mathbf{a}) - \mathbf{f}^*)^T \mathbf{W}_f^{-1} (\mathbf{f}(\mathbf{a}) - \mathbf{f}^*) + \gamma_g \mathbf{a}^T \mathbf{G}^T \mathbf{W}_g^{-1} \mathbf{G} \mathbf{a} + \gamma_a (\mathbf{a} - \mathbf{a}^*)^T \mathbf{W}_a^{-1} (\mathbf{a} - \mathbf{a}^*), \quad (26)$$

where weighting matrices $\mathbf{W} \dots$ and Lagrange parameters $\gamma \dots$ are defined as follows:

$$\mathbf{W}_f = \frac{1}{\epsilon_f^2} \mathbf{C}_f, \quad \mathbf{W}_g = \frac{1}{\epsilon_g^2} \mathbf{C}_g, \quad \mathbf{W}_a = \frac{1}{\epsilon_a^2} \mathbf{C}_a, \quad (27)$$

$$\gamma_g = \frac{\epsilon_f^2}{\epsilon_g^2}, \quad \gamma_a = \frac{\epsilon_f^2}{\epsilon_a^2},$$

where ϵ_f^2 , ϵ_g^2 and ϵ_a^2 are the first diagonal elements of the corresponding covariance matrices \mathbf{C}_f , \mathbf{C}_g , \mathbf{C}_a , i.e., $\epsilon \dots = \{\mathbf{C} \dots\}_{11}$. We assume that all input data have lognormal error distribution [Dubovik and King, 2000; Dubovik, 2004]; that is, all measurements and parameters are used in logarithmic space. Specifically, the elements of the measurement vector \mathbf{f}^* include the logarithms of the nonnegative phase function and element P_{22} as follows: $\ln(P_{11}(\Theta_j, \lambda_j))$ and $\ln(P_{22}(\Theta_j, \lambda_j)/P_{11}(\Theta_j, \lambda_j))$. The measurements of the other four elements of the scattering matrix that may have negative values are included via simple transformation that allows adequate use of the logarithms for these elements: $\ln(1.1 - P_{ii}(\Theta_j, \lambda_j)/P_{11}(\Theta_j, \lambda_j))$. The retrieved vector \mathbf{a} in equations (25)–(27) is composed of the logarithms of $dV(r_k)/d \ln r$, n , k and $dn(\epsilon_p)/d \ln \epsilon$.

[27] Hence the developed inversion of the scattering matrix allows for the retrieval of all parameters of the spheroid mixture including accounting for different levels of accuracy in the measurements and in the a priori assumptions of aerosol parameters (such as refractive index and size distribution). For example, performing scattering matrix fitting, one has to account for the fact that $P_{11}(\Theta_j, \lambda_j)$ has very wide range of variability, while the rest of the elements presented as ratios $P_{ii}(\Theta_j, \lambda_j)/P_{11}(\Theta_j, \lambda_j)$ vary only between 1 and -1 . Therefore, for $P_{11}(\Theta_j, \lambda_j)$ measured at different angles we assumed the same relative accuracy ($\sim 3\text{--}5\%$). The ratios $P_{ii}(\Theta_j, \lambda_j)/P_{11}(\Theta_j, \lambda_j)$ we fitted to the same absolute accuracy ($\sim 0.005\text{--}0.01$) over different angles. The a priori constraints on retrieved characteristics $dV(r_k)/d \ln r$, n , k and $dn(\epsilon_p)/d \ln \epsilon$ also can be chosen flexibly by changing the values of the Lagrange parameters and weighting matrices (equations (25)–(27)).

3.2. Algorithm Testing

[28] A number of numerical tests have been conducted for evaluating the performance of the algorithm by inverting a simulated scattering matrix. The tests have shown that all aerosol parameters $dV(r_k)/d \ln r$, n , k and $dn(\epsilon_p)/d \ln \epsilon$ can be retrieved with no assumptions on their values (i.e., $\gamma_a = 0$ in equation (26)) and with the use of only minor smoothness constraints. Such conclusion is valid under two basic hypotheses: that particles are spheroids and that $P_{ii}(\Theta_j, \lambda_j)$ are measured with high accuracy (e.g., $< 3\text{--}5\%$ for $P_{11}(\Theta_j, \lambda_j)$ and $< 0.005\text{--}0.01$ for $P_{ii}(\Theta_j, \lambda_j)/P_{11}(\Theta_j, \lambda_j)$).

[29] In order to evaluate the performance of the retrieval algorithm, it was used to invert scattering matrices of water droplets measured by Volten et al. [2001]. The results of simultaneous inversion of $P_{ii}(\Theta_j, \lambda_j)$ measured at two wavelengths ($0.441 \mu\text{m}$ and $0.633 \mu\text{m}$) are shown in Figure 6. It can be seen that a good fit for all $P_{ii}(\Theta_j, \lambda_j)$ elements was achieved at both wavelengths (mean-root-square deviation is $\sim 2.5\%$). The retrieved size distribution shown (shape of

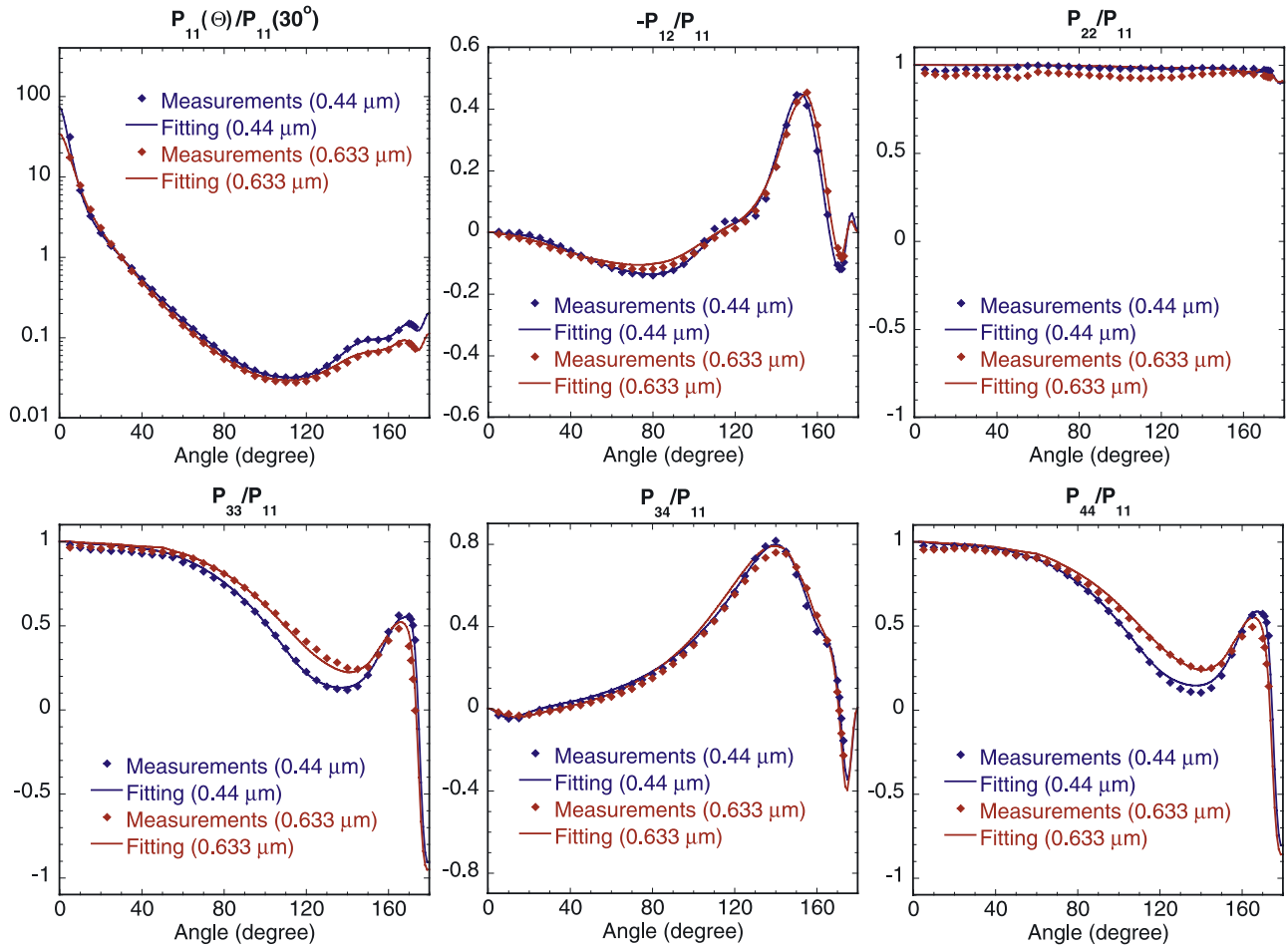


Figure 6. Results of fitting a water droplet scattering matrix by a mixture of spheroids.

size distribution was not restricted in the retrieval) in Figure 7a is in agreement with modeling results of *Volten et al.* [2001]. The retrieved axis ratio distribution $dn(\epsilon_p)/d\ln\epsilon$ (Figure 7b) shows a narrow peak for $\epsilon_p = 1.0$, thus in agreement with the known spherical shape of water droplets. The retrieved real part of the refractive index was ~ 1.34 – 1.33 , the imaginary part was ~ 0.0006 – 0.0005 (note that 1.33 and 0.0005 are at the limits of the parameter range of equation (23) for the kernel look-up table used and also that the actual refractive index of water is 1.33 and that the water droplets are nonabsorbing). Thus the results of inverting the scattering matrices of water droplets show high consistency between the measurements at both wavelengths and the modeling of scattering by spherical particles.

3.3. Inversion of Scattering Matrices of Irregular Particles

[30] The inversion algorithm has also been applied to analyze the measured scattering matrices of irregular particles [*Volten et al.*, 2001]. Here we discuss the results of fitting measured scattering matrix of Feldspar. This sample was chosen because Feldspar is commonly observed in desert dust aerosol composition [*Reid et al.*, 2003b] and the size distribution of this sample is the closest (among other samples analyzed by of *Volten et al.* [2001]) to the size distribution expected for airborne desert dust [e.g., *Reid et*

al., 1994, 2003a, 2003b; *Haywood et al.*, 2003]. The inversion of measurements for other samples was discussed in a separate study [*Veihelmann*, 2005]. Here we have attempted to fit the measured $P_{ii}(\Theta_j, \lambda_j)$ under different scenarios: (1) fixing $dV(r_k)/d\ln r$, n , and k (setting high γ_a and corresponding elements in \mathbf{W}_a for these parameters) and leaving $dn(\epsilon_p)/d\ln\epsilon$ free; (2) fixing n , and k (setting high γ_a and corresponding elements in \mathbf{W}_a for these parameters) and leaving $dV(r_k)/d\ln r$ and $dn(\epsilon_p)/d\ln\epsilon$ free; and (3) leaving all parameters n , k , $dV(r_k)/d\ln r$ and $dn(\epsilon_p)/d\ln\epsilon$ free.

[31] In all of the above scenarios minor smoothness constraints have been used to avoid unrealistic oscillations in $dV(r_k)/d\ln r$, $dn(\epsilon_p)/d\ln\epsilon$ and $n(\lambda)$ and $k(\lambda)$ (if scattering matrices were fitted at several wavelengths). Applying the algorithm to the measured $P_{ii}(\Theta_j, \lambda_j)$ showed the following tendencies:

[32] 1. For each single wavelength the Feldspar scattering matrices can be adequately reproduced by spheroids if $dV(r_k)/d\ln r$ is not fixed. However, the retrieval of $dV(r_k)/d\ln r$ appears rather unstable (using different initial guesses leads to noticeable differences in the retrieved size distributions). Fixing the size distribution to the one provided for each sample in a database described by *Volten et al.* [2005] constrained the accuracy of the matrix fitting.

[33] 2. Fixing n , k at values provided by *Volten et al.* [2005] did not substantially influence the accuracy of the

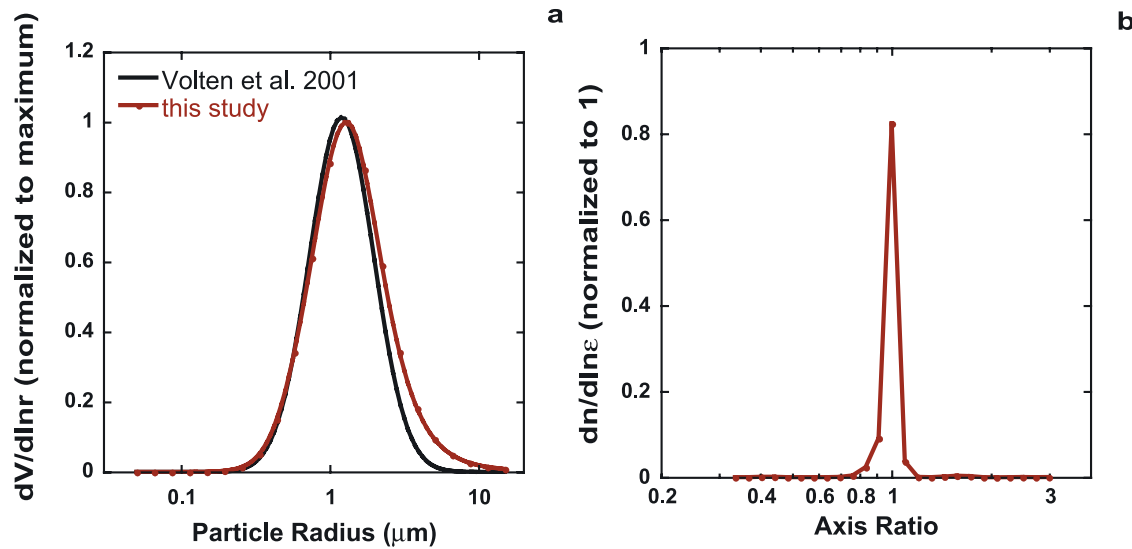


Figure 7. (a) Size distribution (used by *Volten et al.* [2001], black line; retrieved in this study, red line). (b) Axis ratio distribution retrieved from an inversion of water droplet scattering matrix (measured at two wavelengths 0.441 and 0.633 μm).

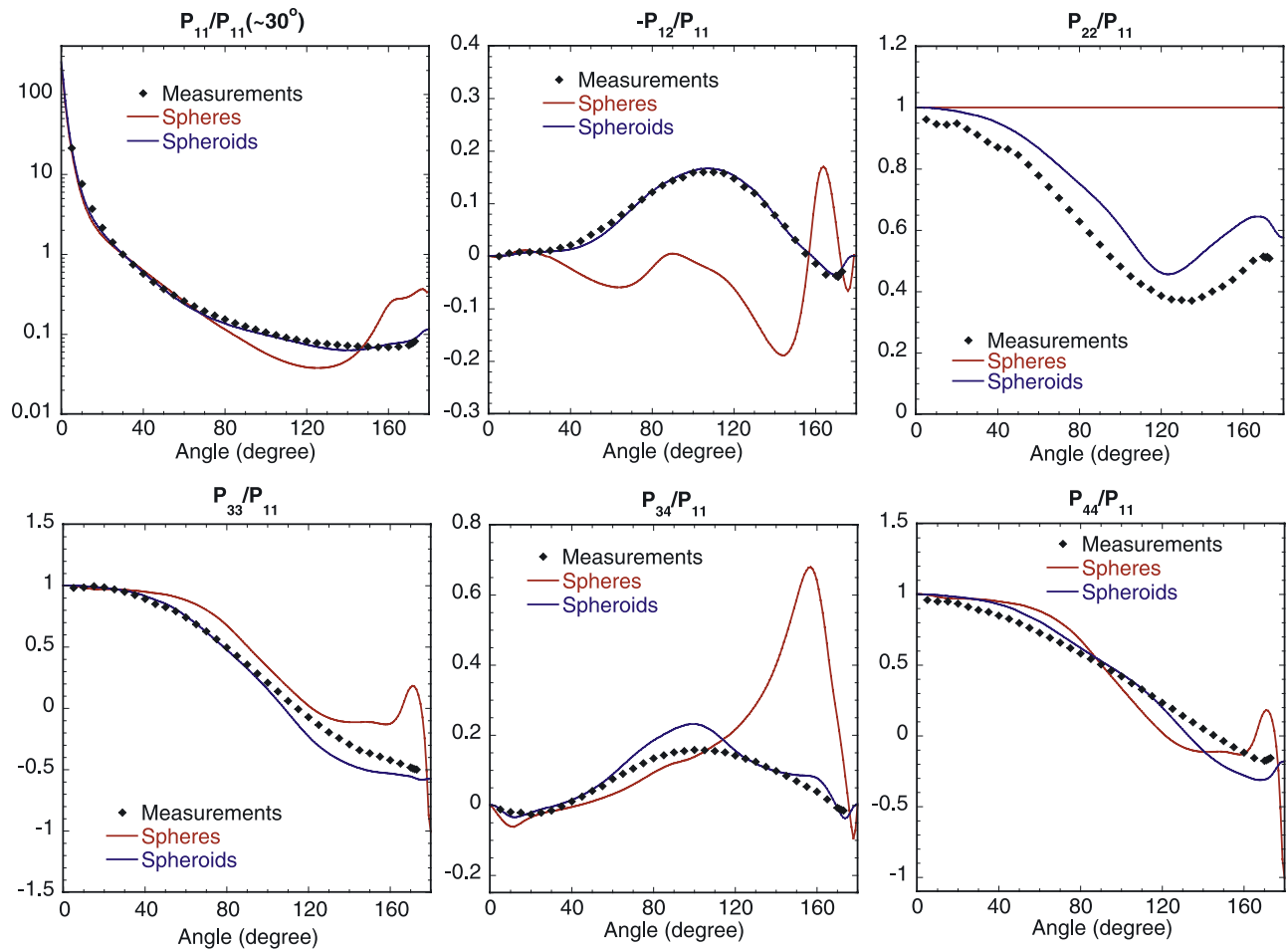


Figure 8. Results of fitting a Feldspar scattering matrix measured at 0.441 μm . The blue line shows the simulation based on the assumption of spheroidal particle shape. The red line shows scattering matrices simulated for spherical particles using the size distribution and complex refractive index retrieved using the spheroid model.

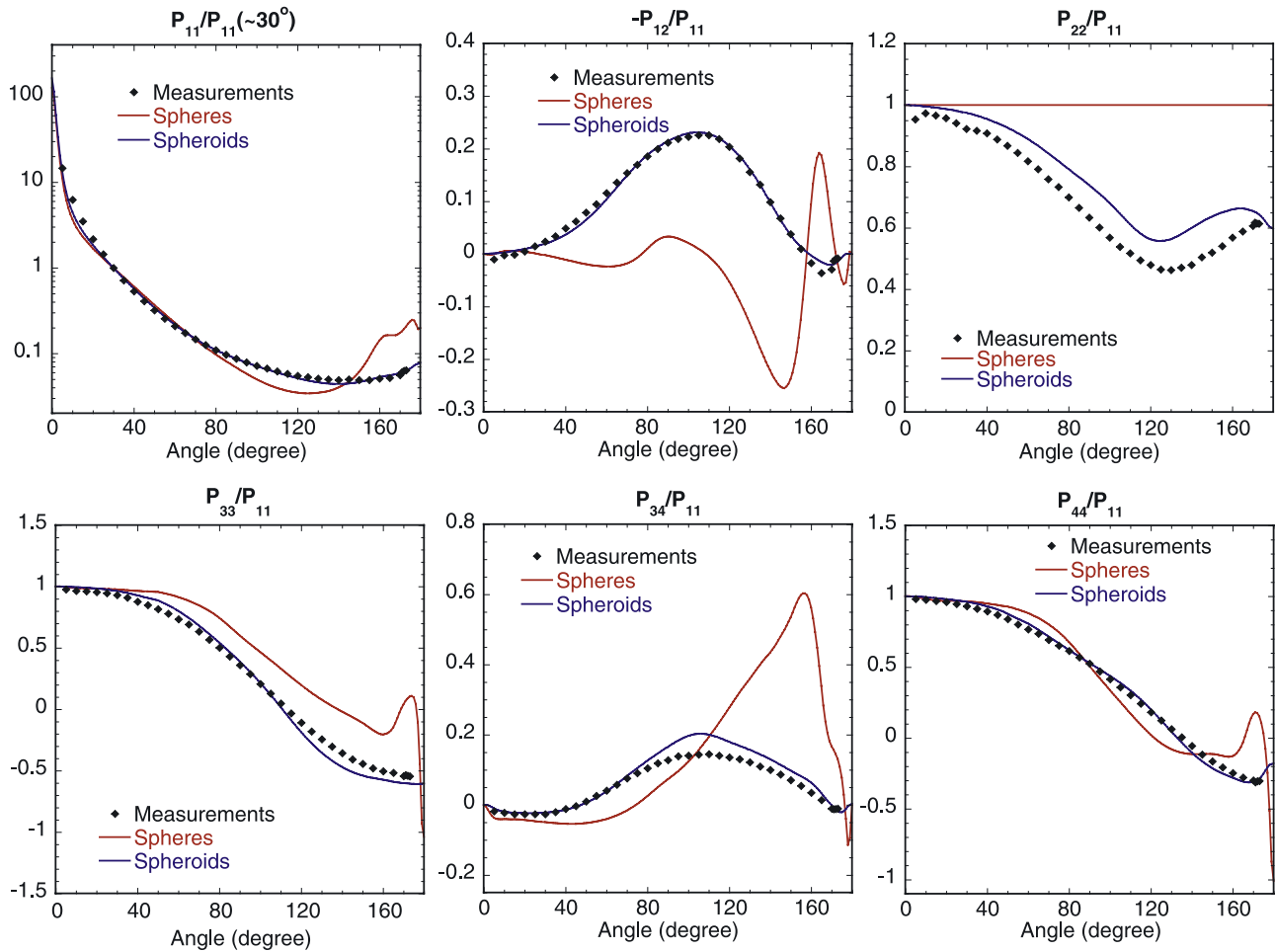


Figure 9. Results of fitting the Feldspar scattering matrix measured at $0.633 \mu\text{m}$. The blue line shows the simulation based on the assumption of spheroidal particle shape. The red line shows scattering matrices simulated for spherical particles using the size distribution and complex refractive index retrieved using the spheroid model.

matrix fitting. However, leaving n , k as invertable free parameters resulted in the fact that the retrieved n , k were reasonably close to the values suggested by *Volten et al.* [2005]. However, if the size distribution was fixed according to the one provided in the database of *Volten et al.* [2005], the good fit was achieved only at the cost of unrealistically high values of k .

[34] 3. The retrieval of $dn(\varepsilon_p)/d\ln\varepsilon$ was critical for achieving a good fit of the scattering matrices. For example, fixing $dn(\varepsilon_p)/d\ln\varepsilon$ from a spheroid mixture function to a mixture of polydisperse spheres did not allow any reasonable fit to the measured $P_{ii}(\Theta_j, \lambda_j)$ even if $dV(r_k)/d\ln r$, n , and k were left free in the inversion.

[35] Figures 8 and 9 show the results of fitting $P_{ii}(\Theta_j, \lambda_j)$ measured for the Feldspar sample at two wavelengths $0.441 \mu\text{m}$ and $0.633 \mu\text{m}$ with no fixed parameters used in the fitting process. Overall the agreement between the modeled and measured scattering matrices is better than in other studies analyzing the same scattering matrix [Noussainen and Vermeulen, 2003; Kahnert, 2004; Veihelmann et al., 2004; Noussainen et al., 2006]. Nonetheless, one can see that the measurement results for $P_{11}(\Theta_j, \lambda_j)$ and $-P_{12}(\Theta_j, \lambda_j)/P_{11}(\Theta_j, \lambda_j)$ are fitted noticeably better than

the other element ratios. This is because the weighting matrices \mathbf{W}_f that were set in the inversion assumed much higher fitting accuracy for the first two elements compared with the other four. This weighting was selected because we could not achieve equally good fits for all six elements of the matrix and since accurate knowledge of $P_{11}(\Theta_j, \lambda_j)$ and $-P_{12}(\Theta_j, \lambda_j)/P_{11}(\Theta_j, \lambda_j)$ is most important for polarimetric passive remote sensing of the atmosphere. Indeed, since the incident solar radiation is unpolarized, the spectral and angular dependencies of the diffuse radiation are dominated by $P_{11}(\Theta_j, \lambda_j)$ and $P_{12}(\Theta_j, \lambda_j)$ (this can be seen from the derivations by Hovenier and van der Mee [1983]).

[36] The fitting results shown in Figures 8 and 9 were achieved by inverting measurements at a single wavelength. Simultaneous inversions of scattering matrices measured at two wavelengths ($0.441 \mu\text{m}$ and $0.633 \mu\text{m}$) were not successful in that a reasonably good fit was not achieved. The root-mean-square (over all elements) fit for a single wavelength was about 7–10%, while for two wavelengths the root-mean-square fit did not drop below 20%. An analysis of the reasons limiting the agreement of the two-wavelength fit has shown that the spheroid model could not reproduce the measured spectral dependence of the ratio $P_{11}(\Theta_j, \lambda_j)/$

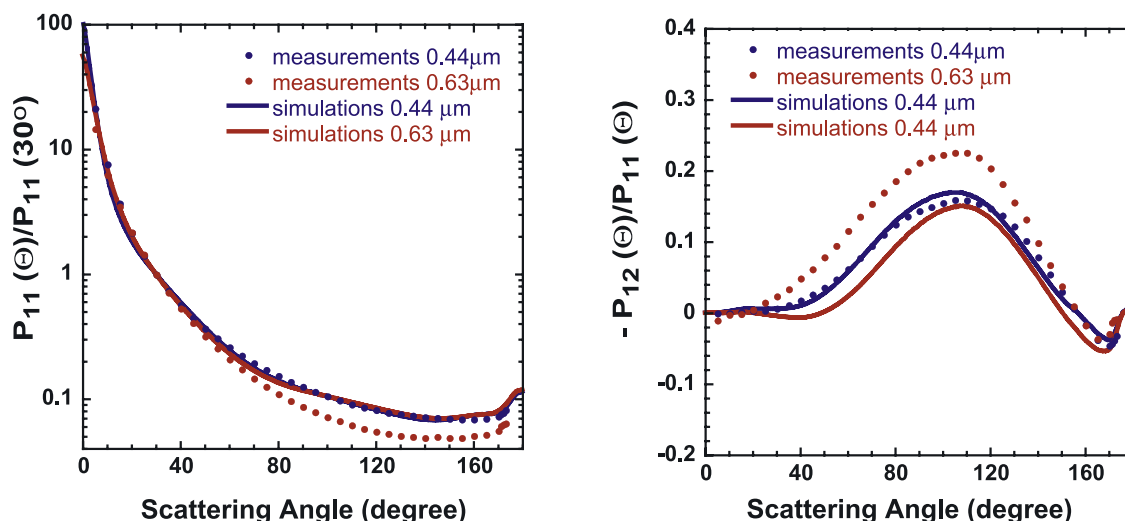


Figure 10. Measured and simulated phase functions (normalized to a value at $\Theta = 30^\circ$) and degree of linear polarization using aerosol parameters retrieved from measurements at $\lambda = 0.441 \mu\text{m}$.

$P_{11}(30^\circ, \lambda_j)$. It can be seen from Figure 10 that the simulations with spheroids do not allow such strong wavelength dependence as shown in the measurements. The main difference is caused by strong wavelength dependence of the ratio $P_{11}(\Theta_j, \lambda_j)/P_{11}(30^\circ, \lambda_j)$ that results in the strong wavelength dependence of the ratios $-P_{12}(\Theta_j, \lambda_j)/P_{11}(\Theta_j, \lambda_j)$. As demonstrated by Figure 10 the simulations suggest much less spectral dependence of $P_{11}(\Theta_j, \lambda_j)/P_{11}(30^\circ, \lambda_j)$.

[37] In principle, the limitations of the spheroid model can be a possible cause of this discrepancy, since the spheroid model does not include the potential effects of small-scale structures on the surface or inside the irregular particles. However, those irregularities are more likely to affect the angular distribution of light scattering rather than its spectral properties [Han et al., 1999; Chamaillard and Lafon, 2001; Mishchenko et al., 2002; C. Li et al., 2004; Sun et al., 2004; Shcherbakov et al., 2006]. Also, it should be noted that the laboratory measurements for the Feldspar sample show a pronounced wavelength dependence, whereas that is not the case for all other samples of irregular particles for which measurements are available. For example the measurements for red clay or quartz particles [Volten et al., 2001, 2005] and green clay [Muñoz et al., 2001; Volten et al., 2005] at two wavelengths hardly show any spectral dependence. The measurements for those samples are more in line with the overall results obtained from inversions of AERONET atmospheric radiation measurements [Dubovik et al., 2002a, 2002b] which suggest no significant spectral dependence of the phase function of desert dust aerosols.

[38] Our present study shows that the measured spectral dependence can be reproduced by spheroids only if we assume differences for the size distributions of the Feldspar samples for each of the two wavelengths. If the size distributions were forced to be the same for observations at both wavelengths, we could not reproduce the spectral dependence even if differences in axis ratio distributions or an acceptable spectral dependence of the complex refractive index were allowed. The retrieved size distributions (Figure 11a) are generally similar to the size distribution

suggested by Volten et al. [2001] for the Feldspar sample. However, the retrieved $dV(r_k)/d\ln r$ show minor shifts in the modal radii and indicate the presence of small particles ($<1.0 \mu\text{m}$). The differences in $dV(r_k)/d\ln r$ retrieved from measurements at different wavelengths (0.441 and $0.633 \mu\text{m}$) could possibly be explained by random noise and other limitations of the measurements. For example, the error bars for the experimental $P_{11}(\Theta)$ at small scattering angles ($<10^\circ$), are usually larger than at other scattering angles [see Volten et al., 2001]. Unfortunately, this scattering angle range ($<10^\circ$) is the one most sensitive to the presence of particles with radii $1 \mu\text{m}$ and greater. This was one of the reasons for choosing the Feldspar sample for this analysis, since it has noticeably smaller particles than the red clay or quartz samples and is, therefore, closer to the known size range of airborne desert dust. Thus difficulties in reproducing the spectral dependence of the scattering matrices can potentially be caused by limitations of either the spheroid model or the measurement scheme or by both factors.

[39] The presence of a minor fraction of small particles ($r < 0.5 \mu\text{m}$) can be real. As noted by Min et al. [2005], the laser diffraction method [Konert and Vandenberghe, 1997] employed by Volten et al. [2001] for measuring the size of dust particles in the laboratory is not suited to detect the presence of submicrometer particles, which could be the reason why the fine particle component was not found. The analysis of Min et al. [2005] also has shown that some fine mode particles are needed in order to reproduce the measured polarization ($-P_{12}(\Theta)/P_{11}(\Theta)$) of the quartz sample by an ensemble of hollow spheres. However, both hollow spheres and spheroids are simplified approximations and there is a possibility that the small particles retrieved in the fits may actually mimic the effect of small-scale (surface) structures on irregular particles [see, e.g., Nousiainen et al., 2003]. Similarly, earlier studies [Dubovik et al., 2000, 2002a] showed that aerosol retrievals based on the assumption of spherical particles had a tendency to overestimate the concentration of fine particles (see section 4.1). Nonetheless a presence of fine particles in desert dust aerosol has been shown by in situ measurements [e.g., Reid et al., 1994,

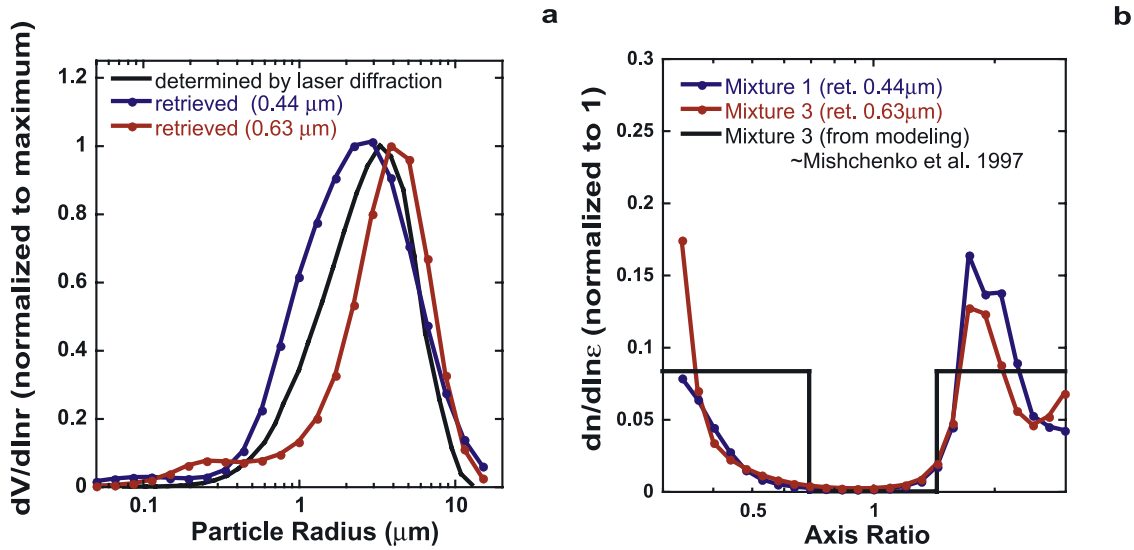


Figure 11. (a) Size distributions retrieved for Feldspar. (b) Axis ratio distributions retrieved for Feldspar and determined by modeling.

2003a, 2003b; Haywood *et al.*, 2003]. In addition, a noticeable presence of small particles in desert dust size distributions is in agreement with optical measurements that are not sensitive to particle shape. Namely aerosol retrievals using only scattering in the aureole [e.g., Dubovik *et al.*, 2002b] and even analysis of spectral optical thickness (i.e., without using any inversion) indicate the presence of fine particles in desert dust. For example, Holben *et al.* [2001] presented extended climatologies of optical thickness observations by the AERONET ground-based Sun/sky radiometers [Holben *et al.*, 1998], where spectral dependence of the aerosol optical thickness was approximated by the Ångström parameterization [Ångström, 1929]:

$$\ln(\tau(\lambda)) = -\alpha \ln(\lambda) + \beta \quad (28)$$

The exponent α is known as the Ångström exponent and it is often used as an indicator of aerosol size distribution. The linear fit of $\ln(\tau(\lambda))$ versus $\ln(\lambda)$ is only an approximation (the quadratic fit is more accurate). However, when computed over a sufficiently large wavelength interval including both the visible and near infrared (i.e., 0.44 and 0.87 μm) then the Ångström exponent is sensitive to the relative contributions of fine and coarse mode particles to the optical depth [Eck *et al.*, 1999; Reid *et al.*, 1999; O'Neill *et al.*, 2001; Schuster *et al.*, 2006]. Specifically, $\alpha \sim -0.2$ corresponds to pure coarse mode aerosol and $\alpha \sim 1.7$ – 2.7 corresponds to pure fine mode aerosol. Holben *et al.* [2001] indicate that the Ångström parameter is small but positive for the majority of observed desert dust outbreaks, while any aerosol composed from particles only with radius $>1.0 \mu\text{m}$ should have a negative Ångström parameter.

[40] The axis ratio distributions retrieved from measurements at 0.441 and 0.633 μm (Figure 11b) have a similarity in the fact that there are no “near spherical” particles with ϵ_p between ~ 0.7 ($=1/1.44$) and ~ 1.44 (unfortunately, independent measurements of shape distribution of Feldspar sample particles are not available). The wings of the axis ratio distributions shown on Figure 11b are quite different

for the two wavelengths. Kahnert [2004] also reported high variability of spheroid shape distributions from his effort to reproduce the desert dust scattering matrix modeled using a mixture of prisms. However, simulations show that those differences are not very significant for the modeling of scattering matrices. For example, Figure 12 illustrates the phase matrices simulated for desert dust aerosol using an ensemble of spheroids differing only by their axis ratio distributions. We used $dn(\epsilon_p)/d\ln \epsilon$ retrieved from the Feldspar measurements at 0.441 and 0.633 μm . In addition, we used the spheroid mixture with $dn(\epsilon_p)/d\ln \epsilon$ formed simply by the following straight lines:

$$\frac{dn(\epsilon)}{d\ln \epsilon} = \begin{cases} 0 & -0.7 < \epsilon < 1.44 \\ \text{const} - \epsilon \leq 0.7 \text{ and } 1.4 \leq \epsilon \end{cases} \quad (29)$$

This distribution is analogous (very close) to the one suggested by Mishchenko *et al.* [1997] (see Figure 11b). Specifically, Mishchenko *et al.* [1997] concluded that the measured phase function of mineral dust [Jaggard *et al.*, 1981] can be reproduced by scattering from a mixture of spheroids with equal numbers of particles with aspect ratios ranging from $\alpha_{\min} = 1.4$ (or 1.2) to $\alpha_{\max} = 2.4$.

[41] Thus one can see from Figure 12 that $P_{11}(\Theta, \lambda)$ and $-P_{12}(\Theta, \lambda)/P_{11}(\Theta, \lambda)$ are nearly equivalent for all spheroid mixtures. Some differences can be seen for other elements (especially for $P_{22}(\Theta, \lambda)/P_{11}(\Theta, \lambda)$), however they are likely to be insignificant for passive remote sensing applications. Similar conclusions regarding the relative lack of importance of axis ratio distribution details were stated in studies of Mishchenko *et al.* [1997], Nousiainen and Vermeulen [2003]. Nousiainen *et al.* [2006] in their studies introduced shape parameterization (the weights depend on the axis ratio as a power law) driven by one parameter only. Also, Kahnert [2004] reported that a rather wide diversity of spheroid shape distributions reproduced the same desert dust scattering matrix modeled by a mixture of prisms. Therefore we have adopted the additional assumption of an

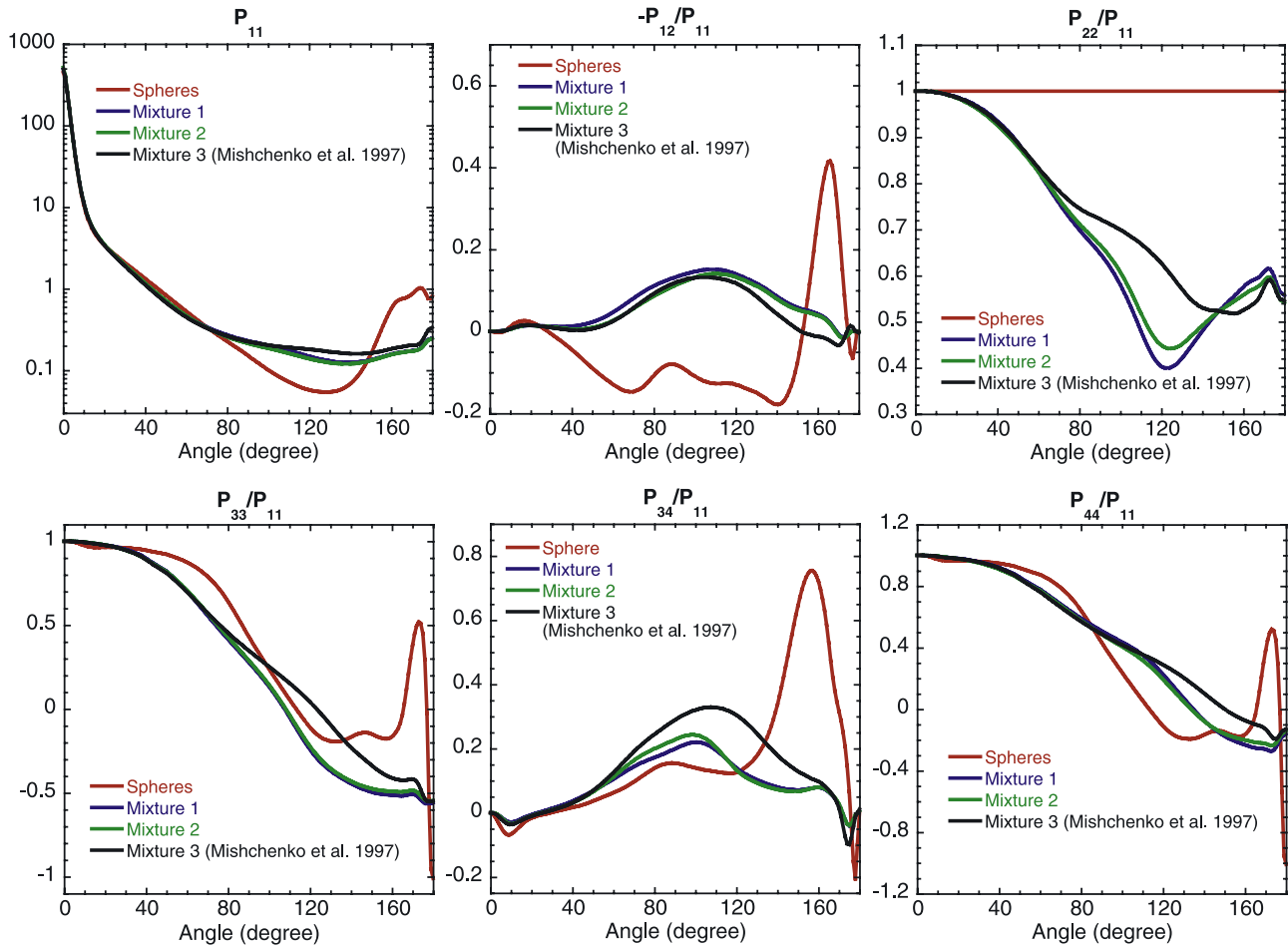


Figure 12. Phase matrices simulated at $0.441 \mu\text{m}$ for desert dust. Size distribution and complex refractive index were assumed according to the climatology of *Dubovik et al. [2002a]* for Saudi Arabia observations. The simulations were performed for different axis ratio distributions (mixture 1, mixture 2 and mixture 3 as shown in Figure 11b).

equal presence of prolate and oblate spheroids with the same aspect ratios. Accordingly, in the retrieval algorithm, the aerosol shape distribution is represented by an aspect ratio distribution $dn(\varepsilon_p)/d\ln\varepsilon'$ and therefore the number of retrieved parameters (discrete points N_p describing the shape distribution) is significantly decreased, i.e.,

$$dn(\varepsilon_p)/d\ln\varepsilon \Rightarrow dn(\varepsilon'_p)/d\ln\varepsilon',$$

and

$$(0.3 \leq \varepsilon_p \leq 3.0, \quad N_p = 25) \Rightarrow (1.0 \leq \varepsilon'_p \leq 3.0, \quad N_p = 13). \quad (30)$$

[42] Numerical tests and inversion of the measurements have shown that using the assumption of an equal presence of prolate and oblate spheroids has resulted in improved stability of the retrievals. For example, the aspect ratio distributions and size distributions derived by inversion of the scattering matrix of Feldspar measured at 0.441 and $0.633 \mu\text{m}$ are shown in Figure 13. For improving the stability of the results shown in Figure 13, we have additionally excluded spheroids with $\varepsilon'_p \leq 1.44$ from the

retrievals, since all retrievals showed no significant presence of such particles. Comparing Figures 11 and 13 one can see that the retrieval results obtained from Feldspar measurements at two different wavelengths (0.441 and $0.633 \mu\text{m}$) are in better agreement in Figure 13 than in Figure 11 because of the added assumption of equal number of prolate and oblate spheroids. Also the retrieved characteristics in Figure 13 are smoother. In addition, the inversions illustrated by Figure 13 are much less sensitive to the initial guess of the size distribution than those of Figure 11. However, fixing the number of prolate and oblate spheroids also resulted in a slight decrease of the fitting accuracy of the measured scattering matrices.

4. Applications to Desert Dust Retrievals From AERONET Remote Sensing Observations

4.1. Improving the Spheroid Model in Operational AERONET Retrievals

[43] The previous studies [*Dubovik et al., 2002b*] introduced the spheroid-based parameterization of light scattering into the AERONET operational inversion algorithm described by *Dubovik and King [2000]*. The algorithm retrieves the aerosol size distribution and complex refractive

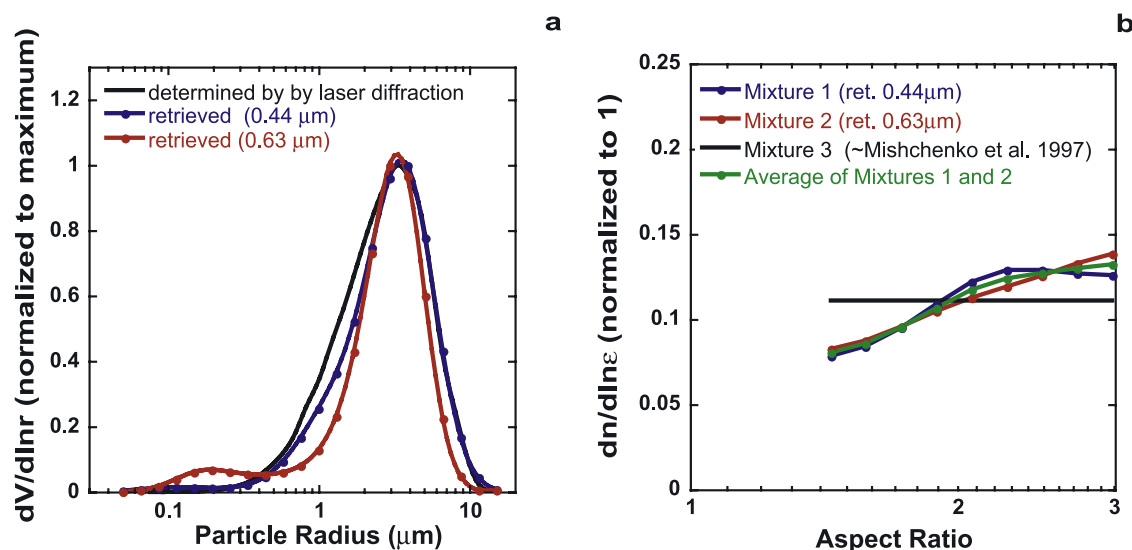


Figure 13. (a) Size distributions retrieved for Feldspar with the added assumption of equal number of prolate and oblate spheroids (see Figure 11 for comparison). (b) Aspect ratio distributions retrieved for Feldspar and determined by modeling.

index from the angular and spectral intensity distribution of atmospheric radiation as measured from the ground. Spheroid scattering is modeled in the algorithm of *Dubovik et al.* [2002b] by using a subset of kernel look-up tables produced for a single fixed axis ratio distribution. The algorithm was applied to the entire database of AERONET almucantar scan (the results are available at the AERONET web site: <http://aeronet.gsfc.nasa.gov>). This spheroid model significantly improved the performance of aerosol retrievals for desert dust observations. Figure 14 shows a typical example where utilizing the spheroid scattering assumption resulted in the removal of the false fine mode in $dV(r_k)/d\ln r$ and the removal of the false spectral dependence in the real part of the refractive index.

[44] Also, using the spheroid model resulted in a decrease of the residual of fitting AERONET observations compared to the residual achieved by using Mie scattering. The decrease of the residual has been observed for nearly all observations of desert cases. The only situation where an increase of the residual by using the spheroid model instead of spheres systematically occurred was in locations where maritime aerosol dominated [*Smirnov et al.*, 2003]. Maritime aerosol is the only aerosol type that typically contains primarily spherical coarse mode particles, because of hygroscopic growth of sea salt particles. Detailed discussion of the spheroid model performance in retrieval of Asian aerosols can be found in the studies of *Eck et al.* [2005]. The present study continues the developments of the spheroid modeling approach introduced by *Dubovik et al.* [2002b]. Specifically, the look-up tables of spheroid kernels were updated by new ones computed with higher accuracy, for higher angular resolution and for a wider size parameter range (see description in section 2). Also, the new kernels were developed for all elements of the scattering matrix; that is, the spheroid model can now be utilized in polarimetric retrievals. In addition we reexamined the selection of the spheroid shape distribution. The axis ratio distribution fixed by *Dubovik et al.* [2002b] in the retrieval systemati-

cally produced undesirable and unrealistic features in the resulting phase functions, while the actual measurements show smoother phase functions [e.g., see *West et al.*, 1997; *Volten et al.*, 2001; *Muñoz et al.*, 2001]. Figure 15 illustrates that using $dn(\epsilon'_p)/d\ln \epsilon'$ retrieved from Feldspar scattering matrix improves the modeled phase function.

[45] Another shortcoming of the *Dubovik et al.* [2002b] retrievals was the fact that unrealistically high concentrations of very small particles and a strong spectral dependence in refractive index (the artifacts shown in Figure 16 for retrieval with the spherical model) remained in some desert dust retrievals even if the spheroid scattering model was used. (It should be noted that the retrievals with artifact of “large tails” have been automatically filtered from the original quality assured “Level 2.0” retrievals provided on AERONET website). An analysis of such cases has shown that the appearance of those artifacts is, at least partially, caused by very low sensitivity of observations to concentrations of very small particles with radii of $\sim 0.1 \mu\text{m}$ and smaller. Indeed, atmospheric radiances resulting from scattering by desert dust aerosol (i.e., aerosol dominated by coarse mode particles) are almost insensitive to an increase in concentration of very small particles ($r < 0.1 \mu\text{m}$) accompanied by a decrease of the real part of the refraction index. Therefore any minor experimental or model inconsistency may cause the appearance of an artificial fine mode in the size distribution and an artificial spectral dependence of the real part of the refraction index. For example, Figure 16 shows that using size distributions and refractive indices that produce artifacts has only a small effect on the fit of measured to modeled atmospheric radiances in solar almucantar. One can also see that if the spherical model is used the appearance of these artifacts helps to compensate for the differences due to particle nonsphericity. Therefore we introduced an additional a priori assumption into the AERONET retrievals: (1) high concentrations of particles with radius $0.05 \mu\text{m}$ are suppressed (by including a very low value of $dV(r_i)/d\ln r$ as an a priori estimate for radius $r_i =$

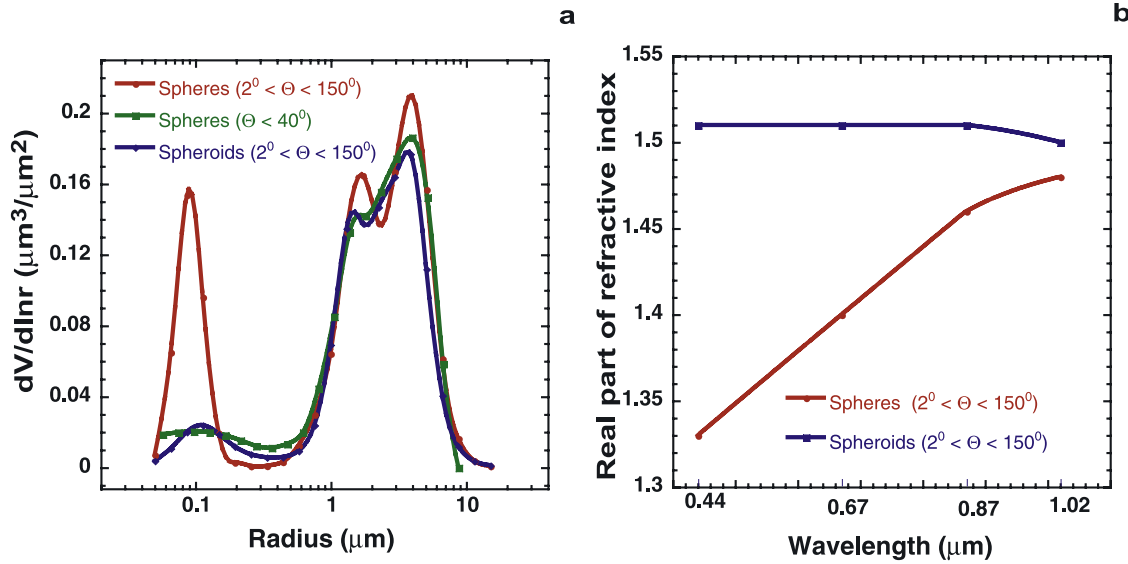


Figure 14. A typical situation where utilizing the spheroid scattering assumption [Dubovik *et al.*, 2002b] resulted in the removal of the false fine mode in the size distribution and false spectral dependence in the real part of refractive index. Size distributions and refractive indices are retrieved assuming sphere and spheroid models from spectral radiance measurements covering the full range of scattering angles. The size distribution retrieved from the aureole only ($\Theta < 40^\circ$, where effects of nonsphericity are minimal) and assuming spherical particles is also shown.

0.05 μm in the retrieval scheme of Dubovik and King [2000] and (2) the spectrally smooth real part of the refractive index was enforced (i.e., γ_4 was increased in scheme of Dubovik and King [2000]). Figure 16 illustrates the situation where both retrievals using spheres and spheroids produced some artifacts that were removed using the new additional constraint in the retrieval. It is important to note that the applying new constraint for the inversion with spherical model resulted in a noticeable increase of the fitting residual ϵ_{sky} . The symbol ϵ_{sky} denotes root-mean-square of fitting modeled to measured sky radiances at all wavelengths and angles. In contrast, for spheroid retrieval ϵ_{sky} remains practically unchanged when the new constraint was added.

4.2. Desert Dust Retrievals From AERONET Polarimetric Measurements

[46] Accounting for polarization was another addition to the development [Dubovik and King, 2000; Dubovik *et al.*, 2002b] of retrieving detailed aerosol properties from measurements of ground-based radiometers. Indeed, some Cimel Sun-sky radiometers (utilized by AERONET network) make polarimetric measurements of atmospheric radiation [Holben *et al.*, 1998] at 0.87 μm . Studies by Vermeulen *et al.* [2000] and Z. Q. Li *et al.* [2004] discuss the use of these polarimetric measurements for aerosol retrievals based on a spherical aerosol model. However, retrieving desert dust microphysics (size distribution and complex refractive index) from polarimetric observations is questionable without a proper accounting of the effects of particle shape. In this regard, as was shown in section 2, the kernel look-up tables of spheroids described in section 1 are a useful tool for performing nonspherical aerosol retrievals from polarimetric laboratory measurements. The same concept was implemented for inverting polarimetric observa-

tions of atmospheric radiation. Figure 17 shows the chart summarizing the concept of including a spheroid model in the inversion of Sun/sky radiometer polarimetric measurements. Similar to the algorithm described in section 2, the aerosol single scattering properties ($\tau_{\text{ext}}(\lambda)$, $\tau_{\text{scat}}(\lambda)$ and

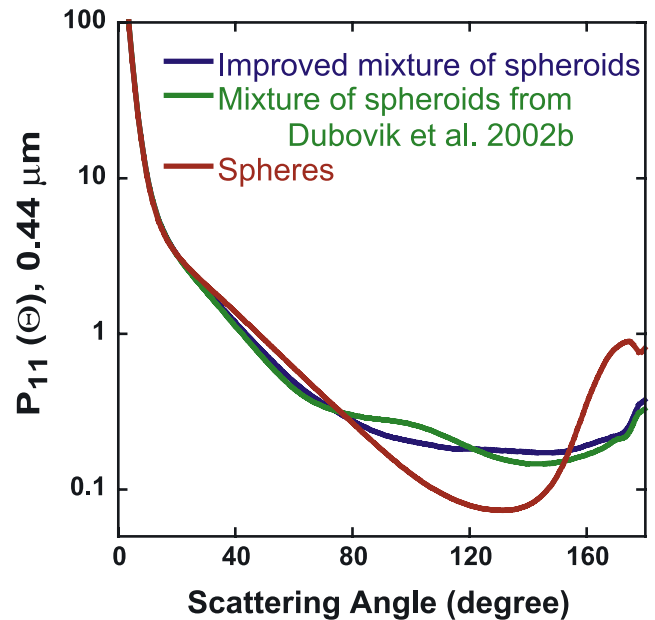


Figure 15. Typical phase function retrievals from AERONET Sun/sky radiometers observation using a spherical aerosol model and also two spheroid mixture models: the Dubovik *et al.* [2002b] mixture and the improved mixture (an average retrieved from Feldspar scattering matrices measured at 0.441 and 0.633 μm , as shown in Figure 13b).

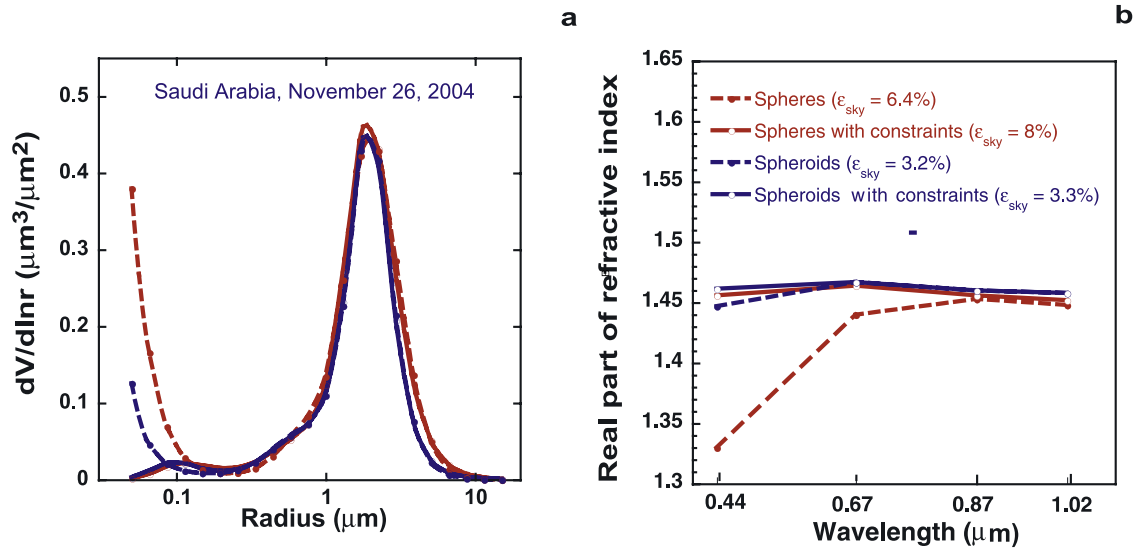


Figure 16. Illustration of removing the artifacts in retrieved size distributions and real refractive index by enforcing low a priori concentrations of particles with a radius of 0.05 μm .

$P_{ii}(\Theta_j, \lambda_j)$) are modeled using look-up tables of spheroid kernels. The multiple scattering effects required for modeling the angular distribution of atmospheric radiances and polarization are accounted for using the successive orders of scattering radiative transfer code developed by *Deuzé et al.* [1989]. The numerical inversion is adopted from *Dubovik and King* [2000], where a multiterm Least Squares Method concept [Dubovik, 2004] has been employed. This retrieval code simultaneously fits three different types of atmospheric measurements: spectral optical thickness $\tau(\lambda)$, spectral and

angular distribution of atmospheric radiances $I(\lambda; \theta_0; \theta; \phi)$ and their degree of linear polarization $P(\lambda; \theta_0; \theta; \phi)$ that is defined as follows [Bohren and Huffman, 1983]:

$$P(\lambda; \theta_0; \theta; \phi) = q \frac{\sqrt{(Q(\lambda; \theta_0; \theta; \phi))^2 + (U(\lambda; \theta_0; \theta; \phi))^2}}{I(\lambda; \theta_0; \theta; \phi)}, \quad (31)$$

where θ_0 is solar zenith angle, θ is observation zenith angle, ϕ is observation azimuth angle. The multiplier q determines

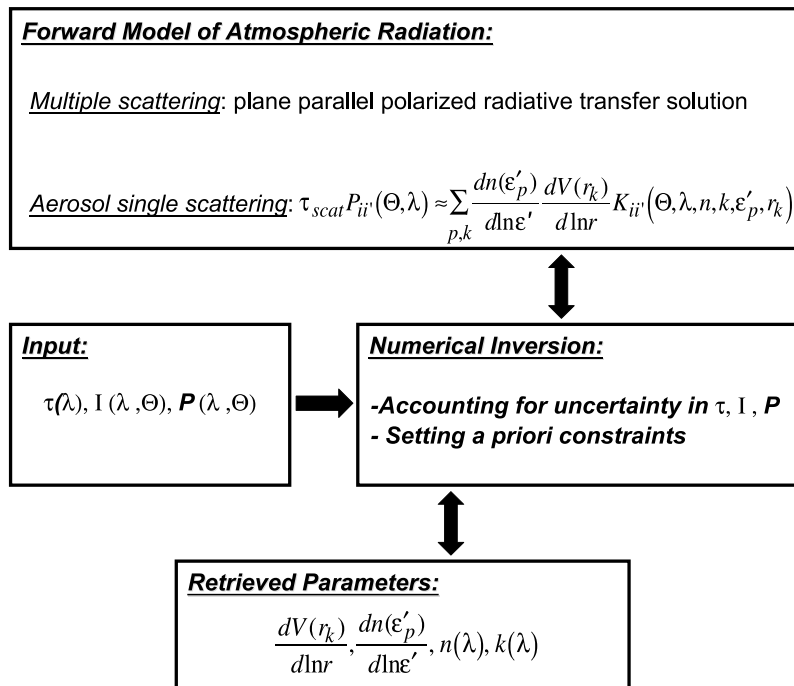


Figure 17. Illustration of inversion logistics in the algorithm developed for inversion of both radiometric and polarimetric measurements of AERONET Sun/sky radiometers.

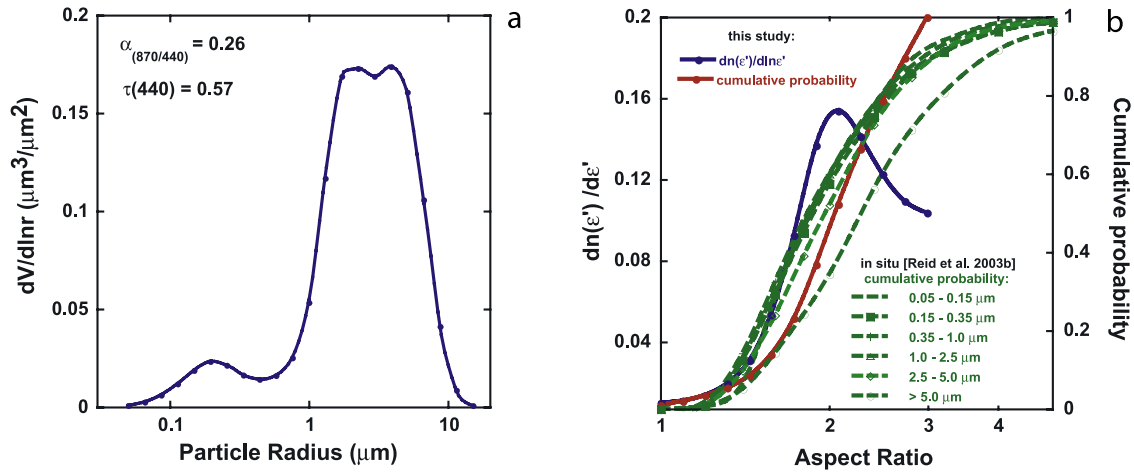


Figure 18. Results of an aerosol retrieval (using the spheroid particle shape model) by simultaneous inversion of $\tau(\lambda)$, $I(\lambda; \Theta)$ and $P(\lambda; \Theta)$ observed at five wavelengths (0.44, 0.5, 0.67, 0.87, and 1.02 μm) at the MAARCO site (UAE²) on 8 August 2004. (a) Retrieved size distribution. The symbol $\alpha_{(870/440)}$ denotes the Ångström exponent calculated using τ at 440 and 870 nm. (b) Comparison of aspect ratio distributions retrieved in this study with those measured in situ by Reid *et al.* [2003b].

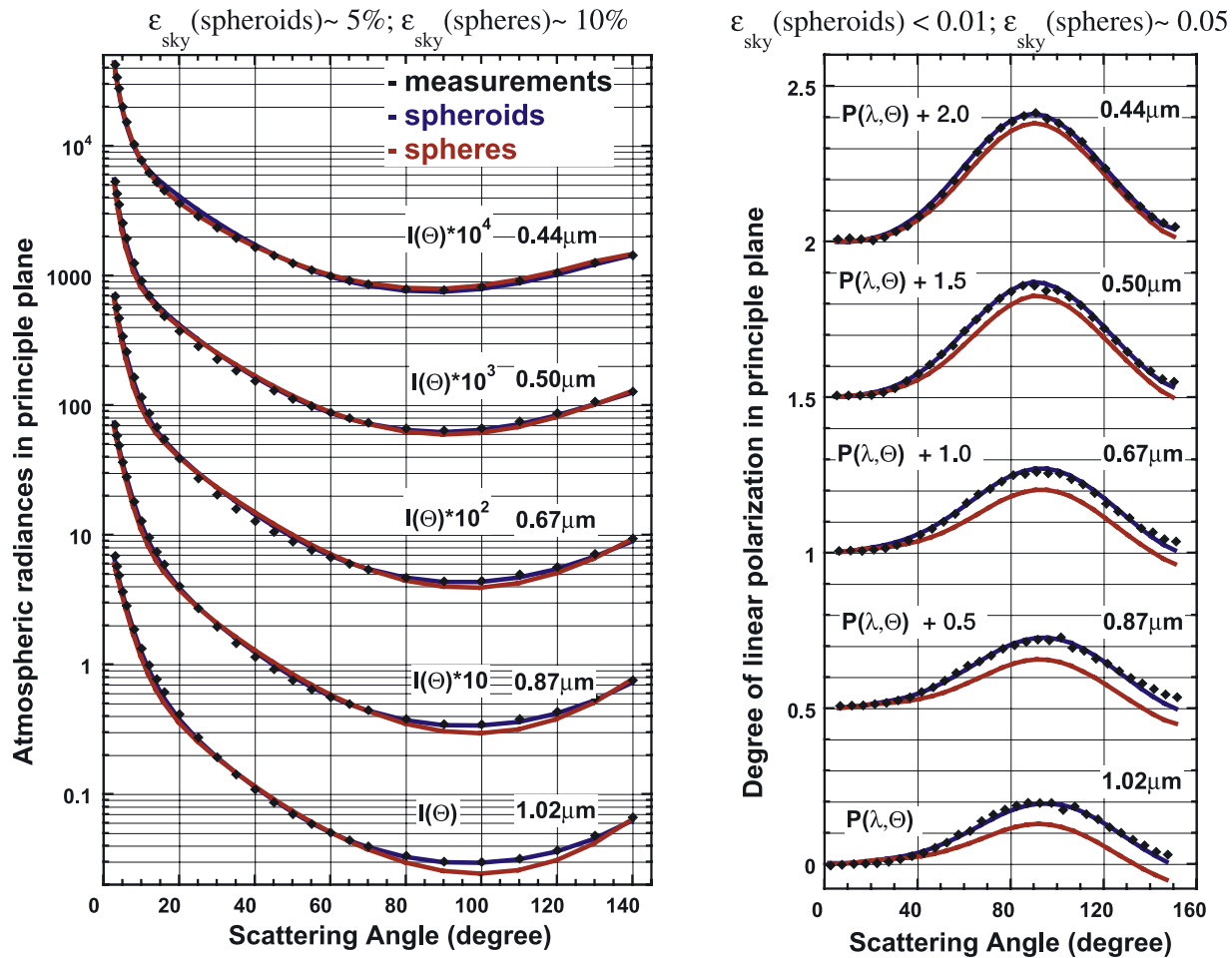


Figure 19. An illustration of (a) atmospheric radiances and (b) linear polarization fitting by simulations with a spheroid model (using retrieved complex refractive index, size and aspect ratio distributions given in Figure 18) and by simulations with a spherical aerosol model using the same size distribution and complex refractive index.

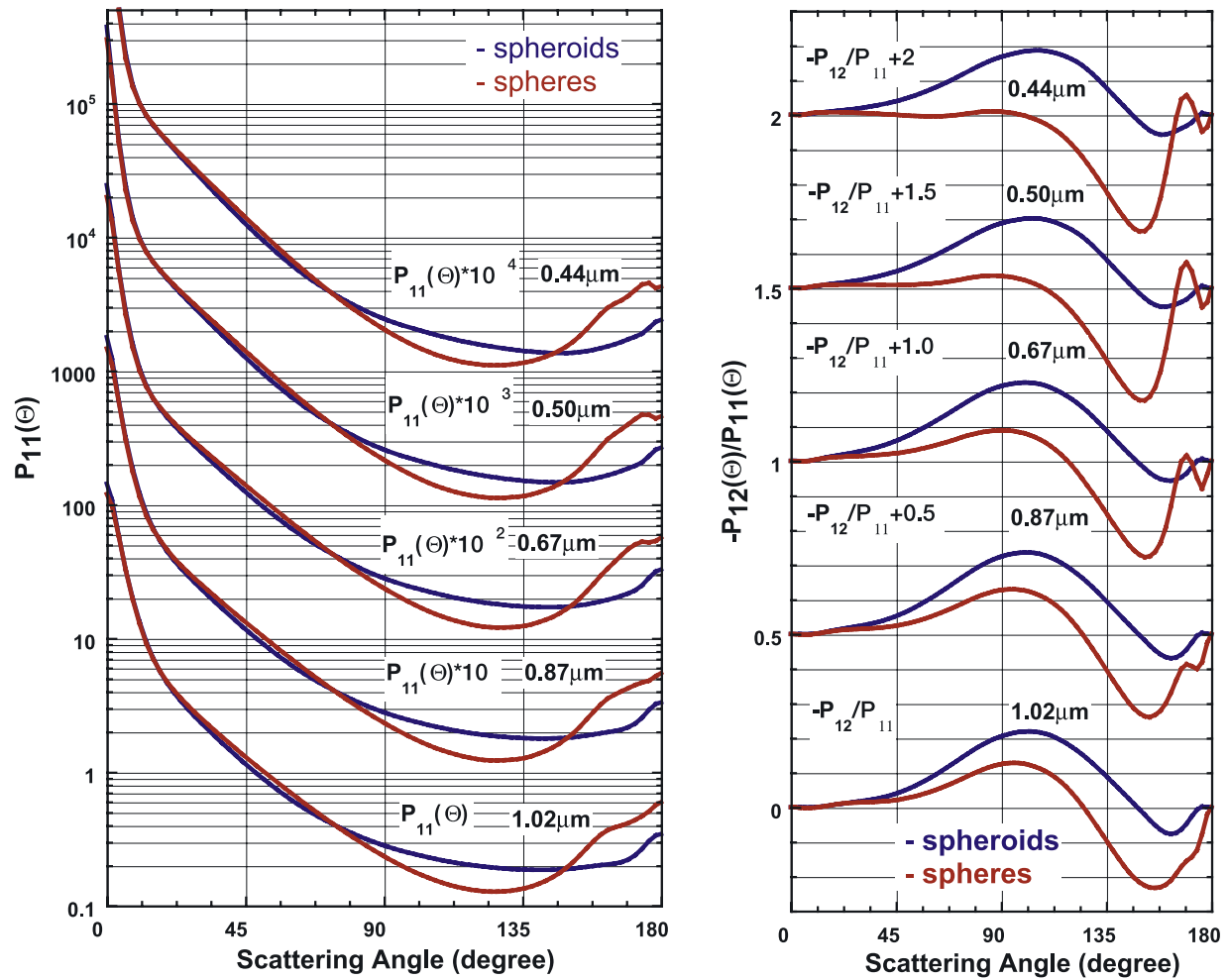


Figure 20. Desert dust phase function and degree of linear polarization simulated with spheroids (using retrieved complex refractive index, size and aspect ratio distributions given in Figure 18) and spherical aerosol model with the same size distribution and complex refractive index.

the sign of linear polarization: $q = -Q/|Q|$. This algorithm has been applied to AERONET observations. The retrieval algorithm was set to fit the data to the level of AERONET measurement accuracy, i.e., ~ 0.01 absolute accuracy for $\tau(\lambda)$ at air mass equal 2 [Eck et al., 1999]; $\sim 5\%$ accuracy for $I(\lambda; \Theta)$ [Holben et al., 1998]; and 0.01 absolute accuracy for $P(\lambda; \Theta)$. Here and below, the atmospheric radiances and their polarization are written using scattering angle Θ , i.e., as $I(\lambda; \Theta)$ and $P(\lambda; \Theta)$.

[47] The standard polarized Cimel Sun/sky radiometers [Holben et al., 1998] perform measurements of polarization in the solar principle plane at a single channel $0.87 \mu\text{m}$. However, here we used the data from the newest model of Cimel Sun/sky radiometer that measures polarization in the solar principle plane in many spectral channels. This instrument was deployed during the UAE² (United Arab Emirate United Aerosol Experiment, web site: <http://uae2.gsfc.nasa.gov/index.html>) field campaign [Reid et al., 2005] that took place during summer and fall of 2004 in UAE (United Arab Emirates), where several AERONET radiometers were placed in locations where desert dust is typically present. The results of a typical aerosol

retrieval during a desert dust event in the UAE are shown in Figures 18–20. The retrieved size distribution (Figure 18a) and the refractive index ($n = \sim 1.56$) coincide well with in situ measurements of Saharan dust aerosol [Reid et al., 2003a, 2003b]. The retrieved aspect ratio distribution $dn(\epsilon'_p)/d\ln\epsilon'$ (Figure 18b) indicates the domination of particles with higher aspect ratios ($\epsilon' \geq \sim 1.44$). In spite of noted earlier low sensitivity of light scattering to the shape of the aspect ratio distribution for $\epsilon' \geq \sim 1.44$, our retrieval shows (Figure 18b) generally good qualitative agreement with the results of in situ characterization for Saharan dust [Reid et al., 2003b]. Indeed, Reid et al. [2003b] reported median aspect ratio of 1.9–2.2 and cumulative probabilities (measured for different size ranges) indicating that 90% of particles have aspect ratios below 3. Figure 19 illustrates that the spheroid model allows a good fit of both intensity and polarization observations. Assuming a spherical model for inverting the same data does not allow simultaneous good fitting of both radiances and polarization: spheroid model allowed 5% root-mean-square fit for radiances and <0.01 for polarization, while spherical model resulted in 10% root-mean-

square fit for radiances and ~ 0.05 root-mean-square fit for polarization. It is noted (Figure 19) that the residual of fitting the atmospheric radiance measurements is more than twice as small for cases when the spheroid model was used compared to the fit achieved with an assumption of spherical particles. It appears that the assumption of spherical aerosol only allows for fitting of the residual ε_{sky} at the level of $\sim 10\%$ for dust aerosol (this agrees with an earlier analysis of *Tanré et al.* [2001]). These differences seem surprisingly small if one looks at the correspondent phase functions (element $P_{11}(\Theta_j, \lambda_j)$) in Figure 20, where differences between $P_{11}(\Theta_j, \lambda_j)$ of the spherical and nonspherical particle retrievals reach the level of 100–200% and higher. This contrast of large differences in phase functions of spherical and nonspherical aerosol versus rather moderate differences in the angular dependencies of the corresponding atmospheric radiances can be explained by the contributions of molecular scattering (at shorter wavelengths) and multiple scattering to the measurements. Both factors reduce the sensitivity of the atmospheric radiation to the differences in the scattering matrix caused by the deviation of the particle shape from spherical. A similar but weaker tendency can be seen for the degree of linear polarization. As shown in Figure 19 the root-mean-square of polarization fitting with spherical particles was ~ 0.05 which is five times higher than root-mean-square of polarization fitting with spheroids. The spheroid fitting was at the level of measurement error, i.e., below 0.01. It should be noted that the aerosol properties retrieved under assumption of spherical particles demonstrated some pronounced differences with retrieval results obtained using spheroid model. For example the retrieval based on spherical particle assumption resulted in value ~ 1.42 for the real part of the refractive index.

[48] The differences between spheres and spheroids on the modeling of pure aerosol degree of linear polarization $-P_{12}/P_{11}$ (i.e., without mixing with molecular scatter and with no multiple scattering effect) is shown in Figure 20. These differences reach values of 0.2 at some scattering angles. However, the effects of multiple scattering and strong polarization effects of molecular scattering diminish these differences in polarization $P(\lambda; \Theta)$ of atmospheric radiation especially at shorter wavelengths (Figure 19). Nevertheless, it is clear from Figures 19 and 20 that using measurements of both absolute radiance and polarization in aerosol retrievals provides a more distinct discrimination between spherical and nonspherical dust and that the spheroid model allows fitting both intensity and polarization observations of ambient desert dust to the level of measurement accuracy.

4.3. Aerosol Shape Retrieval From AERONET Intensity Observations

[49] The results of the previous section illustrate the possibility of including some parameters of aspect ratio distribution from a combination of ground-based intensity and polarization measurements of atmospheric radiation. Such a strategy allows detect aerosol particle nonsphericity during retrieval instead of assuming it prior to retrieval. It appears that using polarimetric measurements of atmospheric radiation is important for identifying aerosol particle shape. Nevertheless, implementing the same approach

for inverting intensity measurements only also seems promising. Indeed, under the operational protocol of AERONET data processing, all aerosol retrievals are always performed twice: assuming both spherical and nonspherical aerosol models. The original nonspherical model assumed aerosol as a mixture of spheroids with the aspect ratio distribution fixed to the one expected for desert dust. Prior analyses demonstrate that even the AERONET intensity data (with no polarization) exhibit a noticeable sensitivity to aerosol particle shape [see *Dubovik et al.*, 2002b; *Eck et al.*, 2005]. As described in section 4.1, the use of the spheroid model allows for more accurate fitting of observations (lower residuals) and more robust retrievals for desert dust observations while also eliminating known artifacts. For maritime aerosol, the assumption of spherical particles performs better since the coarse mode particles in this case (hydrated sea salt) are in fact nearly spherical. For the situation of fine mode dominated aerosol (e.g., biomass burning) both assumptions produce equivalent retrievals of high quality. The disadvantage of such an operational strategy is the fact that neither spherical nor nonspherical model reproduce adequately the situation where coarse mode composed of mixed aerosols, when both spherical and nonspherical super micron size particles are present. Thus implementing the retrieval of aspect ratio distribution is an attractive and feasible strategy for AERONET operational retrievals. For verifying the potential of this strategy we have applied the new algorithm retrieving $dn(\varepsilon'_p)/d\ln\varepsilon'$ together with aerosol size distribution and complex refractive index to AERONET intensity data. The application of this aerosol retrieval algorithm to a number of AERONET observations has shown that robust retrievals of aerosol aspect ratio distribution can be achieved for coarse mode aerosols. The retrieval was applied only to radiance data sets where measurements covered a large range of scattering angles (i.e., up to 120° and higher). The results (illustrated by Figure 21) suggest that desert dust (Saudi Arabia) aerosol is composed of particles with aspect ratios larger than ~ 1.44 while the retrieval for maritime aerosol (Hawaii) show the domination of spherical particles. This agrees with the conclusion of POLDER aerosol retrievals [*Herman et al.*, 2005]. As expected, the intensity observations of fine mode aerosols, such as biomass burning (Zambia), do not show sensitivity to particle shape (since the scattering by small particles is expected to be independent of particle shape). Figure 21b shows the retrieved aspect ratio distributions that were obtained using $y(\varepsilon'_p) = \text{const}$ as an initial guess for $dn(\varepsilon'_p)/d\ln\varepsilon'$. One can see that in case of biomass burning aerosol the retrieved aspect ratio distribution is equal to the initial guess. The coarse mode presenting in size distribution of Zambia biomass burning aerosol has very small contribution to the optical depth compare to contribution of fine mode.

[50] Thus the basic intensity AERONET data have sensitivity to the aerosol shape distribution of coarse mode aerosols. The retrieval of desert dust cases obtained from AERONET sites at all times and locations show the clear dominance of nonspherical particles with $\varepsilon' \geq \sim 1.44$. However, the exact shape of the retrieved $dn(\varepsilon'_p)/d\ln\varepsilon'$ exhibited noticeable variability between different retrievals. It is unlikely that this variability reflects the variability of actual properties of the aerosol, but is rather a product of the

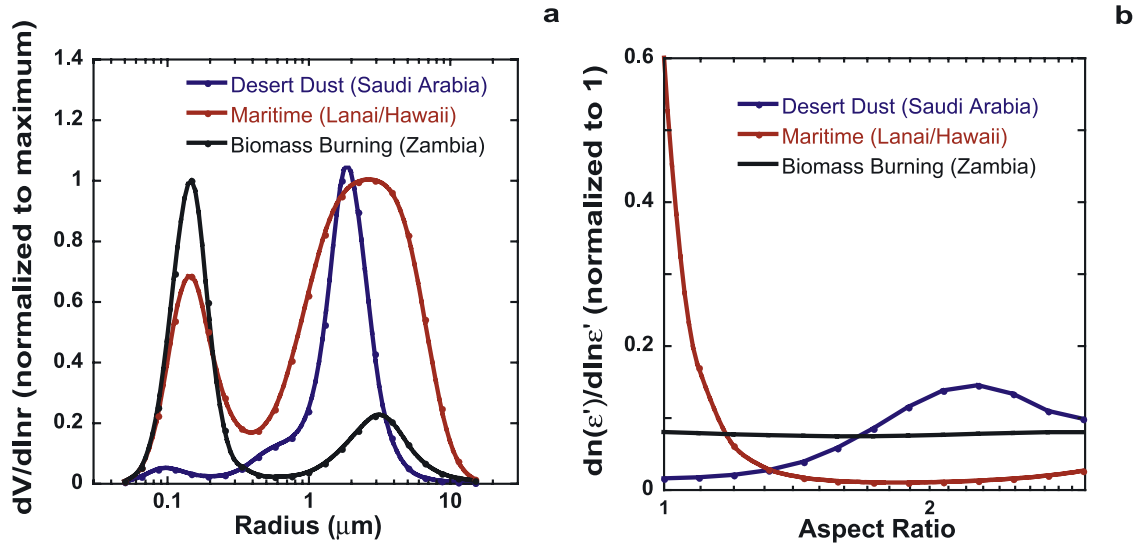


Figure 21. Examples of retrieving complex refractive index, size and aspect ratio distributions from AERONET intensity measurements. (a) Retrieved columnar aerosol size distributions and (b) correspondent retrieved aspect ratio distributions.

limited sensitivity of observations to particle shape. Indeed, similarly to the measurements of full scattering matrices (see discussion in section 3) AERONET observations demonstrate weak sensitivity to the details of aspect ratio distributions for the range of $\epsilon' > \sim 1.44$. In addition, the general sensitivity of AERONET observations to particle shape changes: it decreases for observations with a restricted range of scattering angles and for situations with pronounced presence of fine mode particles. Therefore it appears reasonable to reduce the complex retrieval of the full aspect ratio distribution to a simpler task of retrieving only the fraction (percentages) of nonspherical particles, where the nonspherical particles would be modeled as a mixture of spheroids with a typical aspect ratio distribution observed for strong desert dust events. Such a simplified approach allows fast retrievals (comparable in speed to the current operational AERONET retrieval employing fixed particle shape) and proper modeling of most optically distinct mixtures of coarse aerosols: spherical particles (e.g., maritime aerosol), nonspherical (e.g., desert dust) and their mixtures. The most logical choice would be the shape distribution retrieved by inversions of laboratory measurements [Volten *et al.*, 2001], because at present only these measurements directly provide full scattering matrix in wide scattering angle range ($5^\circ \leq \Theta \leq 175^\circ$). However, the main issue could be the fact that the Feldspar sample analyzed may not necessarily have same property as ambient desert dust aerosol. Nevertheless, comparisons show quite good agreement in principal details between the aspect ratio distributions retrieved from laboratory measurements (Figure 13b) and those retrieved from AERONET dust observations (Figures 18b and 21b). Specifically, all retrieved aspect ratio distributions demonstrate the domination of particles with aspect ratio larger than 1.44 with a moderate increase of particle concentrations with larger aspect ratios. Thus we have employed $dn(\epsilon'_p)/d\ln \epsilon'$ retrieved from laboratory measurements (an average of the ones

retrieved at the two wavelengths, Figure 13b) for modeling the nonspherical aerosol component and for performing the aerosol retrieval of the percentage of nonspherical particles with a priori fixed $dn(\epsilon'_p)/d\ln \epsilon'$. As shown in Figure 22 the results of such retrievals agree well with inversions where the full $dn(\epsilon'_p)/d\ln \epsilon'$ were retrieved.

4.4. Sensitivity of AERONET Observations to Aerosol Shape Distribution

[51] The previous sections describe a new approach where the aerosol particle nonsphericity is retrieved together with other aerosol parameters. However, such approach can only be useful when the measured radiances are sensitive to particle shape, i.e., if the measurement geometry provides coverage of wide range of scattering angles and if the aerosol size distribution has significant coarse mode. Therefore it is helpful to identify when the sensitivity to aerosol particle shape can be expected. In order to evaluate qualitatively the sensitivity of AERONET intensity and polarization measurements to aerosol particle nonsphericity, we calculated intensity and polarization residuals for particles of different sizes. The residuals for intensity (R_I) and polarization (R_P) measurements were defined as follows:

$$R_I = \sqrt{\frac{1}{N_j} \left(\sum_j \left(\frac{I_{sp}(\theta_j) - I_{ns}(\theta_j)}{I_{ns}(\theta_j)} \right)^2 \right)} \times 100$$

and

$$R_P = \sqrt{\frac{1}{N_j} \left(\sum_j (P_{sp}(\theta_j) - P_{ns}(\theta_j))^2 \right)} \times 100, \quad (32)$$

where the subscript *sp* refers to spherical particles and the subscript *ns* refers to nonspherical particles.

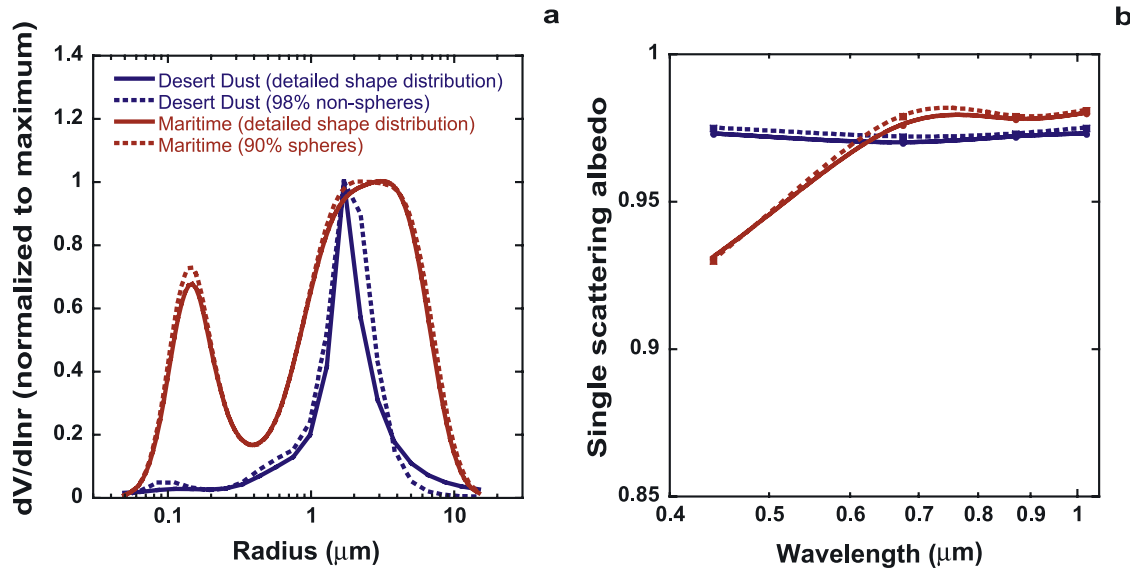


Figure 22. Comparisons of inversion results obtained by two different approaches of aspect ratio parameterization: The first one retrieves the complex refractive index, size distribution and the full aspect ratio distribution (see Figure 21), and the second one retrieves complex refractive index, size distribution and partition between spherical and nonspherical components (for the nonspherical component the aspect ratio distribution is fixed to the average one from those retrieved from Feldspar scattering matrices (see Figure 13b). For example, “90% spherical component” means that retrieval suggests the mixture of 90% spherical and 10% nonspherical particles.

[52] The residuals were calculated using size distributions modeled by a monomodal lognormal function defined as:

$$\frac{dV(r)}{d\ln r} = \frac{C_v}{\sqrt{2\pi}\sigma} \exp\left[-\frac{(\ln r - \ln r_v)^2}{2\sigma^2}\right], \quad (33)$$

where C_v – volume concentration, σ – standard deviation and r_v – median radius. In these simulations the median radius r_v of the size distribution was varied from 0.1 to 5.0 μm , $\sigma = 0.5$ and the complex refractive index was adopted from the retrieval climatology for Saudi Arabian dust [Dubovik et al., 2002a]. The aspect ratio distribution $dn(\xi_p)/d\ln\xi'$ applied was the same as the one retrieved from the Feldspar scattering matrix measurements at $\lambda = 0.441 \mu\text{m}$. The simulations were performed for measurement geometry that provides wide range of scattering angles (i.e., $\Theta \leq 150^\circ$). Figure 23 shows the calculated residuals as a function of the Ångström exponent for 0.44 and 0.87 μm (equation (29)). Using the Ångström exponent instead of the median radius allows the projection of the dependence on more general and realistic situations when aerosol may have more than one mode. Indeed, Ångström parameter can be calculated directly from measured spectral optical thickness with no assumptions about aerosol microphysics and, at the same time, it is usually considered as an indicator of the aerosol size composition [e.g., Eck et al., 1999; O'Neill et al., 2001; Schuster et al., 2006]. Thus Figure 23 illustrates that, if only intensity measurements are used, the aerosol shape retrieval can be beneficial in situations with Ångström

exponents $< \sim 1.0$, i.e., when the aerosols have a pronounced presence of coarse mode particles. If polarization measurements are also used, the sensitivity to particle shape remains even for fine mode aerosol corresponding to high values of the Ångström exponent. It should be noted that in order to avoid ambiguity in the inversion results, all particles are assumed spherical as the initial guess and the particle nonsphericity is allowed only in the latest stages of retrieval if it improves the fit of observation. Therefore, in situations with high Ångström exponents where observations are insensitive to particle shape the retrieval chooses spherical particles even though the nonspherical particles could provide an equally good fit of measurements.

5. Other Applications of Desert Dust Remote Sensing

[53] In addition to AERONET ground-based Sun/sky radiometer aerosol remote sensing (discussed in the previous section), the newly developed kernel look-up table software package can be a useful tool to account for the main features of scattering by nonspherical dust in various aerosol remote sensing applications. Specifically, the aerosol spheroid model can be used for quantitative modeling of passive satellite remote sensing as well as lidar observations that are known to be sensitive to nonsphericity of desert dust particles.

5.1. Modeling of Lidar Observations of Nonspherical Desert Dust Aerosol

[54] The extinction to backscatter lidar ratio $S(\lambda)$ and the linear depolarization ratio $\delta(\lambda)$ are the parameters measured

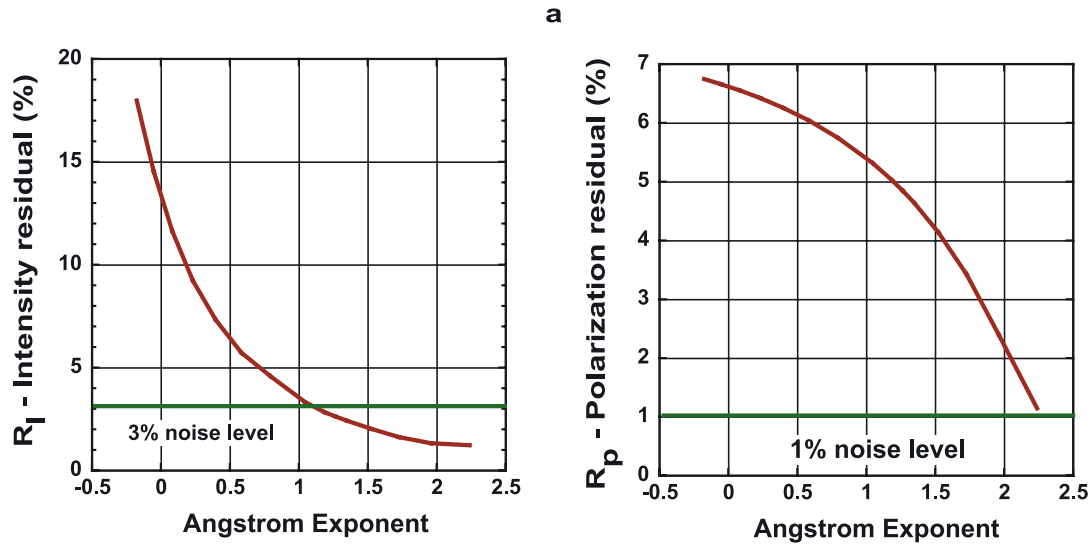


Figure 23. Intensity and polarization residuals between radiation from spherical and nonspherical aerosol simulations. The 3% intensity and 1% polarization noise levels indicate accuracies typically expected in AERONET intensity and polarization measurements.

by lidars and that are known to have sensitivity to the nonsphericity of desert dust particles:

$$S(\lambda) = \frac{4\pi}{\omega_0(\lambda)P_{11}(\lambda, 180^\circ)}, \quad (34)$$

$$\delta(\lambda) = \frac{1 - P_{22}(\lambda, 180^\circ)/P_{11}(\lambda, 180^\circ)}{1 + P_{22}(\lambda, 180^\circ)/P_{11}(\lambda, 180^\circ)} 100\%. \quad (35)$$

The extinction to backscatter lidar ratio $S(\lambda)$ is sensitive to desert dust particle nonsphericity because of the large difference of $P_{11}(180^\circ)$ for spherical and nonspherical coarse particles. As illustrated in Figure 24, $S(\lambda)$ for coarse mode nonspherical aerosol results much lower $S(\lambda)$ than for spherical aerosol with the same size distribution and complex refractive index. Many lidar studies of desert dust [e.g., Sasano and Browell, 1989; Welton et al., 2000; Voss et al., 2001; Liu et al., 2002; Müller et al., 2003, 2004] indicate that observed $S(\lambda)$ has higher values than suggested by dust modeling based on Mie calculations for spherical particles. For example, the review of lidar observations by Cattrall et al. [2005] gives 43 ± 4 as a mean value of $S(\lambda)$ observations for desert dust, while the correspondent simulations with a spherical model suggests 15 ± 2 as a mean value for desert dust $S(\lambda)$. The mean value of $S(\lambda)$ obtained by Cattrall et al. on the basis of a spheroid aerosol parameterization [Dubovik et al., 2002b] was 42 ± 4 , which is very close to the observations. However, the spheroid model by Dubovik et al. [2002b] did not fully explore the possible variability of the axis ratio distribution. The software package described here and the results of the axis ratio distribution retrieval allow more flexibility in the analysis of spheroid model performance for reproducing $S(\lambda)$ of real dust. Figure 24b shows one example, of updated $S(\lambda)$ simulation for desert dust observed during the UAE² experiment.

[55] In addition, the spheroid kernel look-up tables described here allow for modeling and analysis of the linear

depolarization ratio $\delta(\lambda)$ that can be measured by lidars. As can be seen from Figures 8–9 the scattering matrix element P_{22} of nonspherical desert dust is different from P_{11} while for spheres, the particles with highest symmetry, $P_{22} = P_{11}$ [van de Hulst, 1957]; that is, the linear depolarization ratio $\delta(\lambda)$ is always zero for spherical aerosols. Many lidar measurements [e.g., Gobbi et al., 2000; Müller et al., 2003] indicate deviation of $\delta(\lambda)$ from zero for desert dust. For example, Müller et al. [2003] report $\delta(\lambda)$ for desert dust as high as 25%. In order to evaluate qualitatively the performance of the newly developed spheroid mixture in modeling the linear depolarization ratio $\delta(\lambda)$, we have calculated $\delta(\lambda)$ for aerosol with size distributions modeled using monomodal lognormal function (equation (33)). Figure 25 shows the dependence of $P_{22}(\Theta)/P_{11}(\Theta)$ and $\delta(\lambda)$ on the median radius r_v of the size distribution. In these simulations $\sigma = 0.5$ and $dn(\epsilon_p)/d\ln\epsilon$ is the one retrieved from the Feldspar scattering matrix measurements at $\lambda = 0.441 \mu\text{m}$. One can see from Figure 25a that $P_{22}(180^\circ)/P_{11}(180^\circ)$ is different from unity for large nonspherical particles that cause depolarization of fully linearly polarized incident light. Specifically the linear depolarization ratio $\delta(\lambda)$ becomes increasingly different from zero starting from an effective size parameter (calculated as $2\pi r_v/\lambda \sim 2$ and reaches maximum of 0.45 at size parameter ~ 15 then $\delta(\lambda)$ monotonically decreases for size parameter ≥ 15 . This tendency is in qualitative agreement with the calculations of Mishchenko and Sassen [1998], performed for ice spheroids, cylinders and Chebyshev particles using a simple power law aerosol size distribution. Unlike those simulations, the simulations shown in Figure 25 utilized average retrieved axis ratio distribution, a complex refractive index $n = 1.45$, $k = 0.005$ (that is in the middle of tropospheric aerosol complex refractive index range), for a lognormal size distribution and wide median volume radius r_v range (displayed also as the effective size parameter $2\pi r_v/\lambda$). Note that we did not use the aspect ratio distribution shown in Figure 13b, since the assumption of equal

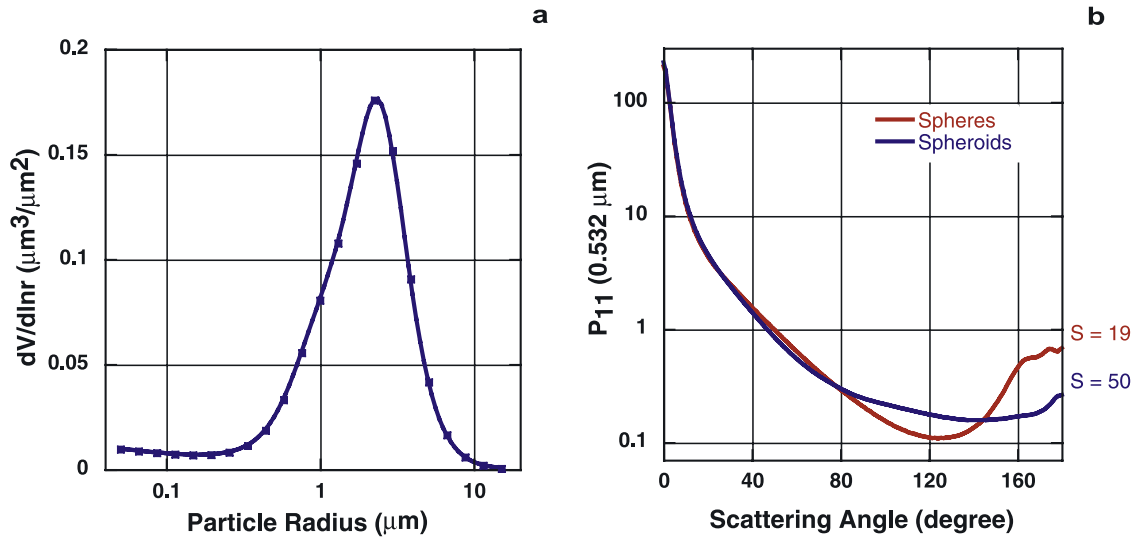


Figure 24. (a) Aerosol size distribution retrieved from AERONET observations during a dust storm in Dhahi/UAE and (b) phase functions calculated using the spherical and spheroid aerosol models for the size distribution shown in Figure 24a.

number of prolate and oblate spheroids seems to decrease the ability of spheroid model to reproduce the angular structure of P_{22} (see Figure 12).

[56] However, using the size dependence of $\delta(\lambda)$ as shown in Figure 25 for the interpretation of lidar remote sensing is problematic, because size distributions of all real tropospheric aerosols including desert dust typically exhibit pronounced bimodality (e.g., see the AERONET aerosol climatologies given by Dubovik *et al.* [2002a]). According to the AERONET retrieval climatology [Dubovik *et al.*, 2002a] desert dust has a coarse mode with r_v between ~ 1.9 and $3 \mu\text{m}$, and has a minor fine mode with r_v of 0.1 – $0.16 \mu\text{m}$. For dust with a bimodal size distribution the variation of $\delta(0.532)$ may be caused not only by changes

in the median size of particles in the coarse mode of desert dust but also by changes of the concentration of the desert dust fine mode. For example, a decrease/increase of $\delta(0.532)$ may be caused by either an increase/decrease of coarse mode r_v or by decrease/increase of the fine mode contribution. Figure 26a illustrates the possible variability of $\delta(0.532)$ of different bimodal (each mode has a lognormal distribution given by equation (33) with $\sigma_1 = \sigma_2 = 0.5$) mixtures of fine spherical particles ($r_{v1} \sim 0.12$ – $0.2 \mu\text{m}$) and coarse nonspherical particles ($r_{v2} \sim 1$ – $5 \mu\text{m}$). In Figure 26a $\delta(0.532)$ is shown as a function of Ångström exponent (based on the same considerations as for Figure 25). One can see from Figure 26a that the linear depolarization ratio of 0.25 observed by Müller *et al.* [2003] can be realized by

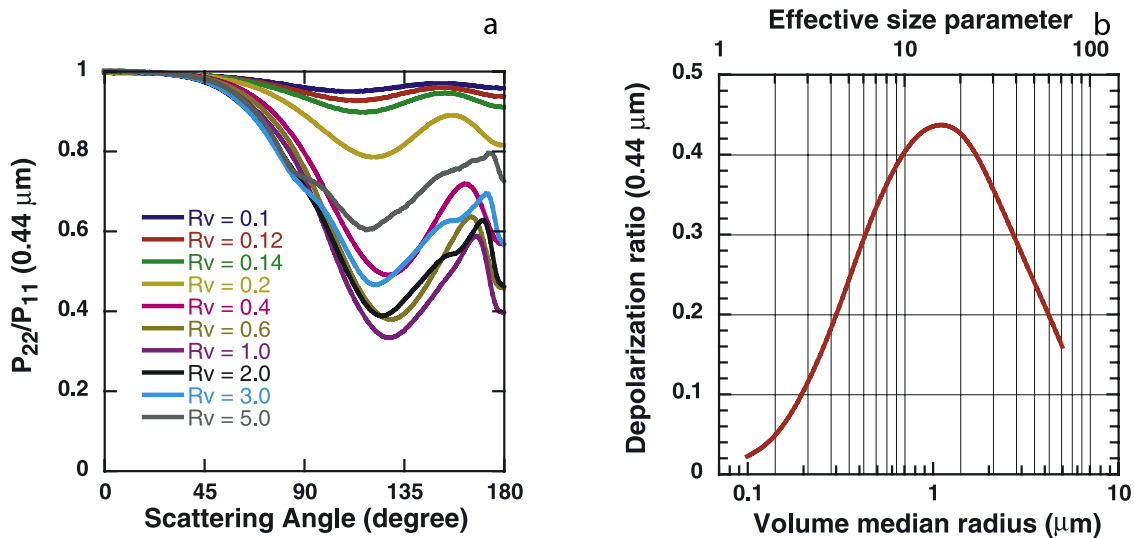


Figure 25. (a) P_{22}/P_{11} calculated for $\lambda = 0.44 \mu\text{m}$ ($n = 1.45$, $k = 0.005$) using the spheroid aerosol model for a monomodal lognormal distribution with different median radii and (b) the correspondent depolarization ratio shown as a function of median radius (lower X axis) and effective size parameter calculated as $2\pi r_v/\lambda$ (upper X axis).

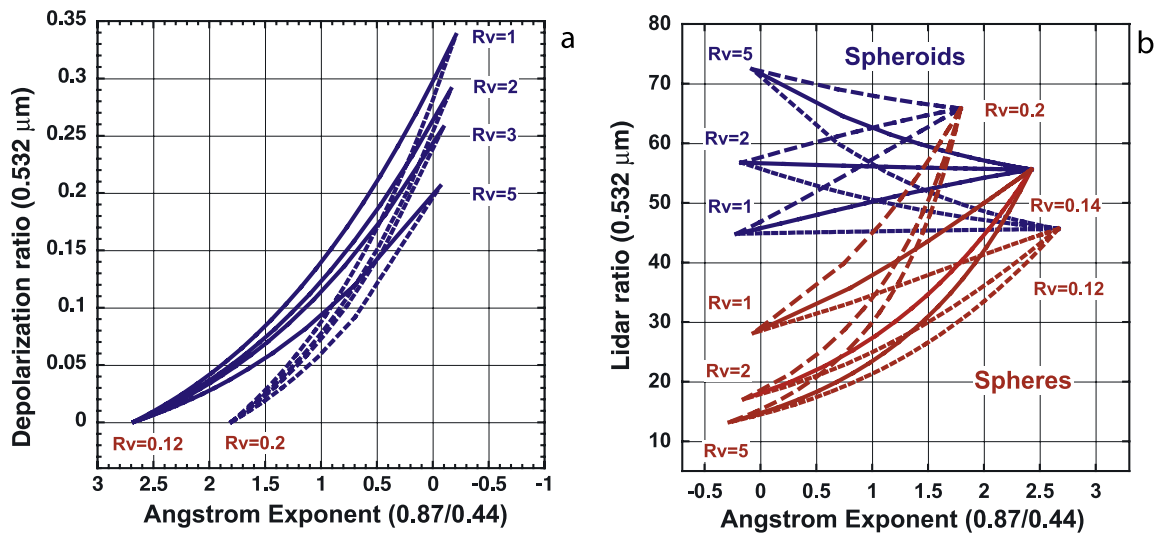


Figure 26. (a) Depolarization ratio plotted as function of the Ångström exponent. Each line shows the dependence of the depolarization ratio for aerosol defined by a lognormal bimodal distribution of spherical (red labels) fine mode (with median radii 0.12 or 0.2 μm) and coarse spheroid mode (blue labels) particles (with median radii 1.0, 2.0, 3.0 or 5.0 μm). (b) Lidar ratio plotted as function of Ångström exponent. Each line shows the dependence of the lidar ratio for aerosol defined by a lognormal bimodal distribution of spherical (red labels) fine mode (with median radii 0.12, 0.14 or 0.2 μm) and coarse spherical (red labels) or spheroid mode (blue labels) (with median radii 1.0, 2.0, 3.0 or 5.0 μm). For example, moving along the solid blue line from $R_v = 0.2$ to $R_v = 5.0$ shows the changes of aspect ratios for different mixtures of small spherical particles with $R_v = 0.2$ and large spheroids with $R_v = 5.0$. The value of α indicates the partitioning between of these two small and coarse particle components. The real and imaginary part of the refractive indices that were used are the same as those given by Dubovik *et al.* [2002a] for Saudi Arabian dust.

several bimodal coarse mode dominated mixtures for an Ångström exponent in the range of -0.1 to 0.4 if r_{v2} of the coarse mode is between 1 and 3 μm . These ranges of α and r_v consistent with the correspondent values observed by Müller *et al.* [2003]. Figure 26b illustrates the variability of the lidar ratio for bimodal mixtures with coarse mode aerosol composed of either spheres or spheroids. When the Ångström exponent is small (i.e., when the coarse mode prevails) the lidar ratio $S(\lambda)$ differs significantly for aerosols with spherical and spheroidal coarse mode particles. This difference increases for larger median radius r_v of coarse mode and Figure 26b can be helpful for evaluating particle shape and median radius r_{v2} of coarse mode. However, the illustrations in Figures 25 and 26 are based on simulations conducted for an aerosol model with selected size distributions, refractive indices and axis ratio distributions. Variations in any of these aerosol characteristics will result in changes in $S(\lambda)$ and $\delta(\lambda)$, nevertheless the qualitative tendencies and ranges of $S(\lambda)$ and $\delta(\lambda)$ variability as shown in Figures 25 and 26 are likely to remain.

5.2. Issues of Aerosol Particle Nonsphericity in Passive Satellite Remote Sensing

[57] The necessity to account for the effects of particle nonsphericity is a well-known issue of passive satellite remote sensing of aerosol. This issue has been analyzed in many studies [e.g., Mishchenko *et al.*, 1995; Kahn *et al.*, 1997; Krotkov *et al.*, 1999; Kalashnikova and Sokolik,

2002; Mishchenko *et al.*, 2003; Kalashnikova and Sokolik, 2004; Kalashnikova *et al.*, 2005; Zhao *et al.*, 2003; Sinyuk *et al.*, 2003; Hsu *et al.*, 2004; Remer *et al.*, 2005] and many satellite retrieval algorithms adopt a methodology to account for desert dust particle nonsphericity. However, at present, there is no single established approach to account for aerosol particle shape, and the methods utilized in different satellite retrieval algorithms are rather diverse. For example, the newest MISR retrieval algorithm relies on desert dust optical properties simulated using model particle shapes based on in situ microphysical data [Kalashnikova and Sokolik, 2004; Kalashnikova *et al.*, 2005]. The MODIS and SeaWiFS groups are exploring the possibility of using an empirical phase function that does not require any assumption of particle shape [Hsu *et al.*, 2004; Remer *et al.*, 2005]. The studies by Krotkov *et al.* [1999], Sinyuk *et al.* [2003], and Zhao *et al.* [2003] have shown that using spheroid desert dust models [Mishchenko *et al.*, 1997] allows identification and accounting for the effects of desert dust particle nonsphericity in TOMS and AVHRR observations.

[58] Nevertheless, in spite of the differences in addressing the issue of particle nonsphericity there is a rather clear understanding and general consensus in all of these approaches that the flattening of $P_{11}(\theta)$ at large scattering angles ($\theta > 90^\circ$) for nonspherical compared to spherical aerosols (e.g., see Figure 15) is the main feature causing differences in radiometric satellite observations of non-

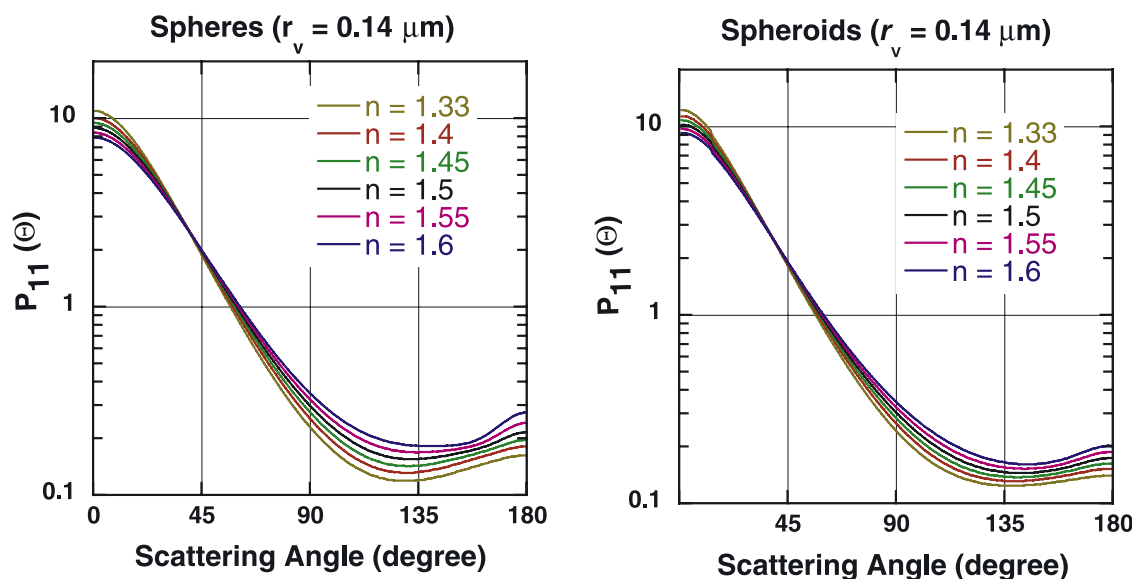


Figure 27. Illustration of the sensitivity of the phase function ($0.44 \mu\text{m}$) of fine mode aerosol to the real part of the refractive index simulated for a monomodal lognormal size distribution ($r_v = 0.14 \mu\text{m}$, $\sigma = 0.5$, $k = 0.005$) of (left) polydisperse spheres and (right) randomly oriented polydisperse spheroids.

spherical desert dust compared to spherical dust model predictions. The situation is more complex when accounting for particle shape effects in aerosol remote sensing from satellite polarimetric observations. The detailed theoretical Lorenz-Mie-based sensitivity analysis of *Mishchenko and Travis* [1997a, 1997b] together with more recent instrumental [Cairns *et al.*, 1999] and methodological developments [Chowdhary *et al.*, 2001, 2002; Mishchenko *et al.*, 2004a] have shown a very high potential of multiangular and multispectral satellite polarimetry for retrieving detailed aerosol properties. However, these studies relied on the spherical aerosol assumption and the importance of accounting for aerosol particle nonsphericity was not fully discussed.

[59] The practical analysis of the POLDER (POLarization and Directionality of Earth's Reflectance) data indicates that accounting for particle nonsphericity is required for using polarization information in satellite retrievals [Deuzé *et al.*, 2000; Herman *et al.*, 2005]. The POLDER instrument [Deschamps *et al.*, 1994] is the first space-borne polarimeter providing spectral (9 spectral channels ranging from 443 to 910 nm), directional (13 different viewing directions) and polarimetric (in channels 443, 670 and 865 nm) observations of atmospheric radiation. The data analysis [Herman *et al.*, 2005] of POLDER-1, which operated during about seven months in 1997, shows that accounting for particle nonsphericity is necessary in order to reproduce observations that correspond to coarse mode aerosols with large real part of the refractive index (i.e., the aerosols that are likely dominated by desert dust). Utilizing the spectrally average mineral dust scattering matrix of Volten *et al.* [2001] allowed Herman *et al.* to eliminate discrepancies between modeling and observations (corresponding to large scattering angles). However, using these measured scattering matrices does not allow for full flexibility of relating light scattering at different wavelengths and in the full range of θ .

Specifically, the scattering matrix provided by Volten *et al.* and utilized by Herman *et al.* is spectrally independent (it is the result of averaging the measurements at two wavelengths). Additionally, using this matrix for radiative transfer modeling requires some nontrivial procedures of extrapolating the measurements into the range of scattering angles less than $\sim 20^\circ$ [Herman *et al.*, 2005] or less than $\sim 5^\circ$ [Liu *et al.*, 2003]. Also, it is problematic to employ this measured scattering matrix for the task of deriving detailed microphysical properties of aerosol.

[60] In these regard the methodology of the present study may be of interest for satellite remote sensing applications. Indeed, Herman *et al.* [2005] reported that their efforts to adopt the spheroid mixture of Mishchenko *et al.* [1997] for reproducing the POLDER measurements were not successful, because the spheroid scattering matrices were exhibiting substantial differences with the measurements of Volten *et al.* [2001]. In contrast, as shown in section 3, the use of the newly developed kernel look-up tables enables the reproduction of the measured scattering matrices by the spheroid mixture in the entire range of measurement scattering angles. Also, as was shown in section 4, the same approach allowed for successful utilization of the spheroid model for interpreting multispectral and multiangle photopolarimetric AERONET measurements. In addition, the very recent studies by Gérard *et al.* [2005] indicated a good qualitative agreement of phase function spectral dependence simulated with spheroid calculations (using the aerosol parameters obtained from fitting Feldspar scattering matrices) with spectral dependence of POLDER observations.

[61] The actual application of the spheroid model for inverting polarimetric satellite data is under development and is beyond the scope of the current paper. Nevertheless, some useful illustrations of particle nonsphericity effects on the sensitivity of polarimetric measurements to aerosol properties can be easily produced using the newly devel-

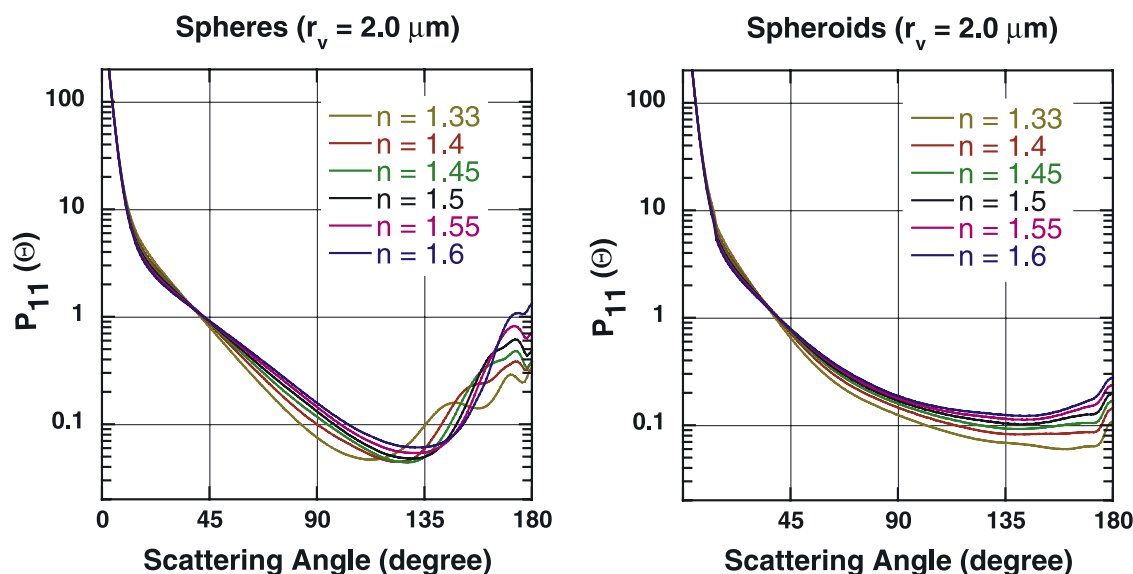


Figure 28. Illustration of the sensitivity of the phase function ($0.44 \mu\text{m}$) of coarse mode aerosol to the real part of the refractive index simulated for a monomodal lognormal size distribution ($r_v = 2.0 \mu\text{m}$, $\sigma = 0.5$, $k = 0.005$) of (left) polydisperse spheres and (right) randomly oriented polydisperse spheroids.

oped spheroid kernel look-up tables. Indeed, rigorous simulations [Mishchenko and Travis, 1994; Mishchenko *et al.*, 1997], as well as laboratory [e.g., Volten *et al.*, 2001; Muñoz *et al.*, 2001] and remote sensing measurements [Deuzé *et al.*, 2000; Herman *et al.*, 1997, 2005] indicate that differences in light scattering between spherical and nonspherical aerosols can be substantial enough to have important consequences for remote sensing. However, the effect of aerosol particle nonsphericity on many particular issues of aerosol remote sensing remains unclear. For example, studies by Wang *et al.* [2003] indicate that correct retrieval of desert dust over ocean requires using a mixture of both

spherical and nonspherical particles due to presence of sea salt in the atmospheric layer. Also, a number of studies based on the spherical aerosol assumption [e.g., Eiden, 1971; Hansen and Travis, 1974; Mishchenko and Travis, 1997a] suggest that measurements of polarization are particularly beneficial for discriminating aerosols by differences in the real part of the refractive index. However, the analysis by Mishchenko *et al.* [2002] indicates important differences in the sensitivity of light scattering of spheres and spheroids to all aerosol parameters including the real part of the refractive index. The spheroid kernel look-up tables enable one to quickly evaluate these differences using

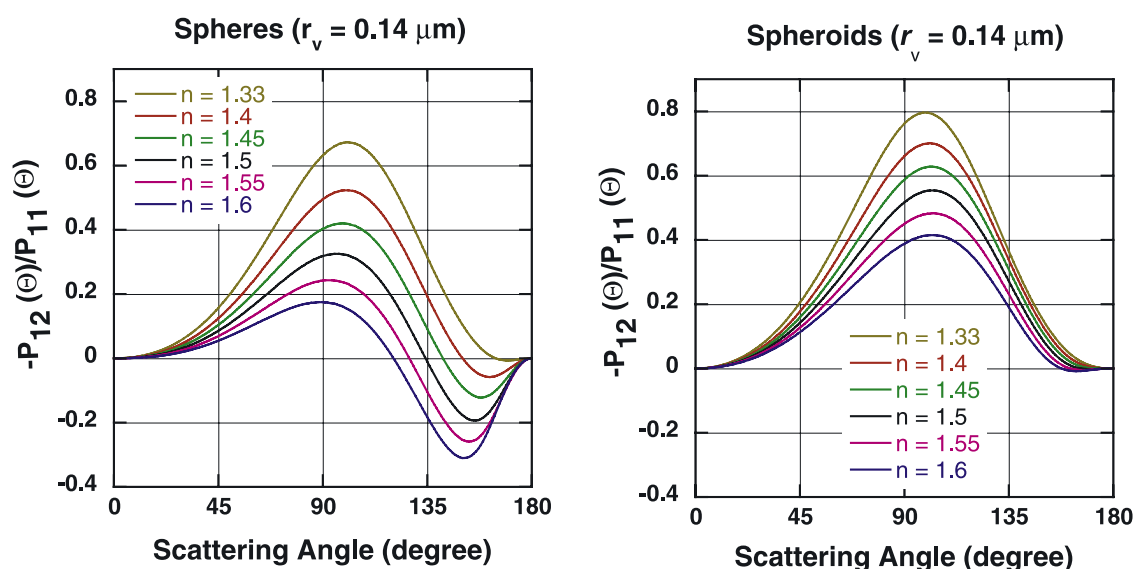


Figure 29. Illustration of the sensitivity of linear polarization at $0.44 \mu\text{m}$ of fine mode aerosol to the real part of the refractive index simulated for a monomodal lognormal size distribution ($r_v = 0.14 \mu\text{m}$, $\sigma = 0.5$, $k = 0.005$) of (left) polydisperse spheres and (right) randomly oriented polydisperse spheroids.

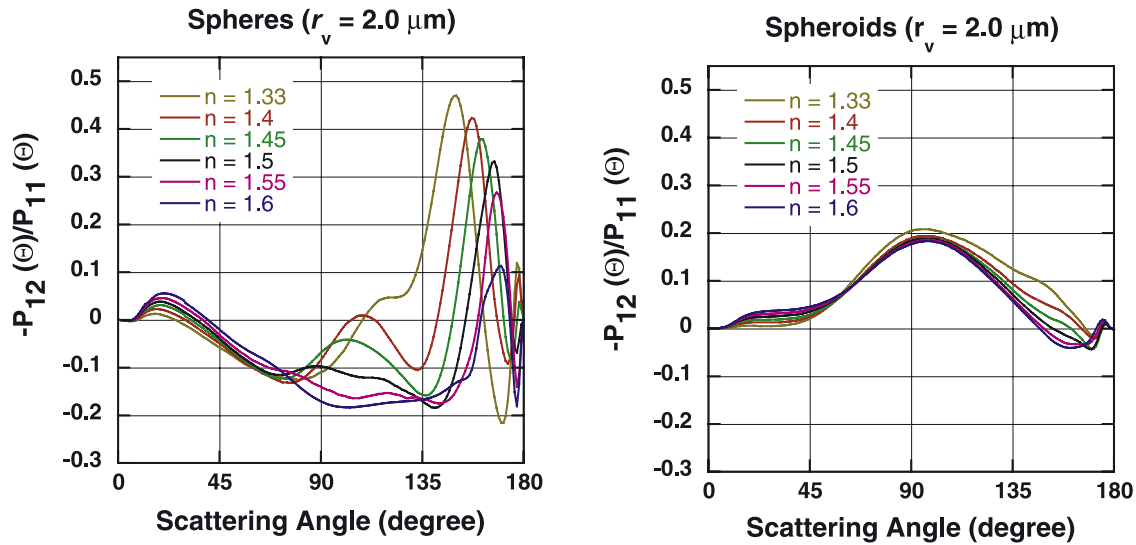


Figure 30. Illustration of the sensitivity of linear polarization at $0.44 \mu\text{m}$ of coarse mode aerosol to the real part of the refractive index simulated for a monomodal lognormal size distribution ($r_v = 2.0 \mu\text{m}$, $\sigma = 0.5$, $k = 0.005$) of (left) polydisperse spheres and (right) randomly oriented polydisperse spheroids.

wide range of aspect ratios and the whole range of particle sizes expected for desert aerosol.

[62] Figures 27–30 show the angular dependencies of $P_{11}(\Theta)$ and $-P_{12}(\Theta)/P_{11}(\Theta)$ at $0.44 \mu\text{m}$ simulated for fine and coarse monomodal aerosols modeled as a spheroid mixture with $dn(\epsilon_p)/d\ln\epsilon'$ (average of those retrieved from the Feldspar scattering matrices measured at 0.44 and $0.633 \mu\text{m}$ and shown in Figure 13) which provided a good fit to both laboratory and ground-based observations (see sections 3 and 4). As expected from previous studies [Mishchenko and Travis, 1997a, 1997b; Mishchenko et al., 2000; Herman et al., 2005], the phase functions P_{11} of both fine and coarse aerosol show some moderate sensitivity to n . For the fine aerosols (Figure 27), the phase functions look nearly identical for both spheres and spheroids. For coarse mode aerosol (Figure 28) the angular dependence of the phase function look substantially different for spheres and spheroids, with slightly lower sensitivity of P_{11} to variations of n for spheroids. The degree of linear polarization $-P_{12}/P_{11}$ shows a high sensitivity to variations of the real part of the refractive index (Figures 29 and 30). It should be noted that the angular dependence of $-P_{12}/P_{11}$ demonstrates generally higher sensitivity to both particle shape and the values of n than the corresponding angular dependence of P_{11} . For example, $-P_{12}/P_{11}$ of fine mode aerosols show strong sensitivity to n , while the angular dependence of $-P_{12}/P_{11}$ clearly differs for spheres and spheroids in Figure 29 in the range of large scattering angles. As expected, the differences in $-P_{12}/P_{11}$ between spheres and spheroids are very significant for coarse mode aerosol, as shown in Figure 30. It is interesting that for spherical coarse mode aerosol, both magnitude and angular behavior of $-P_{12}/P_{11}$ is very different (for $\theta > 90^\circ$) for different n . In the case of spheroids, the differences in $-P_{12}/P_{11}$ for differentiation of n are much less pronounced. Thus the illustrations of Figures 29 and 30 clearly show that the tendencies in light scattering observed with spherical aerosol may not be characteristic for nonspherical aerosols. For

example, $-P_{12}/P_{11}$ for coarse spherical aerosol is very sensitive to n , while $-P_{12}/P_{11}$ of large spheroids show rather weak sensitivity to the real part of the refractive index. Also, for accurate modeling of aerosol polarization the assumption of aerosol particle shape is important even in the case of fine aerosols (Figure 29) in contrast to the intensity of scattered light that is nearly independent of particle shape (Figure 27).

6. Conclusions

6.1. Forward Simulations

[63] The look-up tables of phase matrix, extinction and absorption were calculated for polydisperse randomly oriented spheroids for 25 logarithmically equidistant axis ratios ranging from ~ 0.3 (flattened spheroids) to ~ 3.0 (elongated spheroids). The kernels computed in 41 narrow logarithmically equidistant size bins cover the size parameter ($x = 2\pi r/\lambda$) range from ~ 0.012 to ~ 625 . In order to cover such a large range, two complementary methods were used for computing kernels. For size parameters below $x \sim 30$ – 60 (depending on refractive index and aspect ratio), the simulation were performed using the T -matrix method [Mishchenko and Travis, 1994] which provides an exact solution for electromagnetic radiation scattering by spheroids. For size parameters exceeding the T -matrix convergence limits, the approximated geometric-optics-integral-equation method of Yang and Liou [1996] was used. The kernels cover the following ranges of complex refractive index: $1.33 \leq n \leq 1.6$ and $0.0005 \leq k \leq 0.5$ and allow for simulations of $P_{ii}(\Theta)$ for entire range of scattering angles Θ with 1° resolution. For effectiveness and flexibility of using these computed kernels, a software package has been designed. This software allows for quick simulation of τ_{ext} , τ_{scat} and $P_{ii}(\Theta)$ using following parameters of the spheroid mixture as input: n , k , size distribution ($dV(r_k)/d\ln r$) and axis ratio distributions ($dn(\epsilon_p)/d\ln\epsilon$). The simulations can be done for any λ and r_k within the kernel range of x with

expected average accuracy below 3% for $P_{ii}(\Theta)$ and below 0.005 for τ_{ext} and τ_{scat} . The kernels and software package with detailed description of its functions can be available from the lead author upon request.

6.2. Inversion of Laboratory Measurements of Desert Dust Properties

[64] For the purpose of validating the spheroid approximation, the newly developed software module was incorporated into an algorithm attempting retrieval of an extended set of aerosol parameters including n , k , $dV(r_k)/d\ln r$ and the shape distribution from angular and spectral measurements of the full scattering matrix. This software was applied to laboratory measurements of scattering matrices made by *Volten et al.* [2001]. Inversion of $P_{ii}(\Theta)$ measured for water droplets illustrated the possibility of retrieving aerosol particle shape together with size distribution and complex refractive index. The retrieval clearly identified the spherical character of water droplets and demonstrated a high consistency between spectral and angular measurements with modeling.

[65] The analysis of $P_{ii}(\Theta)$ measured for a Feldspar sample composed of nonspherical particles has shown that our spheroid model can rather adequately reproduce the angular dependence of measured $P_{ii}(\Theta)$ with root-mean-square error of <10%. Moreover, the elements $P_{11}(\Theta)$ and $-P_{12}(\Theta)/P_{11}(\Theta)$, that are most important for passive remote sensing application, could be reproduced with root-mean-square error of only $\sim 3\text{--}4\%$. The worst accuracy of fitting was observed for $P_{22}(\Theta)/P_{11}(\Theta)$ and $P_{34}(\Theta)/P_{11}(\Theta)$ that was at the level of $\sim 15\%$. Nevertheless, the spheroid model was shown to be able to reproduce all of the main features of angular scattering by nonspherical particles with an accuracy far superior than can be achieved under the assumption of particle sphericity. This conclusion is in agreement with a number of previous studies [*Nousiainen and Vermeulen*, 2003; *Veihelmann et al.*, 2004; *Kahnert*, 2004], while our analysis suggests a better fit of spheroid approximation to measurements of $P_{ii}(\Theta)$ of actual mineral aerosol. This can probably be explained by the fact that our newly developed kernel look-up tables allowed simulation of scattering by spheroids with larger size parameters and aspect ratios than previous studies. In addition, we used more flexible procedure of fitting of the measurements that allowed adjustment of larger number of model parameters including n , k , $dV(r_k)/d\ln r$ and the axis ratio distribution. At the same time, our analysis revealed difficulties in reproducing the spectral dependence of the Feldspar scattering matrix, in particular the phase function P_{11} . The simulations with the spheroid model (with Feldspar size distributions and refractive index) suggest nearly spectrally independent P_{11} , while measurements indicate differences of up to 20% in $P_{11}/P_{11}(30^\circ)$ measured at 0.44 and 0.633 μm . This inconsistency can possibly be attributed to limitations of the spheroid model and/or unidentified limitations of $P_{ii}(\Theta)$ measurements with mineral dust samples. The issue remains to be clarified by future studies with more samples and independent measurements.

6.3. Inversion of AERONET Observations

[66] Our new spheroid kernel look-up tables were utilized for the retrieval of aerosol properties from desert dust

observations by Sun/sky radiometers of the AERONET network. First, we refined the spheroid model in the previous AERONET approach that derived complex refractive index and size distribution for nonspherical aerosol using an a priori fixed mixture of spheroids. We have adopted the shape distribution from the laboratory scattering matrix inversion of Feldspar. Second, a new version of the aerosol retrieval algorithm was developed that retrieves information about aerosol nonsphericity in addition to the complex refractive index and size distribution.

[67] Both the previous and the new retrievals show that utilizing the spheroid model significantly improves the retrieval of desert dust from observations with a high sensitivity to aerosol particle nonsphericity (i.e., when measurements cover the scattering angle range from aureole to $>120^\circ$). Specifically, the spheroid model allowed fitting of the entire angular and spectral set of intensity observations to the level of measurement accuracy, i.e., <5% for sky radiances and <0.01 for aerosol optical thickness. Using the spherical model usually resulted in at least a doubling of the sky radiance fitting error. For the case of inverting a new type of AERONET measurements that include spectral and angular measurements of polarization the sensitivity to aerosol particle nonsphericity is even stronger (the spherical assumption results in a 5% residual for the polarization ratio, while using the spheroid model results in a residual below 1%).

[68] Moreover, the application of the new inversion code to retrieve the degree of aerosol nonsphericity together with aerosol refractive index and size distributions from AERONET data was demonstrated. The code provides distinct discrimination of nonspherical coarse mode aerosols from AERONET measurements that cover a wide scattering angle range. The degree of nonsphericity retrieval is particularly fruitful if measurements of polarization are available. For interpretation of AERONET intensity observations only, the aerosol shape retrieval can be beneficial for characterizing aerosols with pronounced presence of coarse mode particles (with Ångström exponent $< \sim 1.0$).

6.4. Details of Aerosol Shape Distribution Retrievals

[69] Several parameterizations of spheroid shape distributions were used in the inversion of laboratory and remote sensing aerosol observations. First, analyzing laboratory measurements of scattering matrices, we attempted to retrieve detailed an axis ratio distribution described by 25 ratios ε_p ranging from 0.3 to 3.0. The inversion of $P_{ii}(\Theta)$ for water droplets demonstrated the domination of spherical particles with a very minor fraction of spheroids with ε between 0.9 and 1.1. (ε of 1 is for spherical shape). In contrast, the inversion of the scattering matrix of a Feldspar sample shows that mineral dust does not have particles with a small degree of nonsphericity ($0.7 < \varepsilon < 1.44$). The inversion of Feldspar $P_{ii}(\Theta)$, as well as numerical simulations, indicates a rather limited sensitivity to details of the axis ratio distributions for ε below ~ 0.7 and higher than 1.44. For example, the discrimination between prolate and oblate spheroids with the same aspect ratio is problematic. Therefore an additional assumption of equal content of both prolate and oblate particles was introduced into the retrieval; that is, the spheroid shape distribution was described by 13 aspect ratios ε'_p ranging from 1.0 to 3.0. Employing this

extra assumption improved the stability of the scattering matrix inversions.

[70] The application of this retrieval methodology to a number of AERONET observations suggested that desert dust aerosol is composed of particles with aspect ratios larger than 1.44 while maritime aerosol is dominated by spherical particles $\varepsilon'_p \leq 1.1$. This agrees with the conclusion based on analyses of spaceborn POLDER data [Herman *et al.*, 2005]. As expected, the intensity observations of fine mode aerosols, such as biomass burning, do not show any sensitivity to particle shape.

[71] The analysis of desert dust aspect ratio distributions retrieved from AERONET observations demonstrated a limited sensitivity to details of the aspect ratio distribution for the range of $\varepsilon'_p > \sim 1.44$ –3.0. Therefore we concluded that for operational purposes, the complex retrieval of the full aspect ratio distribution can be reduced to a simpler task of retrieving only the fraction of nonspherical particles, where the nonspherical particles would be modeled as a mixture of spheroids with an aspect ratio distribution typical of desert dust. For example, we illustrated good performance of this type of retrieval with the aspect ratio distribution used from inversion of scattering matrices measured in laboratory. Such a simplified approach allows for fast retrievals (comparable in speed to the AERONET operational retrieval employing fixed particle shape) and proper modeling of most optically distinct mixtures of coarse mode aerosols: spherical particles (e.g., maritime aerosol), nonspherical (e.g., desert dust) and their mixtures.

6.5. Desert Dust Remote Sensing Applications

[72] We also demonstrated that the new spheroid kernel look-up tables can be a useful tool for various remote sensing applications. It was shown that a moderate amount of computation allows for identification of important tendencies of the effect of aerosol particle nonsphericity on lidar measurements. It was shown that the spheroid model provides the values of extinction-to-backscatter lidar ratios in the range from ~ 40 to ~ 75 and values of depolarization ratio in the range from 10 to 30% for the aerosol with pronounced presence of coarse mode particles when Ångström exponent is less than 1. Also, it was shown that aerosol particle nonsphericity is an important factor affecting the sensitivity of remote sensing observations. For example, it was illustrated that intensity measurements are sensitive to particle nonsphericity of only coarse mode aerosols, while measurements of polarization have some sensitivity to nonsphericity even in the case of fine mode aerosols. In addition, it was shown that the polarization of light scattered by nonspherical coarse mode aerosols has minor sensitivity to the real part of the refractive index of aerosol particles. This is contrasting with known high sensitivity of the polarization of light scattered by large spherical particles to the real part of the refractive index.

[73] Thus our study has shown that the refined spheroid mixture parameterization can adequately describe a number of features of desert dust scattering properties associated with particle nonsphericity. It is also expected that our kernel look-up tables may be a useful tool for various remote sensing applications that would result in further clarification of both the potential and the limitations of

using spheroids for the modeling of desert dust light scattering.

[74] **Acknowledgments.** We thank the EOS Project Science Office for continued support. Michael Mishchenko acknowledges support from the NASA Radiation Sciences Program managed by Hal Maring and from the NASA Glory Mission project. We also thank the AERONET staff for the data collection, calibration and processing. Special thanks go to Jeff Reid, Joop Hovenier, Robert Fraser, and an anonymous reviewer for useful comments that have helped us to improve the paper.

References

- Ångström, A. (1929), On the atmospheric transmission of sun radiation and on dust in the air, *Geogr. Ann.*, **11**, 156–166.
- Arimoto, R., et al. (1997), Mass-particle size distributions of atmospheric dust and the dry deposition of dust to the remote ocean, *J. Geophys. Res.*, **102**, 15,867–15,874.
- Bohren, C. F., and D. R. Huffman (1983), *Absorption and Scattering of Light by Small Particles*, John Wiley, Hoboken, N. J.
- Bohren, C. F., and S. B. Singham (1991), Backscattering by nonspherical particles: A review of methods and suggested new approaches, *J. Geophys. Res.*, **96**, 5269–5277.
- Bond, T. C., M. Bussemer, B. Wehner, S. Keller, R. J. Charlson, and J. Heintzenberg (1999), Light absorption by primary particle emissions from a lignite burning plant, *Environ. Sci. Technol.*, **33**, 3887–3891.
- Cairns, B., L. D. Travis, and E. E. Russell (1999), The Research Scanning Polarimeter: Calibration and ground-based measurements, *Proc. SPIE Int. Soc. Opt. Eng.*, **3754**, 186–196.
- Cattrall, C., J. Reagan, K. Thome, and O. Dubovik (2005), Variability of aerosol and spectral lidar and backscatter and extinction ratios of key aerosol types derived from selected Aerosol Robotic Network locations, *J. Geophys. Res.*, **110**, D10S11, doi:10.1029/2004JD005124.
- Chamailard, K., and J.-P. J. Lafon (2001), Statistical approach of the effects of roughness on the polarization of light scattered by dust grains, *J. Quant. Spectrosc. Radiat. Transfer*, **70**, 519–528.
- Chowdhary, J., B. Cairns, M. Mishchenko, and L. Travis (2001), Retrieval of aerosol properties over the ocean using multispectral and multiangle photopolarimetric measurements from the Research Scanning Polarimeter, *Geophys. Res. Lett.*, **28**, 243–246.
- Chowdhary, J., B. Cairns, and L. D. Travis (2002), Case studies of aerosol retrievals over the ocean from multiangle, multispectral photopolarimetric remote sensing data, *J. Atmos. Sci.*, **59**, 383–397.
- Deschamps, P. Y., F. M. Bréon, M. Leroy, A. Podaire, A. Bricaud, J. C. Buriez, and G. Seze (1994), The POLDER mission: Instrument characteristics and scientific objectives, *IEEE Trans. Geosci. Remote Sens.*, **32**, 598–615.
- Deuzé, J. L., M. Herman, and R. Santer (1989), Fourier series expansion of the transfer equation in the atmosphere-ocean system, *J. Quant. Spectrosc. Radiat. Transfer*, **41**(6), 483–494.
- Deuzé, J. L., P. Goloub, M. Herman, A. Marchand, G. Perry, S. Susana, and D. Tanré (2000), Estimate of the aerosols properties over the ocean with POLDER, *J. Geophys. Res.*, **105**, 15,329–15,346.
- Draine, B. T., and J. P. Flatau (1994), Discrete-dipole approximation for scattering calculations, *J. Opt. Soc. Am. A Opt. Image Sci.*, **11**, 1491–1499.
- Dubovik, O. (2004), Optimization of numerical inversion in photopolarimetric remote sensing, in *Photopolarimetry in Remote Sensing*, edited by G. Videen, Y. Yatskiv, and M. Mishchenko, pp. 65–106, Springer, New York.
- Dubovik, O., and M. D. King (2000), A flexible inversion algorithm for retrieval of aerosol optical properties from sun and sky radiance measurements, *J. Geophys. Res.*, **105**, 20,673–20,696.
- Dubovik, O., et al. (2000), Accuracy assessments of aerosol optical properties retrieved from AERONET sun and sky radiance measurements, *J. Geophys. Res.*, **105**, 9791–9806.
- Dubovik, O., et al. (2002a), Variability of absorption and optical properties of key aerosol types observed in worldwide locations, *J. Atmos. Sci.*, **59**, 590–608.
- Dubovik, O., B. N. Holben, T. Lapyonok, A. Sinyuk, M. I. Mishchenko, P. Yang, and I. Slutsker (2002b), Non-spherical aerosol retrieval method employing light scattering by spheroids, *Geophys. Res. Lett.*, **29**(10), 1415, doi:10.1029/2001GL014506.
- Eck, T. F., B. N. Holben, J. S. Reid, O. Dubovik, S. Kinne, A. Smirnov, N. T. O'Neill, and I. Slutsker (1999), The wavelength dependence of the optical depth of biomass burning, urban and desert dust aerosols, *J. Geophys. Res.*, **104**, 31,333–31,350.
- Eck, T. F., et al. (2005), Columnar aerosol optical properties at AERONET sites in central-eastern Asia and aerosol transport to the tropical mid-Pacific, *J. Geophys. Res.*, **110**, D06202, doi:10.1029/2004JD005274.

- Eiden, E. (1971), Determination of complex index of refraction of spherical aerosol particles, *Appl. Opt.*, **10**, 749–758.
- Gérard, B., J. L. Déuze, M. Herman, Y. J. Kaufman, P. Lallart, C. Oudard, L. A. Remer, B. Roger, B. Six, and D. Tanré (2005), Comparisons between POLDER 2 and MODIS/Terra aerosol retrievals over ocean, *J. Geophys. Res.*, **110**, D24211, doi:10.1029/2005JD006218.
- Gobbi, G. P., F. Barnaba, R. Giorgi, and A. Santacasa (2000), Altitude-resolved properties of a Saharan dust event over the Mediterranean, *Atmos. Environ.*, **34**, 5119–5127.
- Han, Q., W. B. Rossow, J. Chou, K.-S. Kuo, and R. M. Welch (1999), The effects of aspect ratio and surface roughness on satellite retrievals of ice-cloud properties, *J. Quant. Spectrosc. Radiat. Transfer*, **63**, 559–583.
- Hansen, J. E., and L. D. Travis (1974), Light scattering in planetary atmospheres, *Space Sci. Rev.*, **16**, 527–610.
- Haywood, J., P. Francis, S. Osborne, M. Glew, N. Loeb, E. Highwood, D. Tanré, G. Myhre, P. Formenti, and E. Hirst (2003), Radiative properties and direct radiative effect of Saharan dust measured by the C-130 aircraft during SHADE: 1. Solar spectrum, *J. Geophys. Res.*, **108**(D18), 8577, doi:10.1029/2002JD002687.
- Heintzenberg, J. (1998), Particle size distributions from scattering measurements of nonspherical particles via Mie-theory, *Beitr. Phys. Atmos.*, **51**, 91–99.
- Herman, M., J. L. Deuzé, C. Devaux, P. Goloub, F. M. Bréon, and D. Tanré (1997), Remote sensing of aerosols over land surfaces including polarization measurements and application to POLDER measurements, *J. Geophys. Res.*, **102**(D14), 17,039–17,050.
- Herman, M., J. L. Deuzé, A. Marchand, B. Roger, and P. Lallart (2005), Aerosol remote sensing from POLDER/ADEOS over the ocean: Improved retrieval using a nonspherical particle model, *J. Geophys. Res.*, **110**, D10S02, doi:10.1029/2004JD004798.
- Holben, B. N., et al. (1998), AERONET—A federated instrument network and data archive for aerosol characterization, *Remote Sens. Environ.*, **66**, 1–16.
- Holben, B. N., et al. (2001), An emerging ground-based aerosol climatology: Aerosol optical depth from AERONET, *J. Geophys. Res.*, **106**, 12,067–12,097.
- Hovenier, J. W., and C. V. M. van der Mee (1983), Fundamental relationships relevant to the transfer of polarized light in a scattering atmosphere, *Astron. Astrophys.*, **128**, 1–16.
- Hovenier, J. W., and C. V. M. van der Mee (2000), Basic relationships for matrices describing scattering by small particles, in *Light Scattering by Nonspherical Particles*, edited by M. I. Mishchenko, J. W. Hovenier, and L. D. Travis, pp. 61–85, Elsevier, New York.
- Hovenier, J. W., H. Volten, O. Muñoz, W. J. van der Zande, and L. B. F. M. Waters (2003), Laboratory studies of scattering matrices for randomly oriented particles: Potentials, problems, and perspectives, *J. Quant. Spectrosc. Radiat. Transfer*, **79**, 741–755.
- Hovenier, J. W., C. van der Mee, and H. Domke (2004), *Transfer of Polarized Light in Planetary Atmospheres*, Springer, New York.
- Hsu, N. C., S. C. Tsay, M. D. King, and J. R. Herman (2004), Aerosol properties over bright reflecting source regions, *IEEE Trans. Geosci. Remote Sens.*, **42**, 557–569.
- Jaggard, D. L., et al. (1981), Light scattering from particles of regular and irregular shape, *Atmos. Environ.*, **15**, 2511–2519.
- Kahn, R., et al. (1997), Sensitivity of multiangle remote sensing observations to aerosol sphericity, *J. Geophys. Res.*, **102**, 16,861–16,870.
- Kahnert, M. (2004), Reproducing the optical properties of fine desert dust aerosols using ensembles of simple model particles, *J. Quant. Spectrosc. Radiat. Transfer*, **85**, 231–249.
- Kalashnikova, O. V., and I. N. Sokolik (2002), Importance of shapes and compositions of wind-blown dust particles for remote sensing at solar wavelengths, *Geophys. Res. Lett.*, **29**(10), 1398, doi:10.1029/2002GL014947.
- Kalashnikova, O. V., and I. N. Sokolik (2004), Modeling the radiative properties of nonspherical soil-derived mineral aerosols, *J. Quant. Spectrosc. Radiat. Transfer*, **87**, 137–166.
- Kalashnikova, O. V., R. Kahn, I. N. Sokolik, and W. Li (2005), Ability of multiangle remote sensing observations to identify and distinguish mineral dust types: Optical models and retrievals of optically thick plumes, *J. Geophys. Res.*, **110**, D18S14, doi:10.1029/2004JD004550.
- Kaufman, Y. J. (1993), Aerosol optical-thickness and atmospheric path radiance, *J. Geophys. Res.*, **98**, 2677–2692.
- King, M. D., D. M. Byrne, B. M. Herman, and J. A. Reagan (1978), Aerosol size distributions obtained by inversion of spectral optical depth measurements, *J. Atmos. Sci.*, **21**, 2153–2167.
- Koepke, P., and M. Hess (1988), Scattering functions of tropospheric aerosols: The effects of nonspherical particles, *Appl. Opt.*, **27**, 2422–2430.
- Konert, M., and J. Vandenberghe (1997), Comparison of laser grain size analysis with pipette and sieve analysis: A solution for the underestimation of the clay fraction, *Sedimentology*, **44**, 532–535.
- Krotkov, N. A., et al. (1999), Effect of particle nonsphericity on satellite monitoring of drifting volcanic ash clouds, *J. Quant. Spectrosc. Radiat. Transfer*, **63**, 613–630.
- Li, C., G. W. Kattawar, and P. Yang (2004), Effects of surface roughness on light scattering by small particles, *J. Quant. Spectrosc. Radiat. Transfer*, **89**, 123–131.
- Li, Z. Q., P. Goloub, C. Devaux, X. F. Gu, Y. L. Qiao, F. S. Zhao, and H. B. Chen (2004), Aerosol polarized phase function and single-scattering albedo retrieved from ground-based measurements, *Atmos. Res.*, **71**, 233–241.
- Li-Jones, X., and J. M. Prospero (1998), Variations in the size distribution of non-sea-salt sulfate aerosol in the marine boundary layer at Barbados: Impact of African dust, *J. Geophys. Res.*, **103**, 16,073–16,084.
- Liu, L., M. I. Mishchenko, J. W. Hovenier, H. Volten, and O. Muñoz (2003), Scattering matrix of quartz aerosols: Comparison and synthesis of laboratory and Lorenz-Mie results, *J. Quant. Spectrosc. Radiat. Transfer*, **79**, 911–920.
- Liu, Y. G., W. P. Arnott, and J. Hallett (1999), Particle size distribution retrieval from multispectral optical depth: Influences of particle nonsphericity and refractive index, *J. Geophys. Res.*, **104**, 31,753–31,762.
- Liu, Z., N. Sugimoto, and T. Murayama (2002), Extinction-to-backscatter ratio of Asian dust observed with high-spectral-resolution lidar and Raman lidar, *Appl. Opt.*, **41**, 2760–2767.
- Min, M., J. W. Hovenier, and A. de Koter (2005), Modeling optical properties of cosmic dust grains using a distribution of hollow spheres, *Astron. Astrophys.*, **432**, 909–920.
- Mishchenko, M. I., and J. W. Hovenier (1995), Depolarization of light backscattered by randomly oriented nonspherical particles, *Opt. Lett.*, **20**, 1356–1358.
- Mishchenko, M. I., and K. Sassen (1998), Depolarization of lidar returns by small ice crystals: An application to contrails, *Geophys. Res. Lett.*, **25**, 309–312.
- Mishchenko, M. I., and L. D. Travis (1994), *T*-matrix computations of light scattering by large spheroidal particles, *Opt. Commun.*, **109**, 16–21.
- Mishchenko, M. I., and L. D. Travis (1997a), Satellite retrieval of aerosol properties over the ocean using polarization as well as intensity of reflected sunlight, *J. Geophys. Res.*, **102**, 16,989–17,013.
- Mishchenko, M. I., and L. D. Travis (1997b), Satellite retrieval of aerosol properties over the ocean using measurements of reflected sunlight: Effect of instrumental errors and aerosol absorption, *J. Geophys. Res.*, **102**, 13,543–13,553.
- Mishchenko, M. I., A. A. Lacis, B. E. Carlson, and L. D. Travis (1995), Nonsphericity of dust-like aerosols: Implications for aerosol remote sensing and climate modeling, *Geophys. Res. Lett.*, **22**, 1077–1080.
- Mishchenko, M. I., et al. (1997), Modeling phase functions for dustlike tropospheric aerosols using a shape mixture of randomly oriented poly-disperse spheroids, *J. Geophys. Res.*, **102**, 16,831–16,847.
- Mishchenko, M. I., J. W. Hovenier, and L. D. Travis (Eds.) (2000), *Light Scattering by Nonspherical Particles*, Elsevier, New York.
- Mishchenko, M. I., L. D. Travis, and A. A. Lacis (2002), *Scattering, Absorption, and Emission of Light by Small Particles*, Cambridge Univ. Press, New York. (Available at <http://www.giss.nasa.gov/~crim/books.html>)
- Mishchenko, M. I., I. V. Geogdzhayev, L. Liu, J. A. Ogren, A. A. Lacis, W. B. Rossow, J. W. Hovenier, H. Volten, and O. Muñoz (2003), Aerosol retrievals from AVHRR radiances: Effects of particle nonsphericity and absorption and an updated long-term global climatology of aerosol properties, *J. Quant. Spectrosc. Radiat. Transfer*, **79/80**, 953–972.
- Mishchenko, M. I., B. Cairns, J. E. Hansen, L. D. Travis, R. Burg, Y. J. Kaufman, J. V. Martins, and E. P. Shettle (2004a), Monitoring of aerosol forcing of climate from space: Analysis of measurement requirements, *J. Quant. Spectrosc. Radiat. Transfer*, **88**, 149–161.
- Mishchenko, M. I., G. Videen, V. A. Babenko, N. G. Khlebtsov, and T. Wriedt (2004b), *T*-matrix theory of electromagnetic scattering by particles and its applications: A comprehensive reference database, *J. Quant. Spectrosc. Radiat. Transfer*, **88**, 357–406.
- Mishchenko, M. I., L. D. Travis, and A. A. Lacis (2006), *Multiple Scattering of Light by Particles: Radiative Transfer and Coherent Backscattering*, Cambridge Univ. Press, New York.
- Müller, D., I. Mattis, U. Wandinger, A. Ansmann, D. Althausen, O. Dubovik, S. Eckhardt, and A. Stohl (2003), Saharan dust over a central European EARLINET-AERONET site: Combined observations with Raman lidar and Sun photometer, *J. Geophys. Res.*, **108**(D12), 4345, doi:10.1029/2002JD002918.
- Müller, D., O. Dubovik, A. Sinyuk, I. Mattis, U. Wandinger, and A. Ansmann (2004), Aerosol characterization with EARLINET Raman lidar and AERONET Sun photometer, *Opt. Pura Apl.*, **37**, 3581–3584.
- Muñoz, O., H. Volten, J. F. de Haan, W. Vassen, and J. W. Hovenier (2001), Experimental determination of scattering matrices of randomly oriented

- fly ash and clay particles at 442 and 633 nm, *J. Geophys. Res.*, **106**, 22,833–22,844.
- Muñoz, O., H. Volten, J. W. Hovenier, B. Veihelmann, W. J. van der Zande, L. B. F. M. Waters, and W. I. Rose (2004), Scattering matrices of volcanic ash particles of Mount St. Helens, Redoubt, and Mount Spurr Volcanoes, *J. Geophys. Res.*, **109**, D16201, doi:10.1029/2004JD004684.
- Nakajima, T., M. Tanaka, M. Yamano, M. Shiobara, K. Arao, and Y. Nakanishi (1989), Aerosol optical characteristics in the yellow sand events observed in May, 1982 at Nagasaki—Part 2: Models, *J. Meteorol. Soc. Jpn.*, **67**, 279–291.
- Nakajima, T., et al. (1996), Use of sky brightness measurements from ground for remote sensing of particulate polydispersions, *Appl. Opt.*, **35**, 2672–2686.
- Nousiainen, T., and K. Vermeulen (2003), Comparison of measured single-scattering matrix of feldspar particles with T-matrix simulations using spheroids, *J. Quant. Spectrosc. Radiat. Transfer*, **79**, 1031–1042.
- Nousiainen, T., K. Muinonen, and P. Räisänen (2003), Scattering of light by large Saharan dust particles in a modified ray optics approximation, *J. Geophys. Res.*, **108**(D1), 4025, doi:10.1029/2001JD001277.
- Nousiainen, T., M. Kahnert, and B. Veihelmann (2006), Light scattering modeling of small feldspar aerosol particles using polyhedral prisms and spheroids, *J. Quant. Spectrosc. Radiat. Transfer*, **101**, 471–487.
- O'Neill, N. T., T. F. Eck, B. N. Holben, A. Smirnov, O. Dubovik, and A. Royer (2001), Bimodal size distribution influences on the variation of Angstrom derivatives in spectral and optical depth space, *J. Geophys. Res.*, **106**(D9), 9787–9806.
- Reid, J. S., R. G. Floccini, T. N. Cahill, R. Ruth, and D. P. Salgado (1994), Local meteorological, transport, and source aerosol characteristics of late autumn Owens Lake dust storms, *Atmos. Environ.*, **28**, 1699–1706.
- Reid, J. S., T. F. Eck, S. A. Christopher, P. V. Hobbs, and B. N. Holben (1999), Use of the Angstrom exponent to estimate the variability of optical and physical properties of aging smoke particles in Brazil, *J. Geophys. Res.*, **104**, 27,473–27,489.
- Reid, J. S., et al. (2003a), Comparison of size and morphological measurements of coarse mode dust particles from Africa, *J. Geophys. Res.*, **108**(D19), 8593, doi:10.1029/2002JD002485.
- Reid, E. A., J. S. Reid, M. M. Meier, M. R. Dunlap, S. S. Cliff, A. Broumas, K. Perry, and H. Maring (2003b), Characterization of African dust transported to Puerto Rico by individual particle and size segregated bulk analysis, *J. Geophys. Res.*, **108**(D19), 8591, doi:10.1029/2002JD002935.
- Reid, J. S., S. J. Piketh, B. N. Holben, R. T. Bruinijes, D. L. Westphal, A. Mandoos, and A. Mangoosh (2005), A sustained environmental assessment program in southwest Asia, *Eos Trans. AGU*, **86**(52), Fall Meet. Suppl., Abstract A44A-05.
- Remer, L. A., et al. (2005), The MODIS aerosol algorithm, products and validation, *J. Atmos. Sci.*, **62**, 947–973.
- Sasano, Y., and E. V. Browell (1989), Light scattering characteristics of various aerosol types derived from multiple wavelength lidar observations, *Appl. Opt.*, **28**, 1670–1679.
- Schuster, G., O. Dubovik, and B. N. Holben (2006), Angstrom exponent and bimodal aerosol size distributions, *J. Geophys. Res.*, **111**, D07207, doi:10.1029/2005JD006328.
- Shcherbakov, V., J.-F. Gayet, B. Baker, and P. Lawson (2006), Light scattering by single natural ice crystals, *J. Atmos. Sci.*, **63**(5), 1513–1525, doi:10.1175/JAS3690.1.
- Sinyuk, A., O. Torres, and O. Dubovik (2003), Combined use of satellite and surface observations to infer the imaginary part of refractive index of Saharan dust, *Geophys. Res. Lett.*, **30**(2), 1081, doi:10.1029/2002GL016189.
- Smirnov, A., B. N. Holben, O. Dubovik, R. Frouin, T. F. Eck, and I. Slutsker (2003), Maritime component in aerosol optical models derived from Aerosol Robotic Network data, *J. Geophys. Res.*, **108**(D1), 4033, doi:10.1029/2002JD002701.
- Sun, W., N. G. Loeb, G. Videen, and Q. Fu (2004), Examination of surface roughness on light scattering by long ice columns by use of a two-dimensional finite-difference time-domain algorithm, *Appl. Opt.*, **43**, 1957–1964.
- Tanré, D., Y. J. Kaufman, B. N. Holben, B. Chatenet, A. Karnieli, F. Lavenu, L. Blarel, O. Dubovik, L. A. Remer, and A. Smirnov (2001), Climatology of dust aerosol size distribution and optical properties derived from remotely sensed data in the solar spectrum, *J. Geophys. Res.*, **106**, 18,205–18,218.
- Tanré, D., J. Haywood, J. Pelon, J. F. Léon, B. Chatenet, P. Formenti, P. Francis, P. Goloub, E. J. Highwood, and G. Myhre (2003), Measurement and modeling of the Saharan dust radiative impact: Overview of the Saharan Dust Experiment (SHADE), *J. Geophys. Res.*, **108**(D18), 8574, doi:10.1029/2002JD003273.
- Twomey, S. (1977), *Introduction to the Mathematics of Inversion in Remote Sensing and Indirect Measurements*, Elsevier, New York.
- van de Hulst, H. C. (1957), *Light Scattering by Small Particles*, John Wiley, Hoboken, N. J.
- Veihelmann, B. (2005), Sunlight on atmospheric water vapor and mineral dust: Modeling the link between laboratory data and remote sensing, Ph.D. thesis, Radboud Univ., Nijmegen, Netherlands.
- Veihelmann, B., H. Volten, and W. J. van der Zande (2004), Light reflected by an atmosphere containing irregular mineral dust aerosol, *Geophys. Res. Lett.*, **31**, L04113, doi:10.1029/2003GL018229.
- Vermeulen, A., C. Devaux, and M. Herman (2000), Retrieval of the scattering and microphysical properties of aerosols from ground-based optical measurements including polarization. I. Method, *Appl. Opt.*, **39**, 6207–6220.
- Volten, H., O. Muñoz, E. Rol, J. F. de Haan, W. Vassen, J. W. Hovenier, K. Muinonen, and T. Nousiainen (2001), Scattering matrices of mineral aerosol particles at 441.6 nm and 632.8 nm, *J. Geophys. Res.*, **106**, 17,375–17,401.
- Volten, H., O. Muñoz, J. W. Hovenier, J. F. de Haan, W. Vassen, and W. J. van der Zande (2005), WWW scattering matrix database for small mineral particles at 441.6 and 632.8 nm, *J. Quant. Spectrosc. Radiat. Transfer*, **90**, 191–206.
- Voss, K. J., E. J. Welton, P. K. Quinn, J. Johnson, A. M. Thompson, and H. R. Gordon (2001), Lidar measurements during Aerosol99, *J. Geophys. Res.*, **106**, 20,821–20,831.
- Wang, J., X. Liu, S. A. Christopher, J. S. Reid, E. Reid, and H. Maring (2003), The effects of non-sphericity on geostationary satellite retrievals of dust aerosols, *Geophys. Res. Lett.*, **30**(24), 2293, doi:10.1029/2003GL018697.
- Welton, E. J., et al. (2000), Ground-based lidar measurements of aerosols during ACE-2: Instrument description, results, and comparisons with other ground-based and airborne measurements, *Tellus, Ser. B*, **52**, 636–651.
- West, R. A., L. R. Doose, A. M. Eibl, M. G. Tomasko, and M. I. Mishchenko (1997), Laboratory measurements of mineral dust scattering phase function and linear polarization, *J. Geophys. Res.*, **102**, 16,871–16,881.
- Wiscombe, W. J., and A. Mugnai (1986), Scattering from nonspherical Chebyshev particles, *NASA Ref. Publ.* 1157.
- Yang, P., and K. N. Liou (1996), Geometric-optics-integral-equation method for light scattering by nonspherical ice crystals, *Appl. Opt.*, **35**, 6568–6584.
- Yang, P., K. N. Liou, M. I. Mishchenko, and B. C. Gao (2000), Efficient finite-difference time-domain scheme for light scattering by dielectric particles: Application to aerosols, *Appl. Opt.*, **39**, 3727–3737.
- Zhao, T. X.-P., I. Laszlo, O. Dubovik, B. N. Holben, J. Sapper, D. Tanré, and C. Pietras (2003), A study of the effect of non-spherical dust particles on the AVHRR aerosol optical thickness retrievals, *Geophys. Res. Lett.*, **30**(6), 1317, doi:10.1029/2002GL016379.
- O. Dubovik and J.-F. Leon, Laboratoire d'Optique Atmosphérique, Université de Lille 1/CNRS, F-59655 Villeneuve d'Ascq, France. (dubovik@loa.univ-lille1.fr)
- T. F. Eck, B. N. Holben, T. Lapyonok, A. Sinyuk, I. Slutsker, and M. Sorokin, Laboratory for Terrestrial Physics, NASA Goddard Space Flight Center, Greenbelt, MD 20771, USA.
- M. Mishchenko, NASA Goddard Institute for Space Studies, New York, NY 10025, USA.
- O. Muñoz, Instituto de Astrofísica de Andalucía, E-18080 Granada, Spain.
- W. J. van der Zande, Molecular and Biophysics, Institute for Molecules and Materials, Radboud University, P.O. Box 9010, NL-6500 GL Nijmegen, Netherlands.
- B. Veihelmann, Royal Netherlands Meteorological Institute, NL-3730 AE De Bilt, Netherlands.
- H. Volten, Astronomical Institute "Anton Pannekoek," University of Amsterdam, Kruislaan 403, NL-1098 SJ Netherlands.
- P. Yang, Department of Atmospheric Sciences, Texas A&M University, College Station, TX 77843, USA.